Experimental Investigation of the Effect of Engine Representative Combustor Exit Temperature Profile and Disc Cavity Leakage Flow on the Film Cooling of Contoured Hub Endwall of a High Pressure Gas Turbine Rotor Cascade

A THESIS

SUBMITTED TO THE FACULTY OF THE GRADUATE SCHOOL OF THE

UNIVERSITY OF MINNESOTA

By

Arya Ayaskanta

IN PARTIAL FULFILLMENT OF THE REQUIREMENTS FOR THE DEGREE OF

MASTER OF SCIENCE IN MECHANICAL ENGINEERING

Terrence W. Simon, Adviser

May, 2013

ACKNOWLEDGEMENTS

First, I would like to thank my adviser, Prof. Terrence W. Simon, for allowing me to work with him. Prof. Simon's sound advice and thoughtful analysis of each aspect of the problem helped me a lot during the course of the project. Working with Prof. Simon has been a great learning experience for me. I would also like to thank him for his friendship.

I would like to thank Solar Turbines Inc. for the sponsorship of the project. In particular, I thank Hee Koo Moon and Luzeng Zhang of Solar Turbines Inc. for their guidance and valuable inputs throughout the project.

I thank Pat Nelson from the Machine Shop for helping me with the fabrication of different components of the test section. I would also like to thank Mark Erickson of Mechanical Engineering Tool Crib for providing me with the required tools readily.

I would like to thank my fellow graduate students Bo Yan, Chao Zhang, Smita Agrawal, Longzhong Huang, Qiao Li, Taiho Yeom, Yuhyen Seah, Debashish Burman and Jacob Wieberdink for their friendship and valuable suggestions throughout the project.

Last but not the least; I thank my parents for their much needed support and encouragement.

ABSTRACT

The effects of an engine representative combustor exit temperature profile on the adiabatic effectiveness values on a contoured turbine hub endwall at different disc cavity leakage flow rates are documented. Measurements for passage thermal fields and endwall adiabatic effectiveness values are made for disc cavity leakage mass flow rates of 0.5%, 1.0 % and 1.5 % of the mainstream passage flow; in presence of an engine representative combustor exit temperature profile. The endwall contour resembles the shape of a 'shark nose'. Endwall adiabatic effectiveness values for the 'shark nose' profile have been compared with those with a different endwall profile called 'dolphin nose'. Also, augmentation in adiabatic effectiveness by using an engine representative combustor exit temperature profile relative to other profiles has been documented. Passage thermal field and adiabatic effectiveness measurements with leakage flow at a temperature similar to that of the mainstream passage flow in presence of an engine representative combustor exit temperature profile have been made to 'track' the leakage flow within the cascade and obtain its contribution in cooling the hub endwall. The results indicate that increasing leakage flow rates leads to a more uniform distribution of adiabatic effectiveness values in the pitchwise direction at the passage entrance. Also, the presence of additional coolant in the near wall approach flow, leads to significant endwall cooling near the passage exit.

TABLE OF CONTENTS

List of Tables

List of Figures

NOMENCLATURE

Symbols

A	Hot Wire Calibration Constant (Dimensionless)
B	Hot Wire Calibration Constant (Dimensionless)
C	Blade True Chord Length (Centimeters)
C_{ax}	Blade Axial Chord Length (Centimeters)
C_p	Coefficient of Pressure (Dimensionless)
$E(\omega)$	Energy density spectrum ($m^2/sec^2.Hz$)
l	Length Scale (m)
Lu	Turbulence Energy Length Scale (m)
n	Hot Wire Calibration Constant (Dimensionless)
$U(t)$	Instantaneous Velocity (m/sec.)
$\bar{U}$	Time Averaged Velocity (m/sec.)
MFR	Leakage to Mainstream Mass Flow Ratio (Dimensionless)
N	Sample Size
P_s	Static Pressure (Pa)
P_t	Total Pressure (Pa)
Q	Volumetric Flow Rate ($m^3/sec.$)

Re_C	Reynold's Number Based on True Chord Length (Dimensionless)
S	Blade Span (cm)
t	Time (sec.)
T	Absolute Temperature (K)
Tu	Turbulence Intensity (%)
X	Passage Axial Coordinate (cm)
Y	Passage Pitchwise Coordinate (cm)
Z	Passage Spanwise Coordinate (cm)

Greek Symbols

ρ	Density (Kg/m^3)
Λ	Turbulence Integral Length Scale (m)
η	Adiabatic Effectiveness (Dimensionless)
ε	Eddy Diffusivity (m^2/s^3)
λ	Taylor Microscale (m)
ν	Kinematic Viscosity (m^2/s)
θ	Recovery Temperature (Dimensionless)
ω	Frequency (Hz)

Subscripts

0	Located at the Passage Inlet
l	Located at Leakage Rim Seal Slot Exit
w	Located on the Wall

Chapter 1

Motivation and Objectives

1.1 Motivation

Gas turbines have been in use as a source of power generation since the early 1900s.The need to improve thermal efficiency of gas turbines requires an increase in the average turbine inlet temperatures. However, due to environmental concerns, there is a move to cut down on the NOx emissions from gas turbines. In order to keep the NOx emissions low, the peak flame temperatures need to be reduced. Care has to be taken that the average temperatures at the turbine inlet aren't reduced significantly; otherwise there will be a penalty on the efficiency of gas turbines. This has led to the development of combustors which have reduced the peak temperatures, keeping the average temperature the same; thus leading to a 'flatter' temperature profile. These flatter combustor exit temperature profiles have led to an increase in the heat load on the hub endwall, far exceeding its thermal capabilities. Therefore it is necessary to devise efficient cooling schemes to keep the hub endwall temperatures well within the material capabilities. Thermal barrier coatings have proven quite useful in protecting the endwalls from the hot mainstream flow. Also, film cooling holes through which coolant bled from the compressor is ejected have been investigated by researchers to be a promising technique for endwall protection. Another technique that is being studied extensively is cooling of the hub endwall by the purge (or leakage) flow through the stator-rotor disc cavity. The cavity separates the stationary stator from the rotating rotor and must be supplied with coolant flow bled from the compressor so as to seal the cavity and prevent the ingression of the hot mainstream gases into the disc cavity. This leakage flow has been found to be useful in providing endwall protection, particularly near the entry of the rotor passages. It is essential to design techniques by which most of the leakage flow after exiting from the disc cavity remains on the endwall and isn't carried away from the endwall by the

secondary flows. One of the schemes to ensure this is endwall contouring. A contoured endwall accelerates the near-endwall flows, in this case the leakage flow, giving it more energy to counter the effects of the secondary flow structures. Apart from the leakage flow, some amount of coolant is also supplied to the approach flow through the combustor liner. This leads to a particular approach flow temperature profile developing before the flow enters the rotor passages. This additional coolant in the approach flow is quite important for endwall protection, particularly near the exit of the passage. Hence, it is essential to study the combined effect of coolant in the approach flow and in the leakage flow on the endwall film cooling effectiveness. Also, the effect of endwall contouring on the cooling effectiveness of coolant in the approach flow and in the leakage flow must be studied. Such an investigation will serve as a guide for turbine designers to choose the most efficient cooling scheme for endwall protection.

1.2 Objectives

In the present study, experiments are carried out to measure the endwall film cooling effectiveness at various leakage flow rates in the presence of an engine representative combustor exit temperature profile. The hub endwall used in the study is contoured axisymmetrically, resembling a 'shark nose'. Passage temperature field measurements are made to 'track' the near wall coolant and understand how it mixes with the mainstream flow. The results of the present study are compared to the results obtained under two other combustor exit temperature profiles investigated by Erickson[24].Also the results of endwall film cooling effectiveness are compared to another set of data obtained under a similar combustor exit temperature profile, with a different endwall contouring scheme that resembled a 'dolphin nose'. This gives an idea about the effect of endwall contouring on the endwall film cooling effectiveness. An attempt has been made to relate the observed effects with the secondary flow structures within a rotor passage. The results of the present study are intended to provide guidance to turbine designers to implement these cooling strategies in a real gas turbine.

Chapter 2

Turbine Endwall Aerodynamics and Heat Transfer: A Review

This chapter presents a review of some of the relevant past studies on secondary flows in gas turbine blade passages and endwall heat transfer. The complexity of making detailed flow and thermal measurements in an actual rotating turbine facility calls for the use of stationary cascades which mimic several aspects of a real turbine. These studies on stationary cascades have proved to be quite useful in understanding several key aspects of flow within turbine passages. Most of our present understanding of the secondary flow patterns and heat transfer in a gas turbine has its roots in the investigations made on stationary cascades. While stationary cascades are important in understanding the separate effects of various key parameters on gas turbine fluid mechanics and heat transfer, the importance of rotating rigs in simulating the situation in a real turbine cannot be neglected. In recent times progress has been made in developing experimental techniques to carry out investigations on rotating facilities to further refine our understanding of gas turbine fluid mechanics and heat transfer. Several excellent review articles are available in the literature that document in detail the work done in the field of turbine endwall aerodynamics and heat transfer. Sieverding [1], presented a review on the work done on secondary flows in a gas turbine cascade. This review gives an excellent account of the relevant studies on secondary flows in turbine cascades up to 1985. Langston's review [2] builds upon the work done past 1985. Simon and Piggush [3] present a review of turbine endwall aerodynamics and heat transfer. In addition to documenting the relevant studies on secondary flows in gas turbine cascades, the authors also provide a discussion on the work done in the field of endwall contouring to reduce secondary flow losses, endwall heat transfer and cooling schemes. For a more comprehensive description of the relevant topics on endwall aerodynamics and heat transfer, the reader is referred to these articles. This chapter presents a brief discussion

on work done both on stationary cascades and rotating rigs. Section 2.1 discusses the work done on the secondary flow structures within the blade passages which are believed to impact endwall heat transfer. Section 2.2 focuses on the work done on endwall heat transfer.

2.1 Secondary Flows in Cascades

Besides, the primary flow influenced by the turbine blades, the viscous effects of the endwalls produce three dimensional flow structures, also known as secondary flows. These secondary flows lead to significant aerodynamic losses within the rotor passages and also increase heat transfer to the endwalls. Langston [4] performed velocity measurements and flow visualization in a low speed cascade to describe the secondary flows within the cascade. In a later paper [5], Langston described the secondary flows from the standpoint of the endwall boundary layer. Figure 2.1.1 shows Langston's schematic description of schematic flow structures within a cascade, presented in [5].The following distinctive secondary flow structures were identified by Langston:

- Upstream of the passage inlet the endwall boundary layer separates into two legs of a horseshoe vortex. The point of separation is called the saddle point.

- The pressure side leg of the horseshoe vortex merges with and becomes part of the passage vortex. During its motion through the passage, the passage vortex is strengthened by cross flows due to pressure-to-suction pressure gradient. Since, the pressure side leg of the horseshoe vortex and the passage vortex become one within the passage, they have been treated as a single feature by Langston.

- The suction side leg wraps around the suction surface and rotates in a sense that is opposite to that of the passage vortex. It is thus labeled as the counter rotating vortex.

- The suction side leg of the horseshoe vortex (or the counter vortex) is much smaller than the passage vortex. It rotates in the opposite direction of the passage vortex.

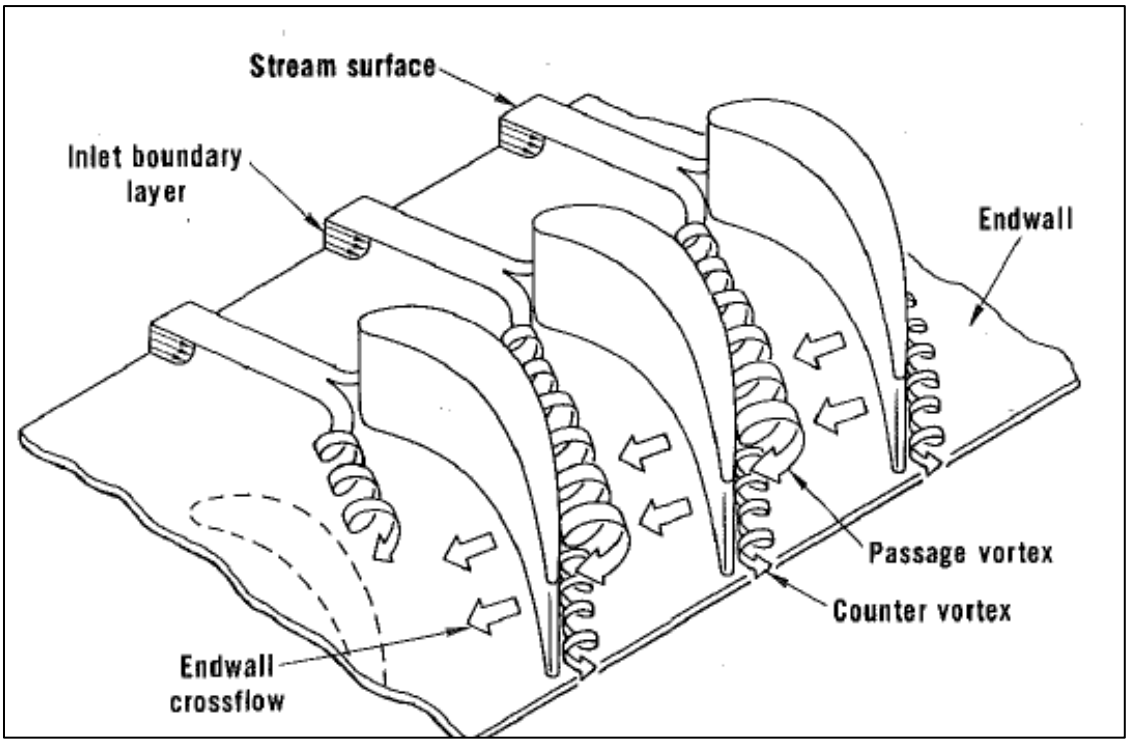

Figure 2.1.1 Secondary Flows in a Cascade (taken from Langston [5])

Sieverding et al. [6] used colored smoke to visualize stream surfaces moving through a cascade. The authors present a description of the evolution of the passage vortex as shown in figure 2.1.2. The stream surface labeled SS2 lies outside the endwall boundary layer. As one moves into the passage, the blade curvature causes the stream surface SS2 to roll up, with the fluid near the pressure side moving towards the suction side. This roll up motion leads to the development of the passage vortex. Moving downstream the passage vortex entrains more fluid outside the endwall boundary layer and increases in strength. Also, it can be seen from figure 2.1.2 that the pressure side led of the horseshoe vortex, continues into the passage along a smooth path and is gradually enveloped by the

passage vortex. Sieverding treats the pressure side leg of the horseshoe vortex and the passage vortex as different entities because of their different origin.

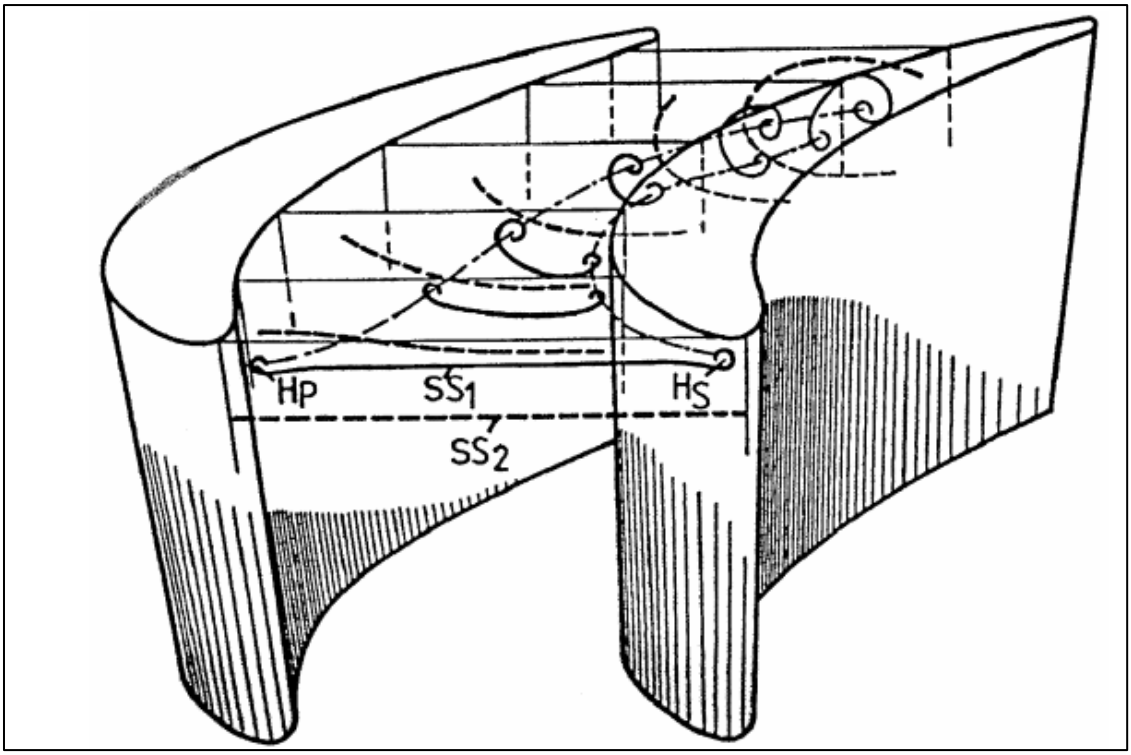

Figure 2.1.2 Development of Passage Vortex within a Turbine Blade Row Cascade (Figure taken from Sieverding [6])

.

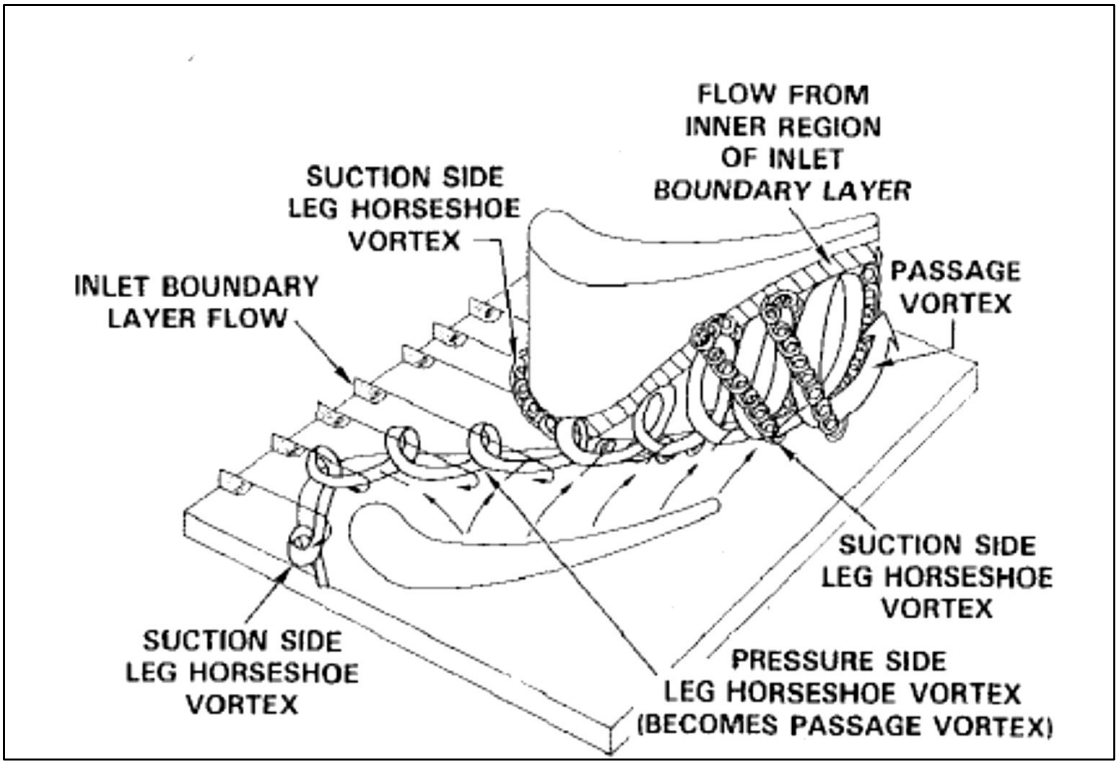

Figure 2.1.3 Secondary Flow Structures in a Turbine Cascade, Sharma and Butler [7]

Sharma and Butler [7] proposed a slightly different explanation of the different secondary flow structures within turbine passage. According to the authors, the fluid particles closest to the endwall do not become part of the horseshoe vortex. These low momentum fluid particles are convected toward the suction surface, and gradually climb the airfoil surface and exit at the top of the airfoil at the end of the passage. The passage vortex meets the suction surface at the minimum pressure point within the cascade. The suction side leg of the horseshoe cortex has a sense of rotation opposite to that of the passage vortex and remains close to the endwall until the passage vortex meets the suction surface. At this point the suction side leg of the horseshoe vortex is forced off the endwall and orbits around the passage vortex without losing its identity.

Wang et al. [8] carried out flow visualization to study different secondary flow patterns in a high performance turbine blade cascade. The authors used smoke wire and laser light sheet for flow visualization. The flow had a lower Reynolds number to facilitate flow visualization. The authors identified additional vortex structures within the cascade. Figure 2.1.4 shows the different secondary flow structures described by Wang et al. A corner vortex was found to exist at the leading edge. Also, wall vortices were induced at the location where the passage vortex met the suction surface. The suction side leg of the horse shoe vortex wraps around the passage vortex and becomes part of the overall vortex system. The complexity of the secondary flow structures merits further investigation into their origin under different conditions.

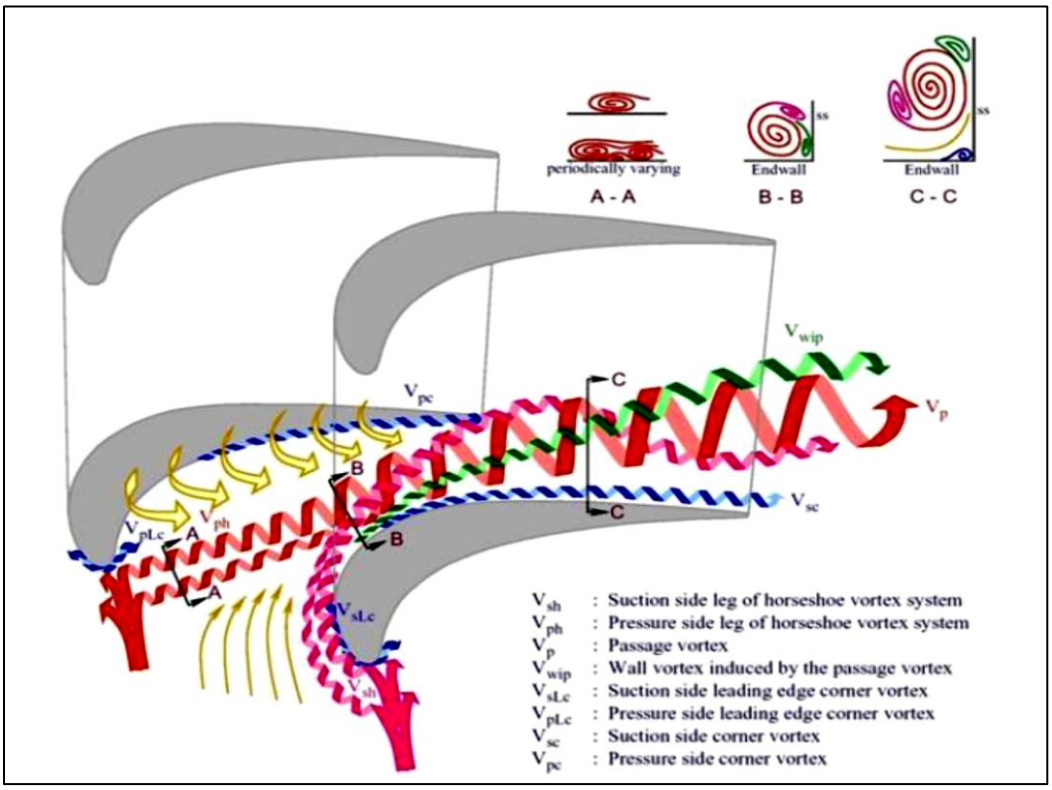

Figure 2.1.4 Secondary Flow Structures in a Turbine Cascade (Taken from Wang et al. [8])

2.2 Endwall Heat Transfer

Heat transfer rates on the endwall are strongly related to the secondary flow structures discussed in section 2.1. Graziani et al. [9] carried out heat transfer measurements on the endwall of a large scale turbine blade cascade for two inlet boundary layer thicknesses. Figure 2.2.1 shows the Stanton number contours on the endwall obtained by the authors. It can be seen that there is a region of high heat transfer near the blade leading edge. This is probably because of the influence of the horseshoe vortex roll up motion in this region. Also, the region of high heat transfer is smaller for the thin inlet boundary layer case in comparison to the thick inlet boundary layer case. The two inlet boundary layer cases also exhibit stark differences in the Stanton number contours near the throat region, which the authors attribute to a complex interaction between the passage vortex, streamwise acceleration and shear generated endwall cross flows.

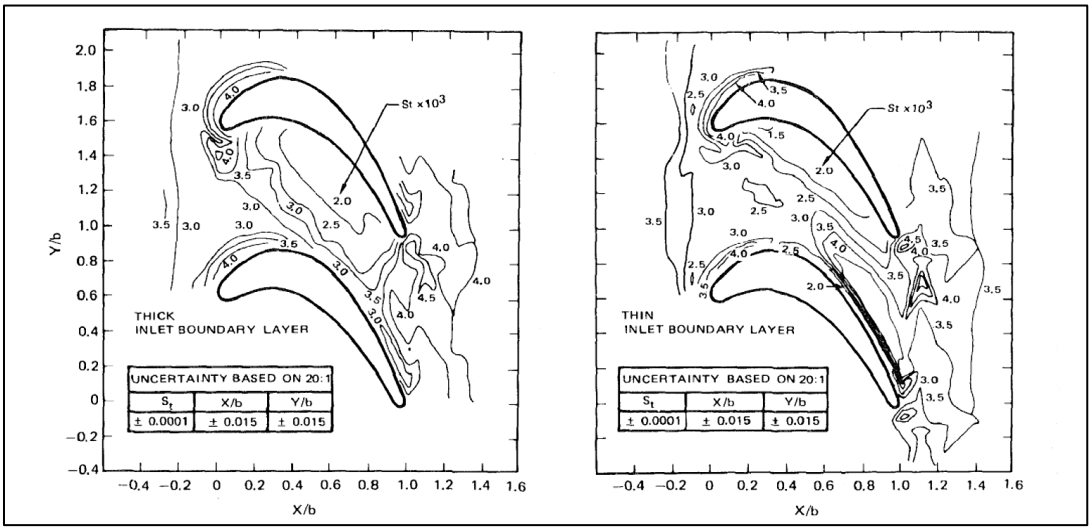

Figure 2.2.1 Endwall Stanton Number Contours for cases with (a) Thick Inlet Boundary Layer (left) and (b) Thin Inlet Boundary Layer (right), Graziani et al. [9]

Goldstein and Spores [10] used the naphthalene sublimation technique to identify regions of high mass transfer on a hub endwall coated with naphthalene. The regions of high mass transfer would indicate regions of intense heat loading by heat/mass transfer

analogy. Figure 2.2.2 shows the mass transfer contours obtained on the endwalls in the study. A localized region of high mass transfer near the leading edge indicates the presence of strong leading edge corner vortices. Also, a region of high mass transfer on the suction side can be seen at the location where the passage vortex meets the suction surface.

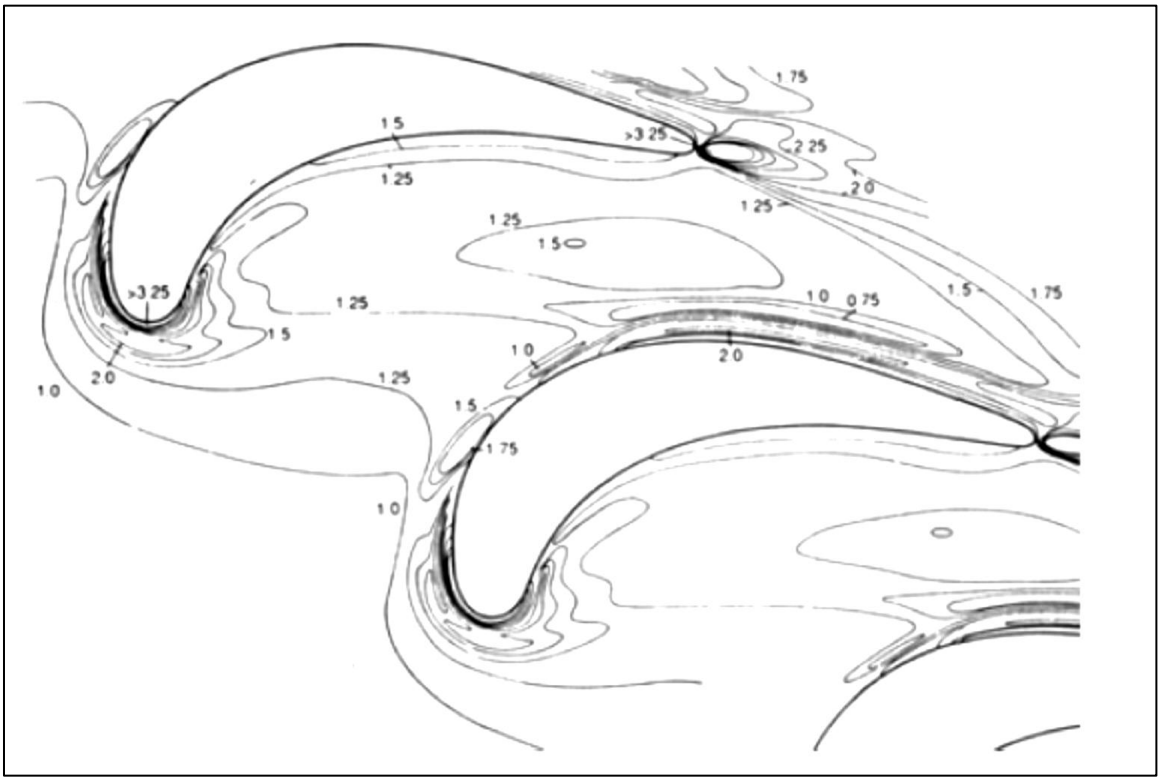

Figure 2.2.2 Mass Transfer Contours on a Turbine Hub Endwall, Goldstein and Spores [10]

One of the earliest studies on the film cooling effectiveness of injected coolant on the endwalls of a turbine vane passage was done by Blair [11]. Coolant was injected into the passage through a slot located upstream of the vanes. Film cooling effectiveness on the endwall was measured at different coolant flow rates. Higher film cooling effectiveness values were observed near the suction surface indicating washing away of the coolant toward the pressure surface by the cross stream pressure gradient. There was some increase in the extent of endwall cooling by increasing the coolant injection rates.

Piggush and Simon [12] performed heat transfer measurements on the contoured endwall of a turbine vane cascade with a transition slot upstream of the vane leading edge and slashface gap within the passage. Effects of a forward and a backward facing step at the transition slot were studied in presence of leakage flow injected through the slot and the slashface gap. It was found that the forward facing step at the transition slot led to thinning of the boundary layers and an increase in heat transfer rates over the whole endwall section. A backward facing step led to a thickening of the boundary layers and a decrease in heat transfer rates over the whole endwall section. The authors also documented the effects of steps at the slashface gap on the heat transfer rates to the endwall. Thrift and Thole [13] experimentally studied the effect of the angle at which coolant is injected from a slot upstream of the vane passages on the time averaged flow fields at the stagnation plane. Corresponding effects on the endwall heat transfer were also studied. Figure 2.2.3 shows the cascade schematic with different slot orientations used by Thrift and Thole[13].

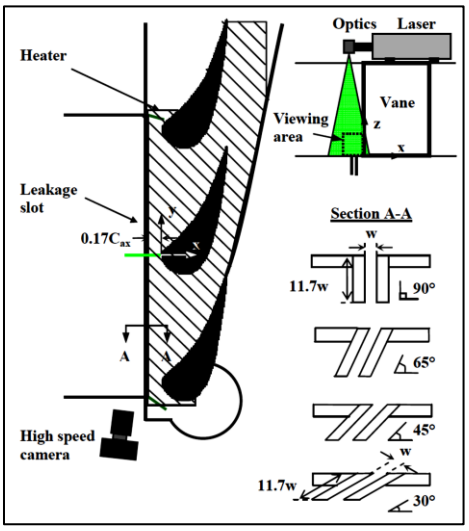

Figure 2.2.3 Cascade Test Section Schematic and Injection Slot Geometries, Thrift and Thole[13]

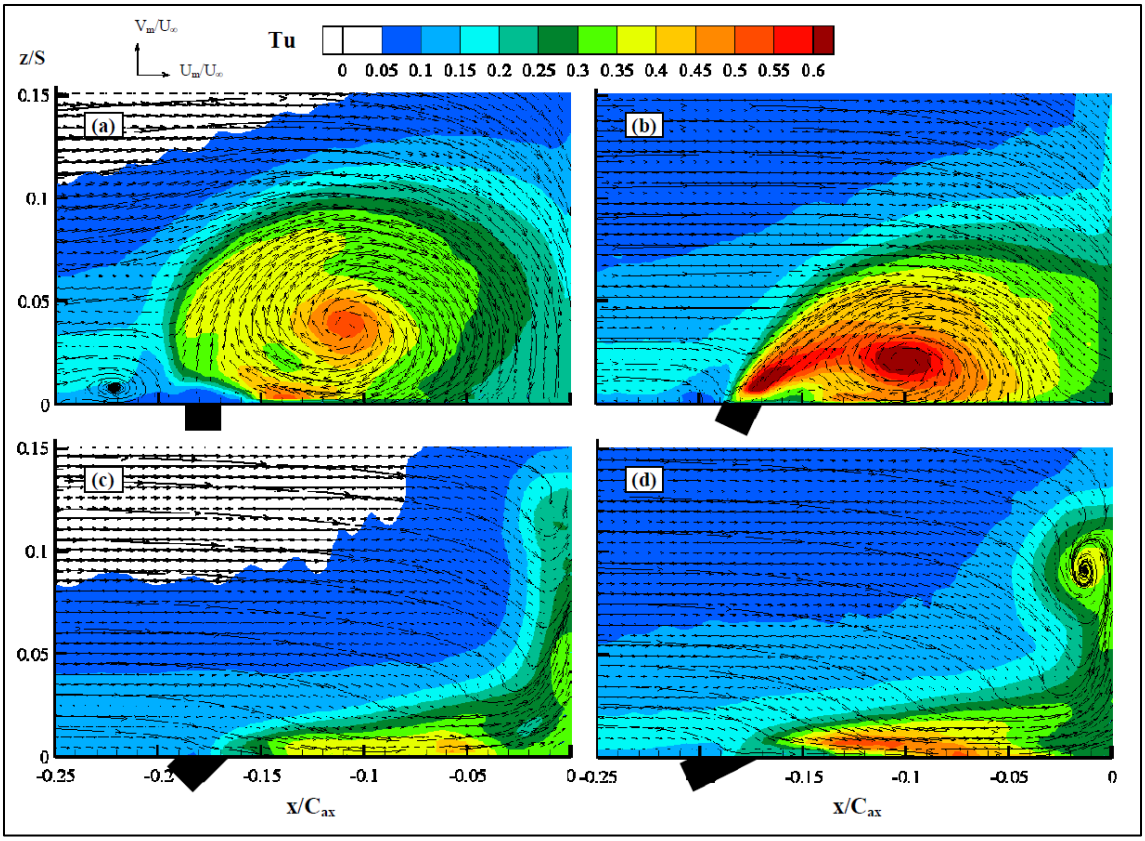

Figure 2.2.4 Time Averaged Flow Streamlines at Stagnation Plane for (a) 90 degree injection (b) 65 degree injection (c) 45 degree injection and (d) 30 degree injection from the Upstream Slot, Thrift and Thole [13]

Figure 2.2.4 shows the time averaged flow field at the stagnation plane. It can be seen that the 90 degree and 65 degree slot injection creates and sustains a time averaged vortex structure in front of the vane leading edge. On the other hand, the 45 degree and 30 degree injection cases prevent inlet boundary layer separation as it meets the vane leading edge. In fact in the 30 degree injection case, the inlet boundary layer is so energized that there is an upwash on the leading edge

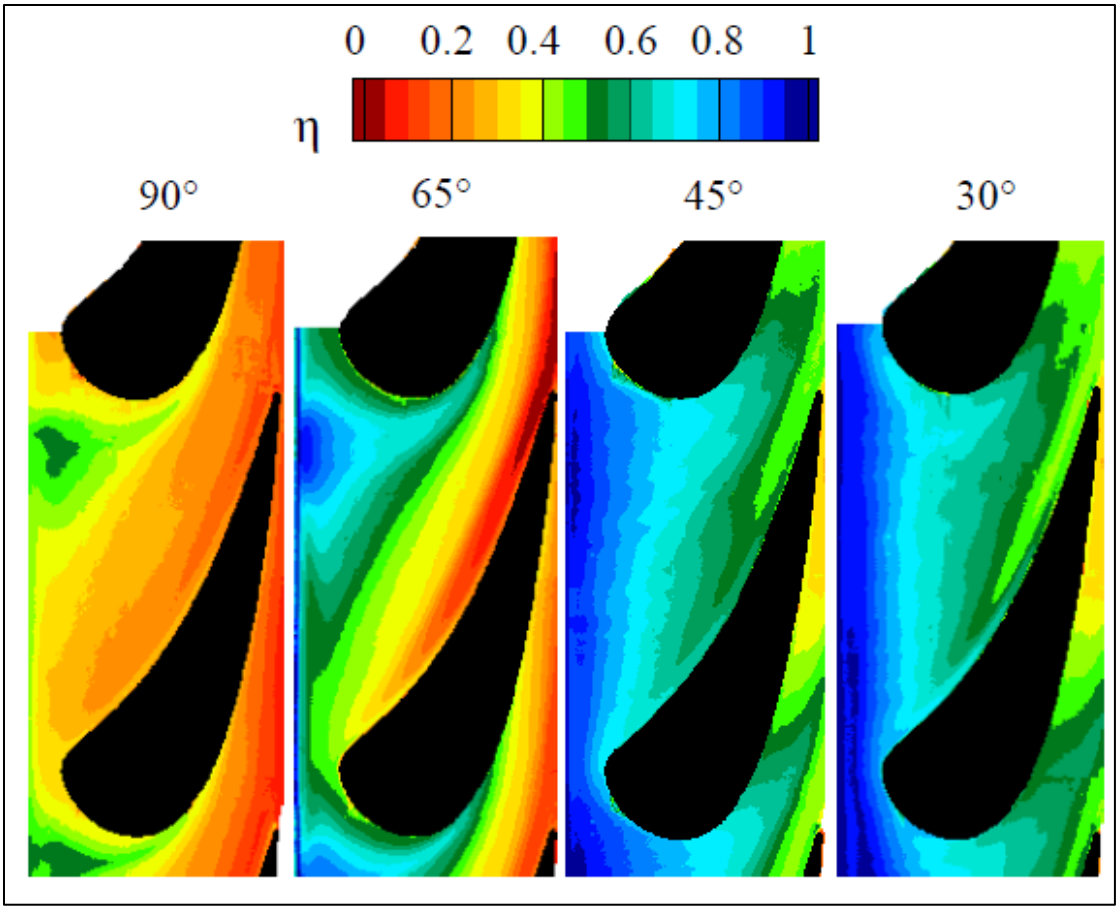

Figure 2.2.5 Endwall Adiabatic Effectiveness Distribution for different Upstream Slot Geometries, Thrift and Thole [13]

Figure 2.2.5 shows the corresponding adiabatic effectiveness plots for the four cases. The 90 and 65 degree cases show lower effectiveness values, whereas the 45 and the 30 degree cases show higher values of adiabatic effectiveness.

Popovic and Hodson [14] experimentally and numerically studied the interaction between rim seal leakage flow and mainstream flow in a high pressure turbine blade cascade with a contoured endwall. The authors identified a vortex structure within the leakage slot called the 'leakage vortex'. This vortex is 'fed' by the ingestion of the mainstream flow into the leakage cavity. The mainstream flow ingresses into the leakage cavity forming the leakage vortex, which spills flow out of the leakage slot near the suction side. Figure 2.2.6 shows the slot geometry used by Popovic and Hodson and Figure 2.2.7 shows the

flow streamlines in the leakage cavity. The authors documented that at 0.5 % leakage mass flow ratio (MFR), there is only a small streak of leakage coolant in the suction side. Increase the leakage flow rate, led to more coverage of the endwall, however the pressure side was devoid of any coolant even at the highest flow rate of 1.5% MFR. Thus, higher leakage flow rates are more effective in pushing the ingested air out of the rim seal cavity. Also there is less mixing between leakage flow and the ingested flow in the rim seal cavity at higher leakage flow rates.

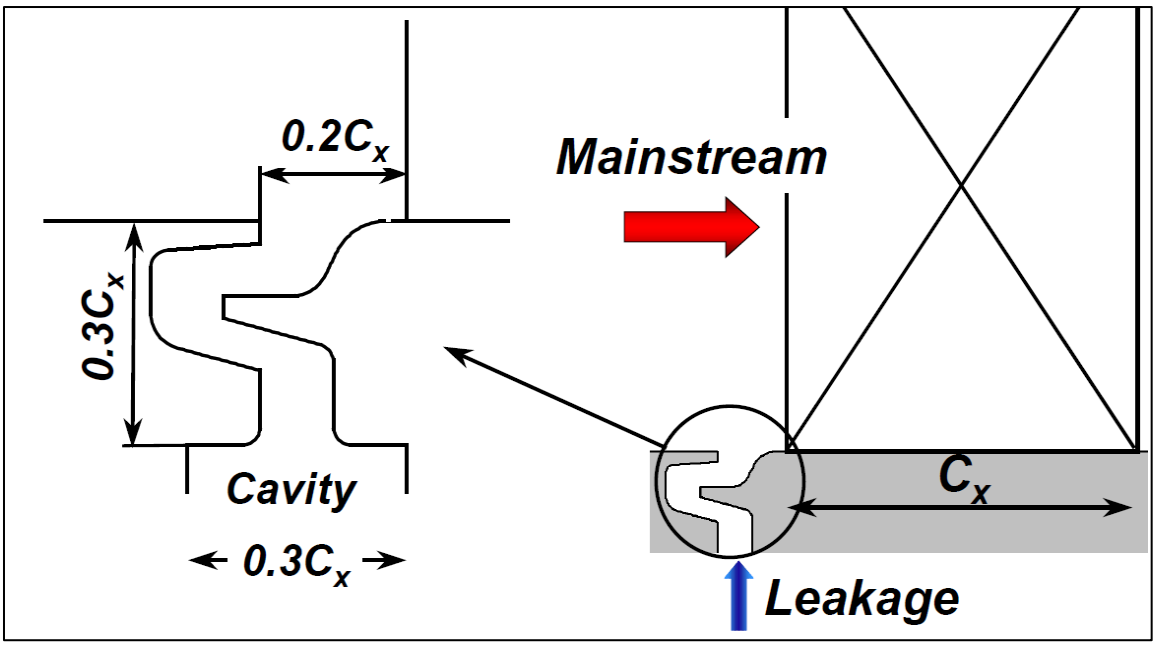

Figure 2.2.6 Disc Cavity Configuration used by Popovic and Hodson to study Leakage Flow-Mainstream Flow Interaction in a HP Turbine Blade Cascade [14]

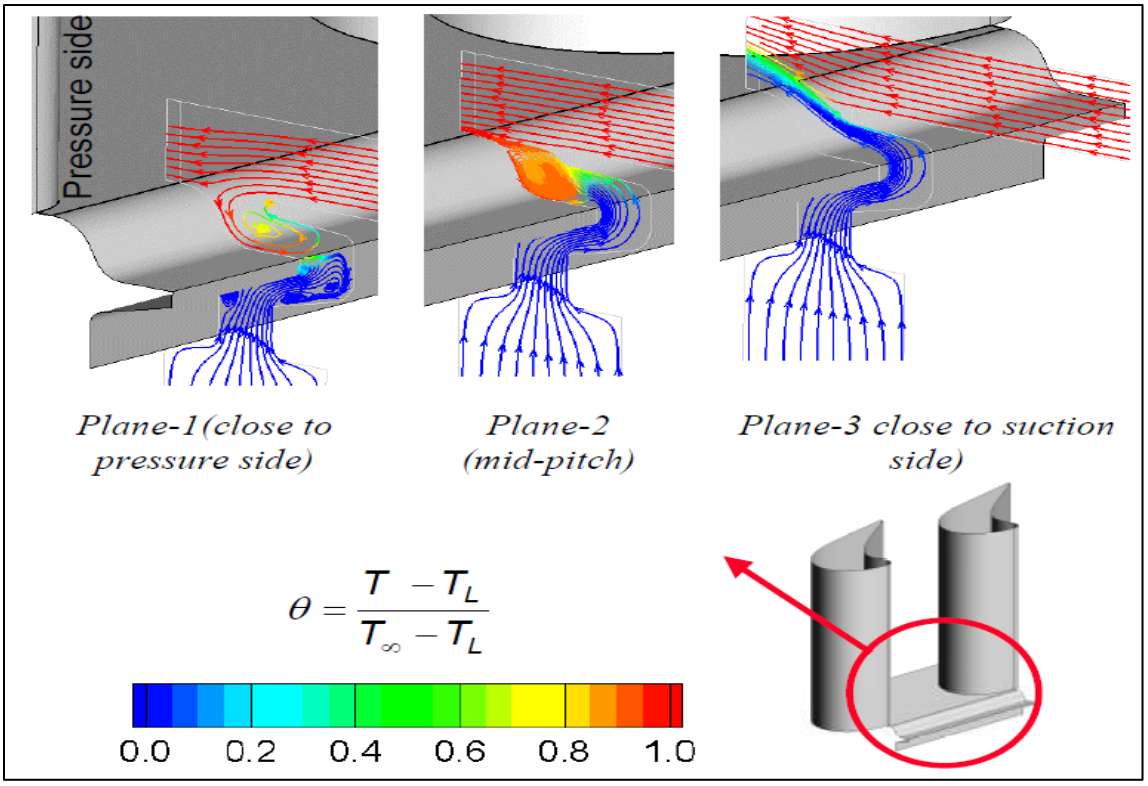

Figure 2.2.7 Leakage Slot Flow Streamlines and Thermal Field by Popovic and Hodson [14]

Suryanarayana et. al. [15] experimentally studied the effect of rotational speed of the rotor on the film cooling effectiveness of purge flow. It was found that decreasing rotational speed of the rotor leads to a more 'non-uniform' film cooling effectiveness in the pitchwise direction, with most of the coolant being accumulated along the suction side.

Lynch et. al. [16] conducted heat transfer measurements on a low pressure turbine cascade with a flat and a non-axisymmetrically contoured endwall. It was found by oil flow visualization that the passage vortex was reduced in strength in case of the contoured endwall. Heat transfer measurements indicated lower heat transfer near the pressure side of the contoured endwall as compared to the flat endwall. The decrease in heat transfer values was attributed to the reduction in the strength of passage vortex in case of the contoured endwall. Mirzamoghadam et. al. [17], investigated the problem of

hot gas ingestion into the rim seal disk cavity of a high pressure turbine. It was found that in presence of circumferential annulus pressure asymmetry, there is ingestion into the upper part of the rim cavity even at high purge (leakage) flow rates.

Pau et al. [18] studied the influence of purge mass flow rate on ingression of the mainstream flow into the disc cavity on a rotating rig by taking static pressure measurements within the disc cavity and the hub platform. Regions of ingression were identified along the vane pitch. These regions were reduced with increasing purge flow rate. Additional pitchwise non-uniformities were introduced by the shocks at the exit of the vanes. The authors investigated in detail the interaction between the purge flow or the leakage flow (the purge flow is referred to as the leakage flow throughout this study) and the mainstream flow. Figure 2.2.8 adapted from the same study reveals the way the leakage flow is being entrapped by the horseshoe vortex near the blade leading edge. It was also reported that the leakage flow helped in lowering the intensity of the passage vortex by strengthening the vortex structures which rotate in opposite sense to that of the passage vortex. Thus, the leakage flow produced a more uniform static pressure distribution in the pitchwise direction.

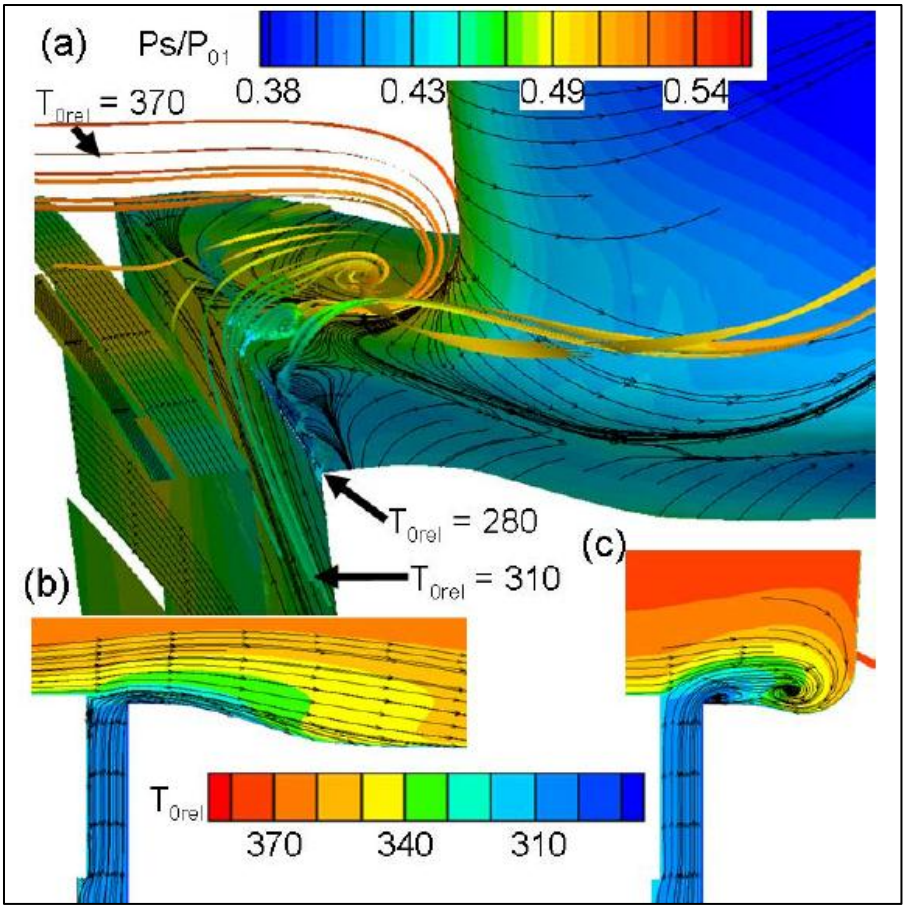

Figure 2.2.8 Interaction between Leakage and Mainstream Passage Flow, Pau et al. [18]

Schuepbach et al. [19] studied the effect of performance of two different asymmetrically contoured endwalls in comparison to an axisymmetric baseline case in presence of rim-seal purge flow. It was found that the asymmetric cases lose some of their benefit in total to total efficiencies with increasing purge flow. Hermanson and Thole [20] computationally studied the effect of inlet temperature and velocity profiles on secondary flows for a stator guide vane. Figure 2.2.9 shows the inlet temperature profiles studied by the researchers. Cases 1, 3 and 4 were run with the same velocity boundary layer thickness. Figure 2.2.10 shows the total pressure, velocity and stream wise vorticity contours for the said cases. It was found that the case with a thick thermal boundary layer significantly affects the nature of secondary flows at the inlet of the vane passages. The thick thermal boundary layer case (case 4) resulted in a separation of vortex structures

bringing flow towards the endwall from the structures taking flow away from the endwall with the earlier staying under 14% of the span and the later staying over 14% of the span. This separation was not seen in cases with no thermal boundary layer and a thin thermal boundary layer (cases 1 and 3).

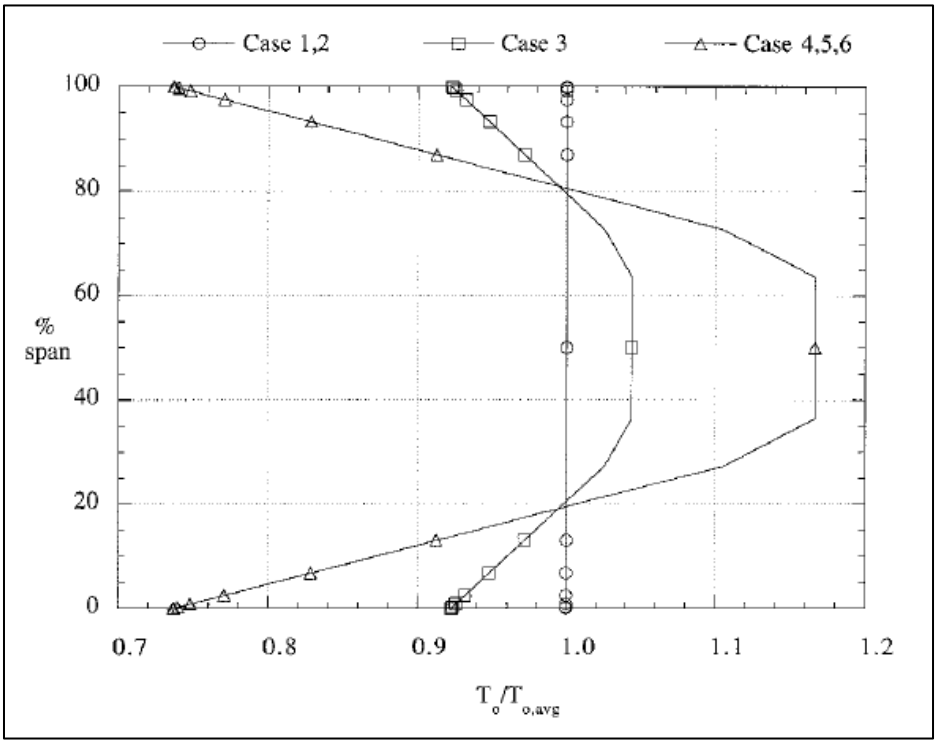

Figure 2.2.9 Combustor exit temperature profiles studied by Hermanson and Thole [20]. The cases 1, 3 and 4 were analyzed in presence of the same velocity boundary layer thickness.

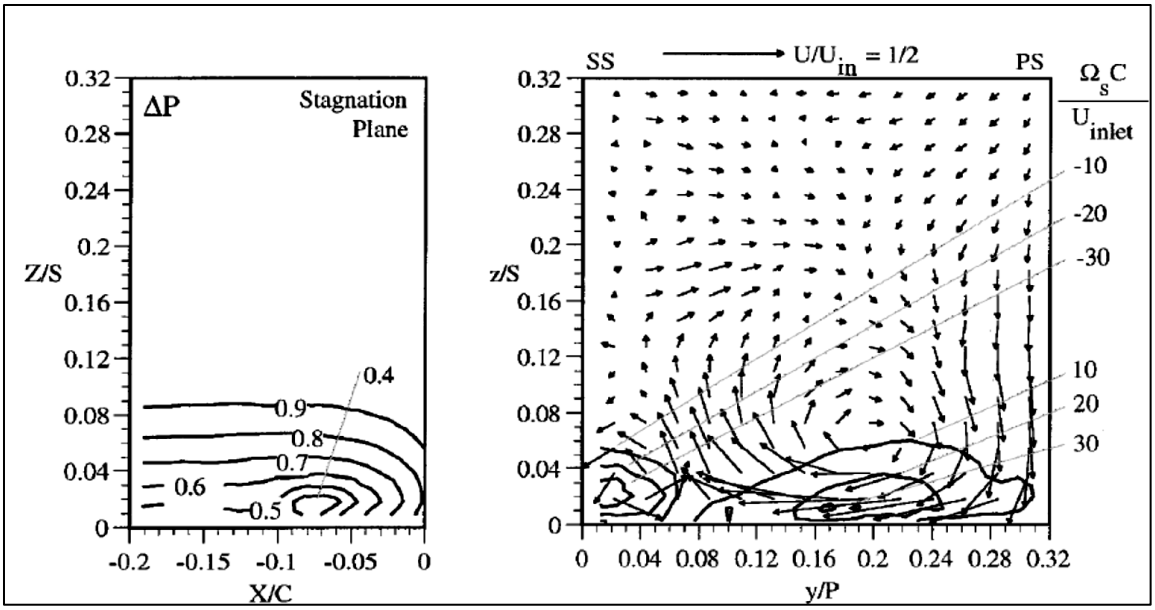
ΔP
Stagnation Plane
Z/S
X/C
0.4
0.9
0.8
0.7
0.6
0.5
SS
U/U_in = 1/2
PS
Ω_s C / U_inlet
-10
-20
-30
10
20
30
z/S
y/P

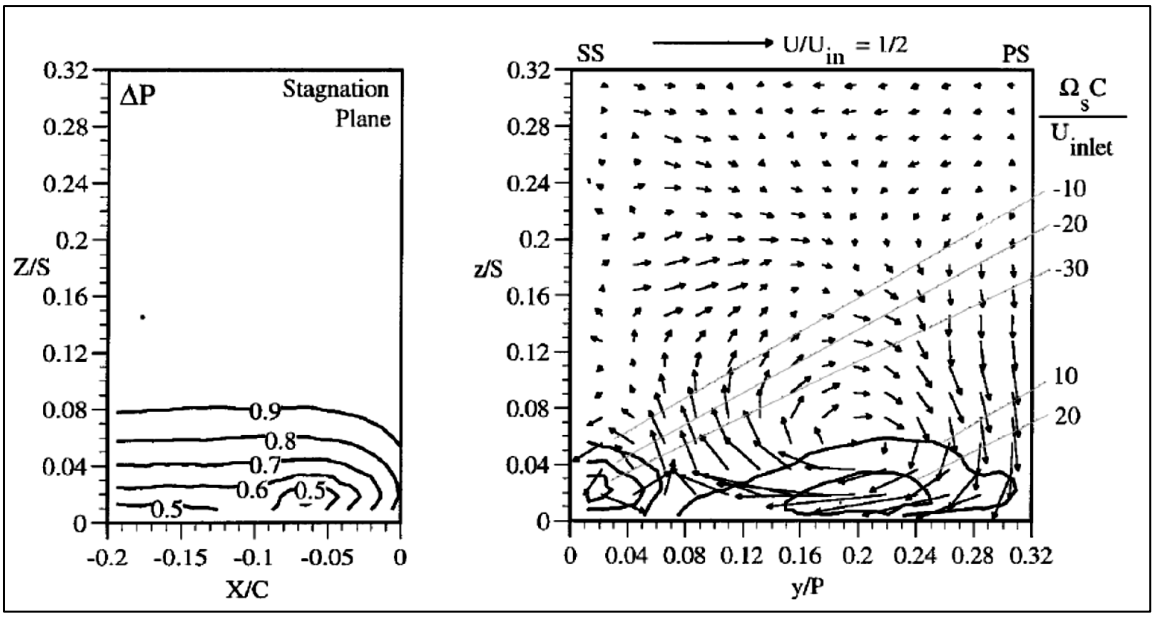
ΔP
Stagnation Plane
Z/S
X/C
0.9
0.8
0.7
0.6
0.5
SS
U/U_in = 1/2
PS
Ω_s C / U_inlet
-10
-20
-30
10
20
z/S
y/P

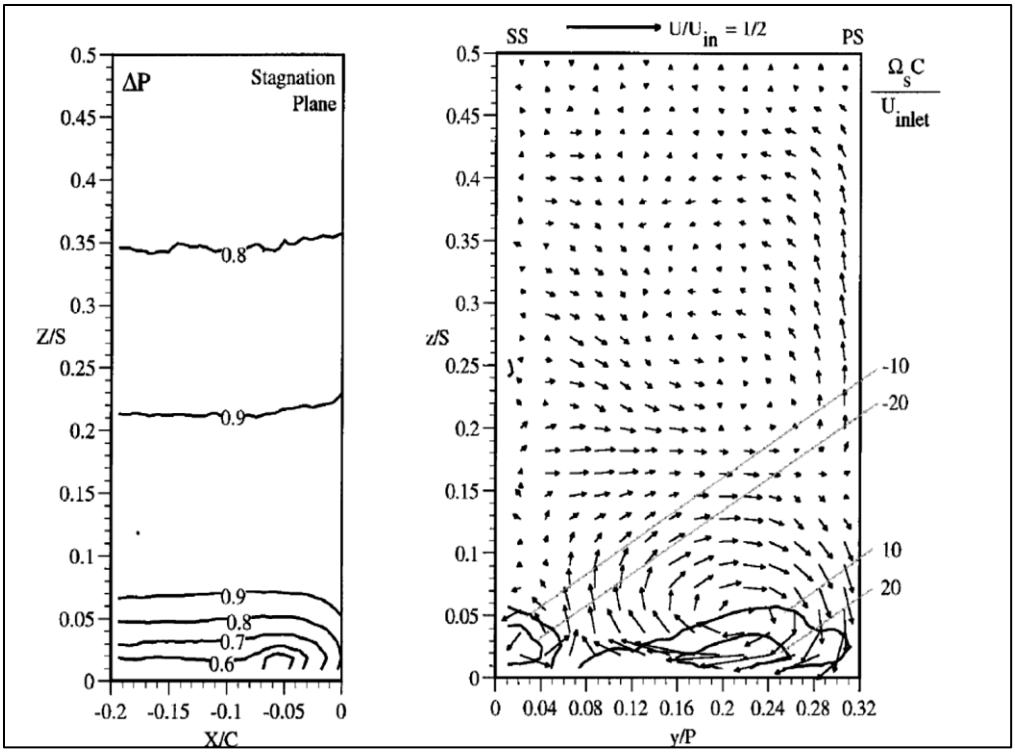

Figure 2.2.10 Total Pressure and Streamwise Vorticity Contours at the Inlet of Vane Passages, Hermanson and Thole [20]

Barringer et al. [21] studied the influence of a variety of total pressure and temperature profiles on the vane endwall heat transfer of a high pressure gas turbine. It was found that the inlet total pressure profiles consistent with a turbulent boundary layer have higher Nusselt number values near the vane inlet as well as the exit than the profiles with inflection points which have higher total pressure near the endwall relative to the midspan.

Matheison et al.[22] experimentally investigated the migration of a uniform and a radial combustor exit temperature profile through the high pressure rotor stage in a rotating facility. Experiments were conducted for situations without cooling and with purge and blade internal cooling. It was found that for both cooled and uncooled situations, the uniform combustor exit temperature profile is flattened by the time it reaches downstream

of the turbine, whereas the radial profile undergoes a significant change in its shape during its passage through the turbine stage. The influence of the cooling scheme is to reduce the average temperatures throughout the span. The temperature profiles were measured in three locations in the spanwise direction: upstream of the blade leading edge by a rake with thermocouples, at the blade leading edge by thermocouples mounted on the blade leading edge and downstream of the passage by another rake with thermocouples.

Taremi et al. [23] experimentally investigated the secondary flows in linear turbine cascades with flat and non-axisymmetrically contoured endwalls. Their surface flow visualization revealed that endwall contouring led to weaker interaction of the vortical structures within the passage with the suction surface boundary layers. Also, the mid-passage crossflows seemed to be oriented more in the streamwise direction in case of the contoured endwall, indicating a weaker pressure-to-suction pressure gradient.

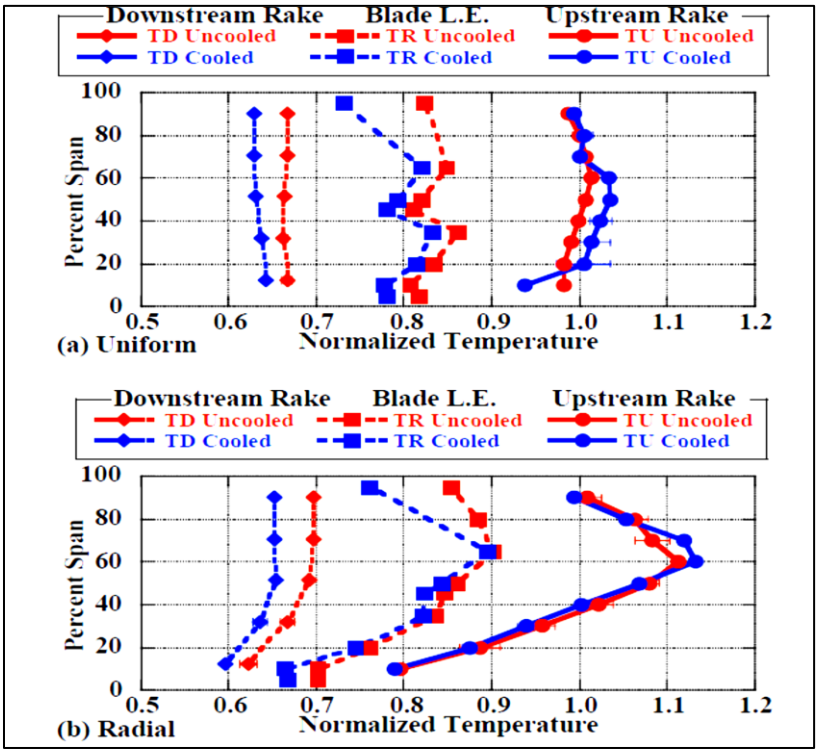

Figure 2.2.11 Migration of the uniform (top) and radial(bottom) combustor exit temperature profiles measured by Matheison et. al. [22].

Erickson[24] studied the effect of leakage flow rates on the passage aerodynamic losses and endwall adiabatic effectiveness using two differently contoured endwalls. One contouring scheme was called the 'Dolphin nose' (labeled endwall A in figure 2.2.12) and the second endwall scheme was known as 'Shark nose'(labeled endwall B in figure 2.2.12).The tests were conducted with a flat combustor exit temperature profile meaning there was no coolant in the approach flow. Figure 2.2.12 shows the adiabatic effectiveness distribution for the two endwalls at different leakage flow rates. The Dolphin nose performs better at the beginning of the passage, suggesting the weakening of the secondary flow structures due to the strong acceleration of the near wall fluid by the steep slope of the dolphin nose profile as against a more gradual slope of the shark nose profile.

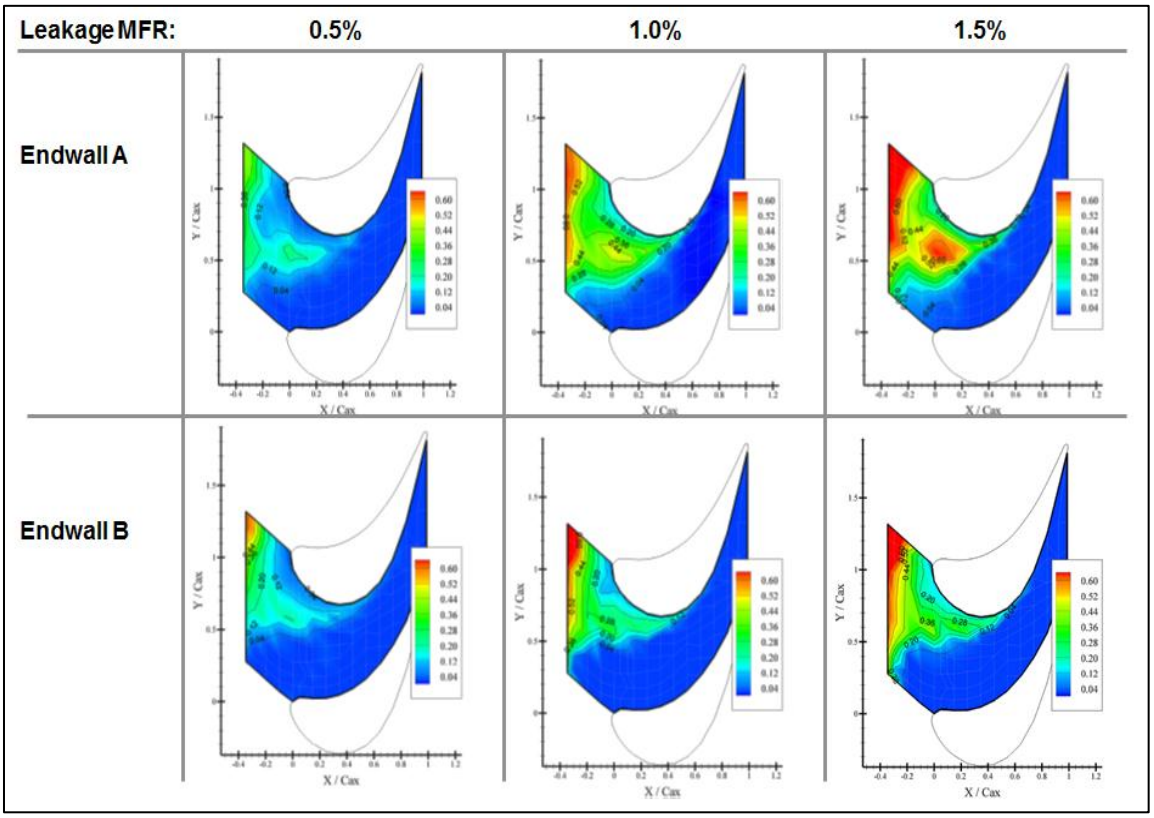

Figure 2.2.12 Endwall Adiabatic Effectiveness Distribution at different Leakage MFRs for two different Endwall Contours under a Flat Combustor Exit Temperature Profile, Erickson [24]

Erickson [24] also tested a case with a thin approach flow thermal boundary layer (contains coolant upto 10% of the span). It was found that this profile increased cooling near the pressure side at the beginning of the passage, but a large part of the endwall going deeper into the passage was devoid of any cooling.

The present study focusses on the use of an engine representative combustor exit temperature profile and its effects on the adiabatic effectiveness distributions on a contoured hub endwall resembling a ‘shark nose’. Tests have been conducted at of 0.5%, 1.0% and 1.5% leakage MFR. It is believed that such a study would provide guidance to turbine designers in understanding the mixing between the leakage flow and the mainstream passage flow and the effect of such mixing on the endwall adiabatic effectiveness distribution.

CHAPTER 3

Experimental Test Facility

This chapter discusses the essential features of the test facility used for the present study. A pre-existing facility designed and developed by Erickson [24] was used for the study. A brief description of the essential features of the facility is provided in this chapter. For a detailed description of the design and fabrication of different components of the test section, the reader is referred to Erickson [24].

3.1 Wind Tunnel

The test facility consists of a blow-down type wind tunnel located in the Heat Transfer Laboratory (ME-281), Mechanical Engineering, University of Minnesota. Figure 3.1.1 shows a schematic sketch of the wind tunnel layout.

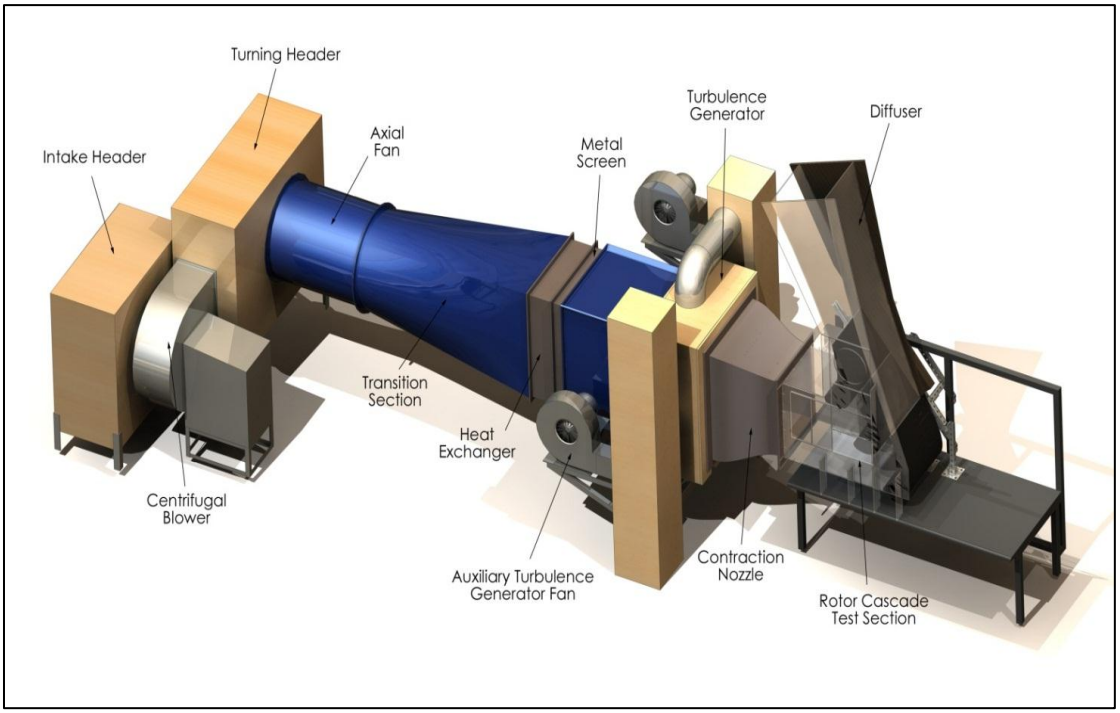

Figure 3.1.1 Test section layout, taken from Erickson [24]

The following sections describe the notable features of various components of the wind tunnel.

3.2 Mainstream Flow Fans

The mainstream flow is introduced into the wind tunnel by means of a centrifugal blower through an intake header. The intake header is lined by air filters. The centrifugal blower is a 3.7 kW fan made by the New York Fan Company .An additional axial flow fan is used to provide more energy to the flow introduced into the tunnel by the mainstream flow fan. The axial fan has a rating of 5.6 kW and is manufactured by Joy Manufacturing Company. It is fitted with an Alan Bradley motor controller, which can operate under variable frequency in the range of 0-60 Hz in 0.1 Hz increments. The desired mainstream flow velocity can be obtained by varying the frequency. For the present study, the highest frequency of 60 Hz was used.

3.3 Auxiliary Fans

Auxiliary fans are used in this to study to cater to certain specific needs of the wind tunnel. These are:

- Turbulence Generator Fans
- Leakage flow fan
- Approach flow- temperature control- slot flow fan

3.3.1 Turbulence Generator Fans

A turbulence generator (described later in the chapter) is used in the study to obtain high free stream turbulence, representative of a real gas turbine combustor. The turbulence generator is supplied to by two 3.7 kW centrifugal fans manufactured by Dayton Electric Manufacturing Company. These fans are positioned on two opposite sides of the wind tunnel and supply air into a flow distribution cabinet. From the flow distribution cabinet

the supply air enters the turbulence generator from the side and from the top via a 90 degree elbow, as shown in the figure 3.3.1.

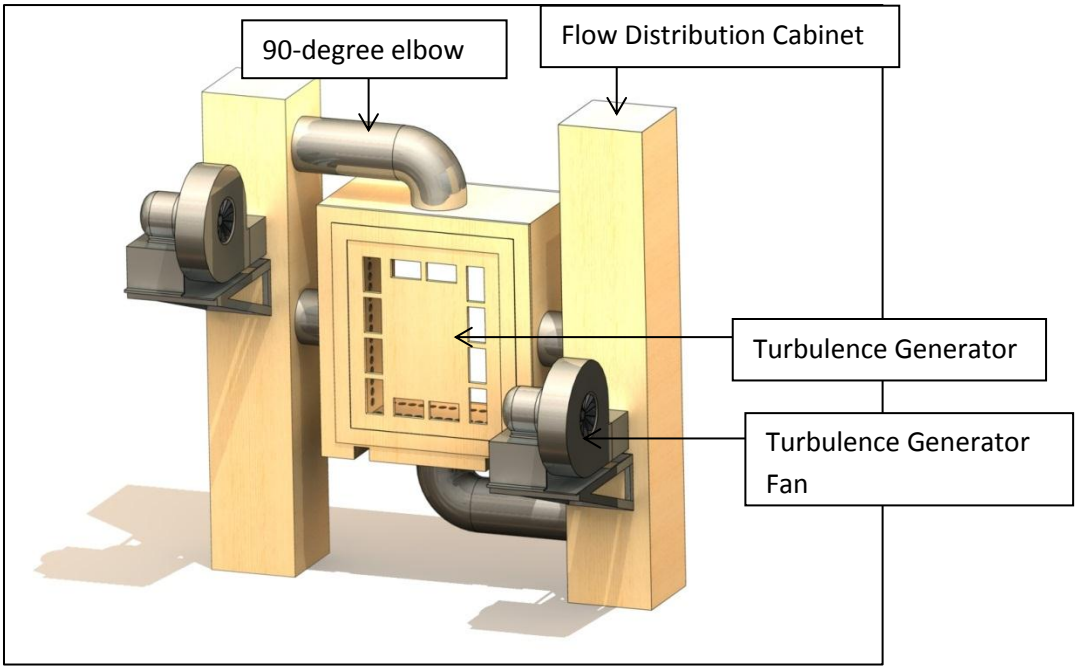

Figure 3.3.1 Turbulence Generator fans supplying to the flow distribution cabinet, taken from Erickson[24]

3.3.2 Leakage Flow Fan

The leakage flow plenum fed by a 1.5 kW fan made by the Cincinnati Fan Company. Its rotational speed is controlled by a Magnatek GPD333 motor controller, whose operating frequency can be varied in 0.1 Hz increments. The fan's outlet is connected to the leakage plenum by means of a PVC pipe. In the middle of the pipe, a Meriam^{TM} laminar flow element (LFE) is attached for the purpose of flow measurement (details described in chapter 4). The laminar flow element is connected to an inclined tube manometer, which reads pressure difference across the LFE in inches of water.

3.3.3 Temperature Control Slot Flow Fan

A temperature control slot is located upstream of the passages to achieve the engine representative combustor exit temperature profile by introducing flow at an appropriate temperature into the passage. This flow helps in keeping the wall of the wind tunnel upstream of the leakage slot at a temperature that equals the mean leakage flow temperature. It is fed by a fan similar to the one supplying the leakage plenum. This fan, like the one supplying the leakage plenum, is controlled by a Magnetek GPD333 motor controller whose frequency can be varied in order to vary the rotational speed of the fan. The outlet of the fan is connected to a 2.3 meters long 10 cm diameter PVC piping. Inside the piping are heating elements, whose power input can be controlled by means of a Variac. The desired combustor exit temperature profile is obtained by varying the power input to the heating elements. The piping is connected to a header which causes a uniform distribution of the flow. A fine screen is placed at the exit of the header to get rid of any vortices that might have been introduced by the motion of the fan.

3.4 Turbulence Generator

The main function of the turbulence generator is to create a uniform, high free stream turbulence field that resembles the flow exiting typical low NOx combustor. A brief description of the turbulence generator used in the study is presented here. For a more detailed description of the design, fabrication and the working principles of the turbulence generator, the reader is referred to Erickson [24].

The mainstream flow entering the wind tunnel encounters a large blockage by the turbulence generator. Square slots are machined on the back of the turbulence generator as shown in figure 3.4.1 to produce streamwise jets. These jets enter the mixing volume of the turbulence generator, which is shown in figure 3.4.2. Inside the mixing volume cross flows (supplied from the turbulence generator fans) are introduced in the form of jets produced by circular holes. The streamwise and cross flow jets mix in this zone, producing a uniform, high free stream turbulence field. The flow exits the front face of the turbulence generator through the slots machined on it.

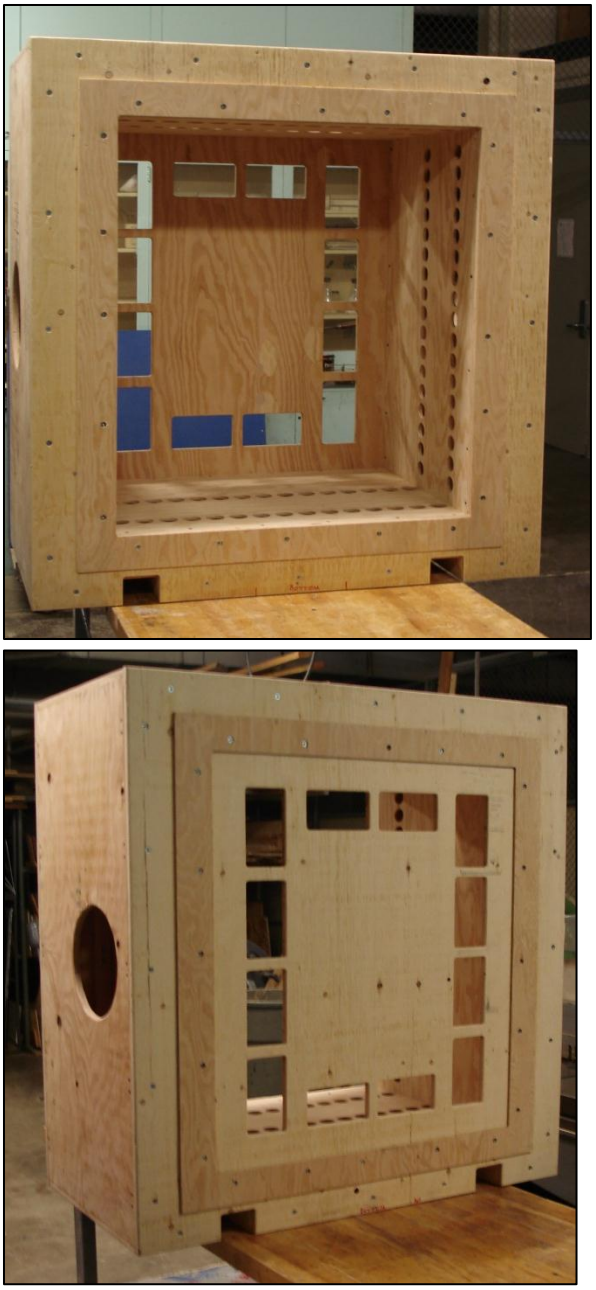

Figure 3.4.1 Turbulence Generator back (top) and front (bottom) taken from Erickson[24] (Refer to Erickson [24] for exact dimensions)

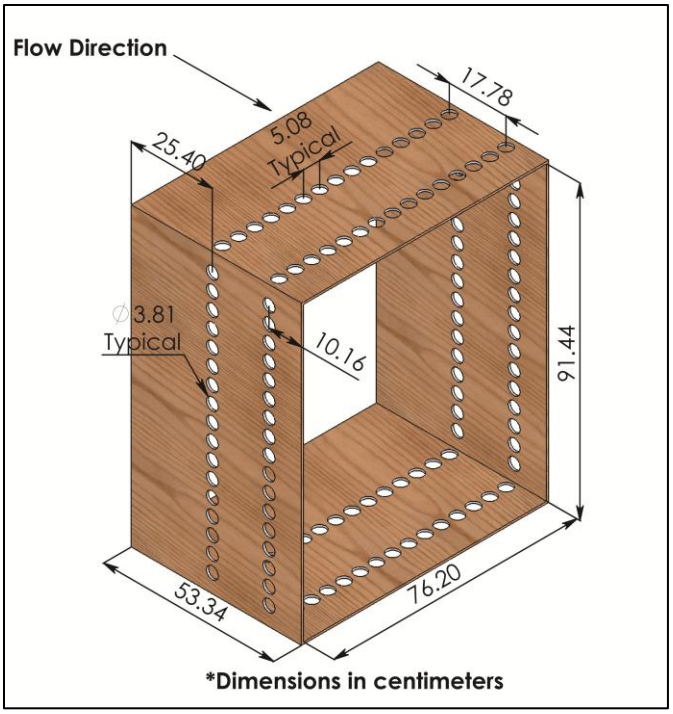

Figure 3.4.2 Turbulence Generator Mixing Volume

3.5 Nozzle

Downstream of the turbulence generator is a nozzle providing the necessary flow contraction. It was made of stainless steel with upstream and downstream flanges to connect to the rest of the section. With the dimensions shown in figure 3.5, the area ratio is 2.1:1. The walls of the nozzle are contoured to ensure that the streamlines are parallel at the inlet and the exit. The contour was designed by Erickson [24] using regression analysis.

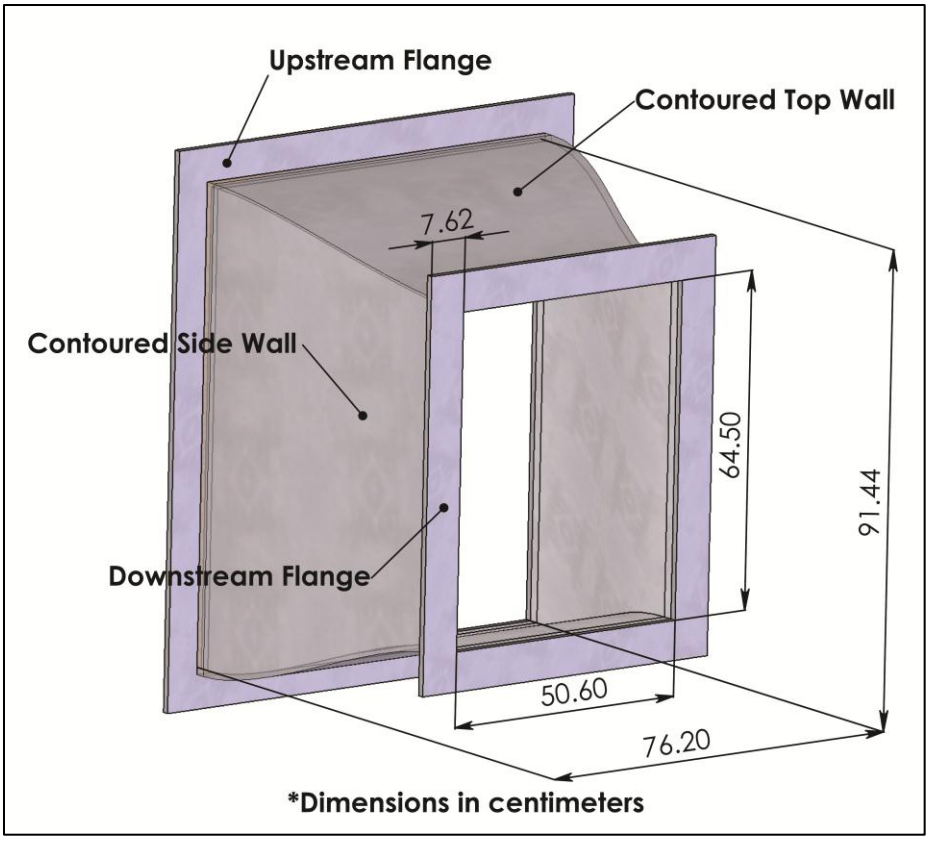

Figure 3.5 Flow Contraction Nozzle (Figure taken from Erickson[24])

3.6 Rotor Cascade Section

The rotor cascade used in the study consists of:

- Three blades forming two rotor passages
- Two contoured endwalls
- Tailboards and diffuser boards
- Leakage plenum and slot
- Approach flow temperature control slot
- Approach flow heaters

3.6.1 Rotor Blades

The rotor blades were made of a material called Medium Density Fiberboard (MDF). MDF is available in sheets; hence the blades were made by machining the sheets to the desired airfoil cross-section and then stacking them together using an adhesive binder.

Holes were drilled through the stacked sheets and fitted with nuts to hold the sheets under compression. The bonded sheets were sanded, finished with a polyurethane sealer and painted black.

Static pressure taps are located in the mid-span position of both the suction and pressure surfaces of the blades; hence ports were drilled up to the midspan position to accommodate the static pressure taps. The diameter of the ports is 0.64 cm and these pass about 3 mm below the blades surface ending at mid span [24]. Steel tubing with 4.7 mm internal diameter is inserted into the ports and secured in its position using room temperature vulcanizing silicone. The opposite end of the tubing extends about 2 cm out of the blades and can be connected to plastic tubing leading to the pressure transducers.

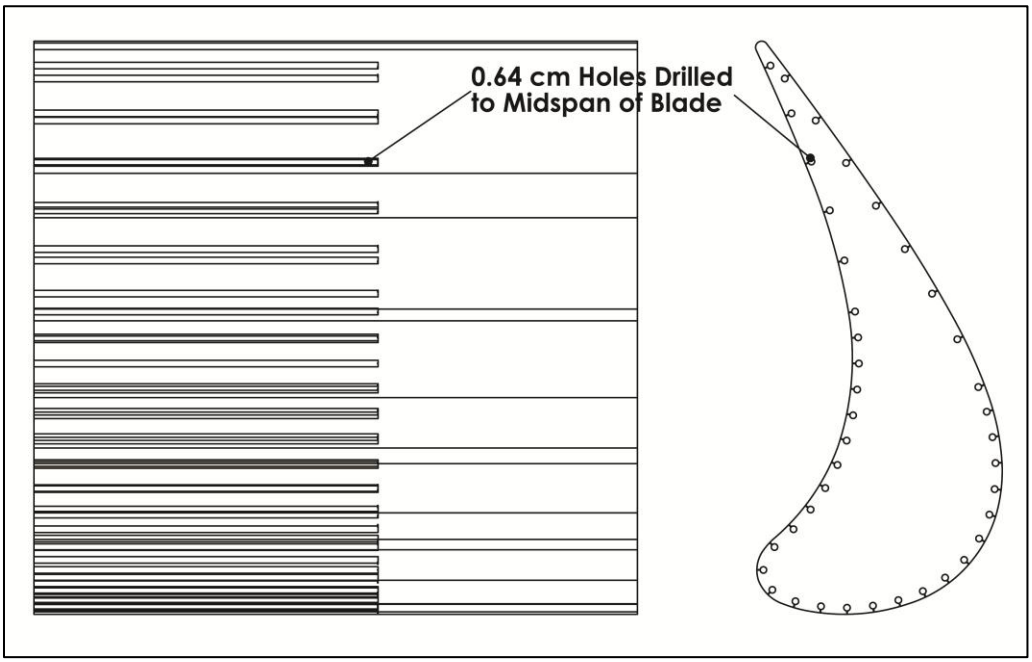

Figure 3.6.1 Ports for static pressure taps within the blades (taken from Erickson[24])

3.6.2 Hub Endwalls

One of the prime focuses of the present study is to investigate film cooling effectiveness of coolant in the leakage flow and in the near wall approach flow over a contoured endwall. The hub endwall is contoured in the axial direction, with the contour resembling a 'shark nose'. Another endwall contouring scheme namely 'Dolphin nose' has been previously investigated in studies by Erickson[24].The endwalls were made by Erickson[24] from MDF sheets in a manner similar to the blades i.e. by cutting the cross section and stacking the sheets together to get the desired height. Milling was done to obtain the necessary contouring scheme. The contouring scheme (Shark nose) is based on the designs provided by the sponsor, a turbine manufacturer, Solar Turbine Inc.

Figure 3.6.2 a shows section of the contoured endwall. The contouring begins at a streamwise location of X/C_{ax} =-0.14 and continues gradually upto X/C_{ax} = 0.31. At X/C_{ax} = 0.31 the height of the endwall equals the height of the stator lip. Figure 3.6.2 b shows a three dimensional view of the hub endwall (Shark nose profile).

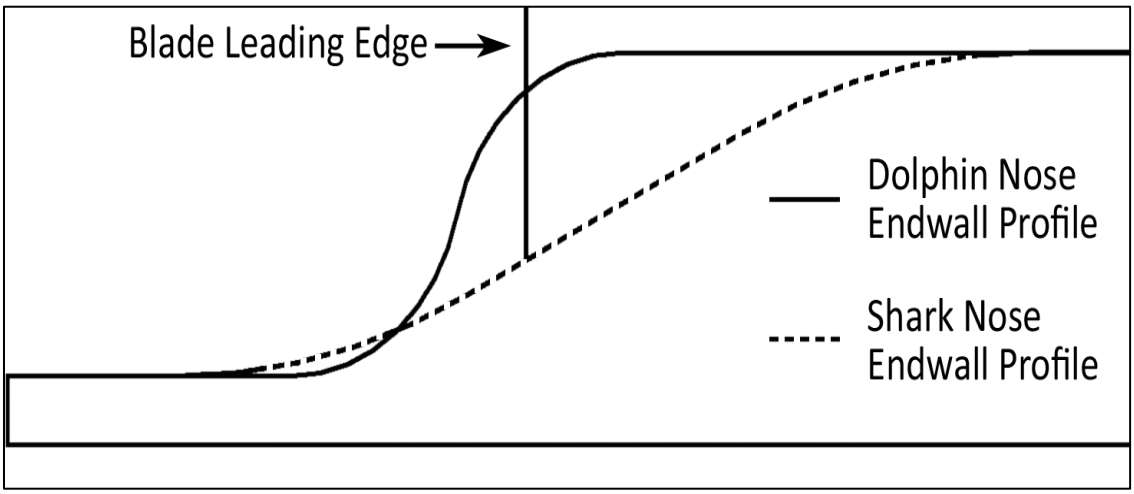

Figure 3.6.2 a Hub Endwall Contours (The Shark Nose profile is investigated in the present study; the Dolphin nose profile has been studied by Erickson[24])

The endwall opposite to the hub section is flat and provides access to the cascade section to make the necessary measurements.

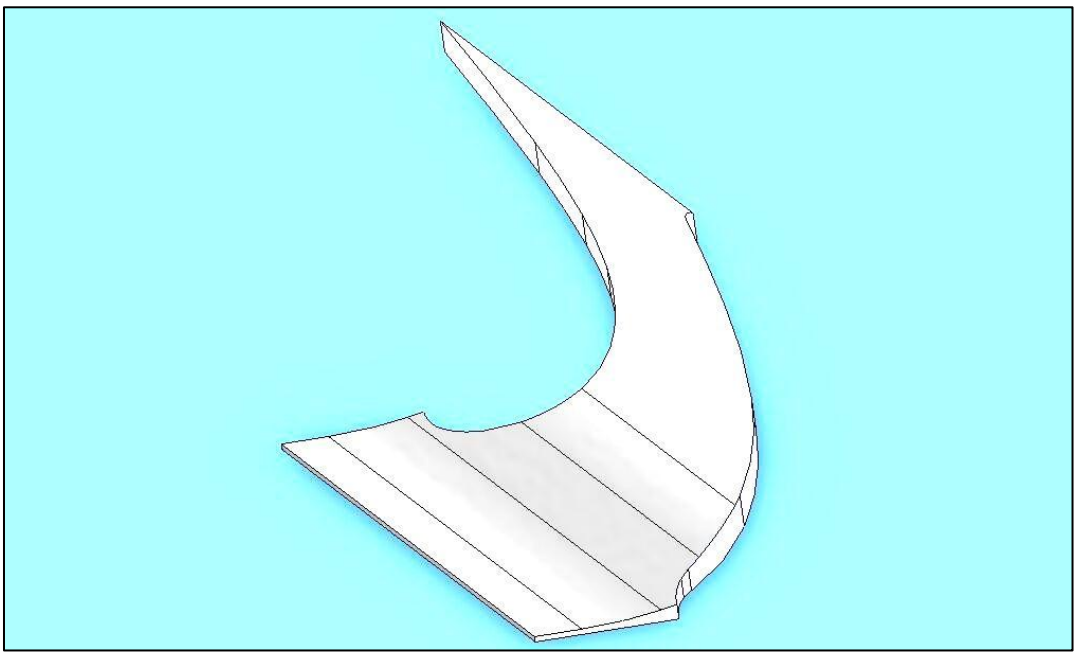

Figure 3.6.2 b Shark Nose Endwall

For more details about the manufacture and assembly of the endwalls, the reader is referred to Erickson [24].

Shark Nose Contour

The focus of this study is to document the performance of a 'shark nose' contoured endwall in presence of disc cavity leakage and approach flow temperature profile. It is thus necessary to understand the shark nose contour well.

Shown in figure 3.6.2 a is the shark nose contour superimposed with another representative contour called the dolphin nose that has been studied earlier by Erickson [24] .

The designs for both the contours were provided by Solar Turbines Inc.

The 'dolphin nose' contour begins at X/C_{ax} = -0.14 as concave curvature. This concavity is transformed into a convex curvature near the blade leading edge and finally the curvature ends at X/C_{ax} = 0.06.

In contrast the shark nose contour has a much more gradual beginning at X/C_{ax}= -0.14 and continues up to X/C_{ax}= 0.31.

This difference in the two types of contours is critical to the explanation of most of the observed effects discussed in the later chapters. By just a brief look at the two contoured profiles, one can say that the dolphin nose profile is expected give a rapid but short lived acceleration to the near wall fluid, owing to its steep gradient spread over a short distance near the beginning of the passage. On the other hand the shark nose endwall is expected to give a gradual but long lived acceleration to the near wall fluid owing to its milder gradient continuing deep into the passage.

Figure 3.6.2 c shows the overall cascade layout with table 3.1.1 showing the cascade dimensions.

Table 3.1.1 Cascade Dimensions

Scale Factor:	14.06
Chord Length (*C*):	55.79 cm
Axial Chord (C_{ax}):	43.20 cm
Pitch (p):	42.10 cm
Blade Aspect Ratio:	1.20
Inlet Flow Angle (α_1):	40.0°
Outlet Flow Angle (α_2):	70.0°
Inlet Duct Height (h_d):	64.50 cm
Inlet Duct Width (w_d):	50.60 cm
Blade-Endwall Corner Fillet Radius	2 mm

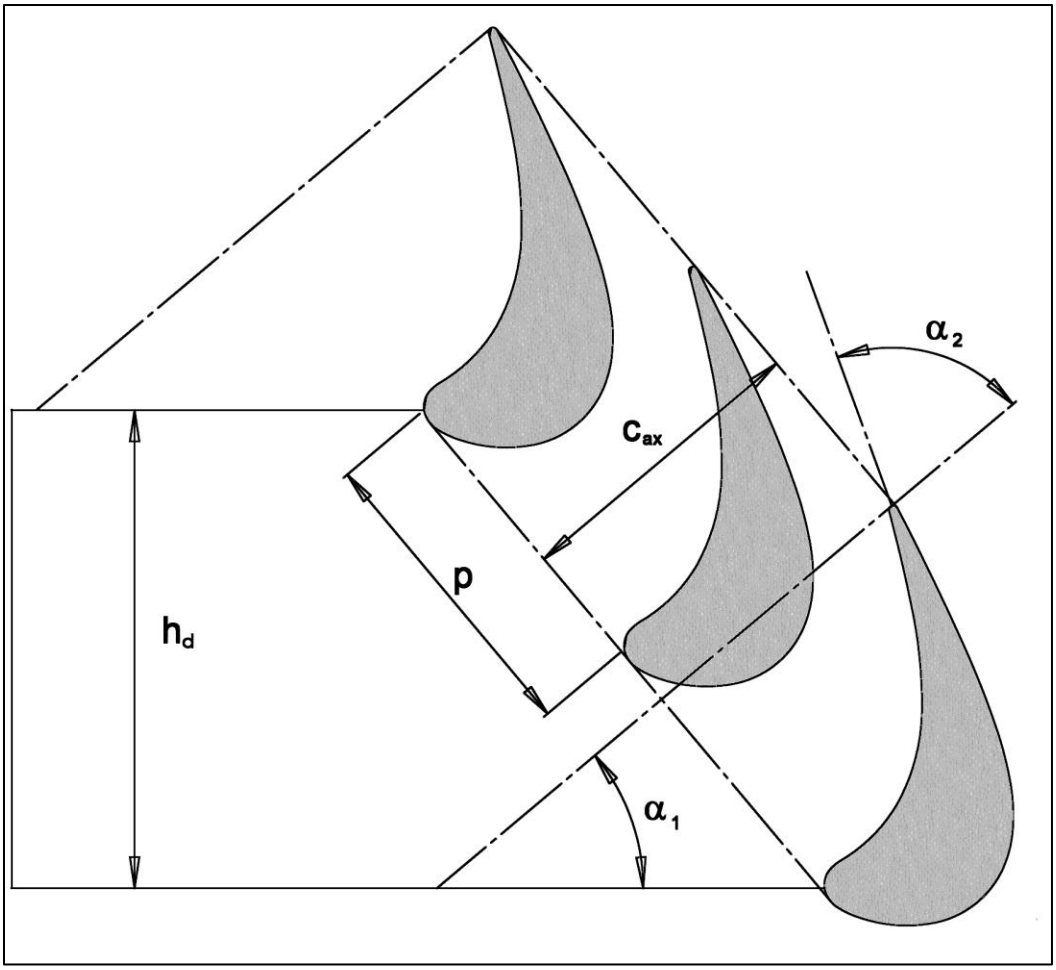

Figure 3.6.2 c Overall Cascade Layout

3.7 Leakage Plenum

In a gas turbine, there is a clearance between the stationary stator and the rotating rotor. In order to prevent the ingression of hot mainstream gases through this clearance a part of the flow from the compressor is bled through this clearance into the main flow. This bleed air is known as leakage flow or the purge flow and the path travelled by it is called the leakage path. The appropriate plenum for the leakage flow is designed for the study by taking cues from a modern gas turbine. Design dimensions were provided by Solar Turbines Inc. These were then scaled up to fit the test section geometry. The geometry studied is thus engine representative.

In the present study the leakage flow is fed by the leakage flow fan as described earlier. The flow enters a large acrylic box called the leakage plenum which simulates the disc cavity of a real engine. From the plenum the leakage flow enters the mainstream passage by means of the leakage slot which simulates the clearance between the stator and the rotor.

Shown in figure 3.7.1 is the leakage plenum geometry. For detailed dimensions of the plenum the reader is referred to Erickson [24].

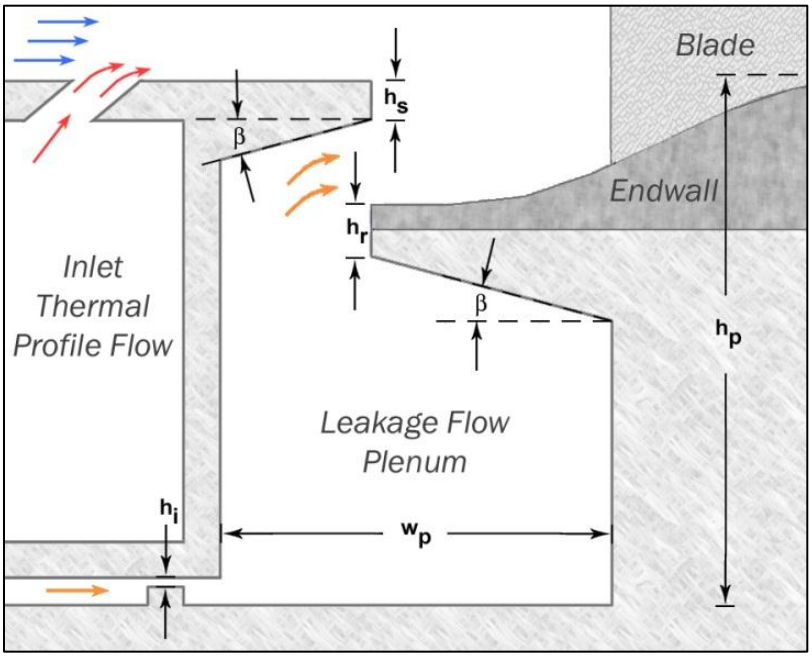

Figure 3.7.1 Leakage Plenum (Taken from Erickson [24])

The flow from the top left corner of the figure (colored blue) is the mainstream passage flow. Leakage flow enters from the bottom left corner through a contraction called the rim-seal gap. It then enters the plenum and then the passage through the leakage slot.

3.8 Approach Flow Temperature Control Slot

As shown in figure 3.7.1, upstream of the leakage slot, there is a 45 degree slot called the approach flow temperature control slot. Flow simulating the combustor liner coolant is fed through this slot. The approach flow temperature control fan draws in air from the

room and feeds it to a plenum that runs parallel to the nozzle walls though a PVC piping. Inside the piping resistance heaters have been installed, which heat the temperature control flow to a temperature that is enough to maintain the endwall upstream of the leakage slot at a temperature equal to the mean leakage flow temperature (8-10 ^{o}C above the mainstream flow temperature). Power to the resistance heaters is regulated by means of a Variac.

3.9 Approach Flow Heating Elements

This study focuses specifically on the effect of an engine representative approach flow profile and leakage flow on the adiabatic effectiveness values on the rotor endwall. Hence, establishment of an engine representative combustor exit temperature profile is important for the study. Since the near wall fluid including the leakage flow is supposed to be heated in the present study to achieve a temperature profile that qualitatively resembles the combustor exit temperature profile of a real engine, it is essential that some heating elements are installed in the approach flow upstream of the leakage slot so that the near wall flow is heated and progressively becomes cooler as one moves away from the walls. Four resistance heaters were placed at distances 3mm, 6mm, 9mm and 14 mm away from the wall at a distance X/C_{ax}= -0.5. These heaters were made by spirally winding a nichrome wire on a non-conducting rod about 1 cm in diameter. The heaters were connected to the power supply by means of a variac in order to regulate the power input to the heaters. By specifically varying the power input to each of the heaters and allowing them to reach steady state, one can establish the desired temperature profile.

3.10 Diffuser and Tailboards

The diffuser and the tailboards serve the purpose of effectively exiting the wind tunnel flow back into the room. Additionally, the tailboards help in achieving proper boundary conditions at the exit of the passages and in ensuring that equal amounts of flow pass through each of the two passages in the cascade section.

3.10.1 Diffuser

The flow is accelerated within the rotor passages. At the exit of the passage, its pressure is lower than the ambient (room pressure). In order to exit the flow to the room it is necessary that pressure is recovered from the flow. This is done by using a diffuser at the end of the passages. The front and the back walls of the diffuser are made of 1.27 cm thick sheets of acrylic with a length of 122 cm and width 50.8 cm. The side walls are made from 1.9 cm thick plywood. The geometry of the diffuser was designed by Erickson [24]. It has a half divergence angle of 7 degrees and streamwise length of 122 cm. The area ratio of the diffuser is 2.1. It is believed that this design is optimum for a turbulent flow, and separation effects are not present.

3.10.2 Tailboards

The tailboards are meant to maintain proper boundary conditions at the passage exit. These are connected to the airfoils at the exit plane. They are made of 0.16 cm thick acrylic polycarbonate sheets that are reinforced at equal distances with thick acrylic ribs. The ends of the ribs have projections that are used to fit the tailboards tightly with the sidewalls of the diffuser using C-clamps. The tailboards can be adjusted by tightening or loosening the clamps attached to the ribs. The final position is determined by measuring and matching the static pressure profiles between the two passages (discussed in chapter 6). The adjustment of the tailboard is done to either increase or decrease the area under a passage in a manner that the static pressure profiles of both the passages coincide with each other. This ensures that equal amounts of flow are passing through both the passages.

3.11 Wind Tunnel Access and Traverse System

Access to the wind tunnel for the purpose of measurement is obtained through the movable hole panel and the flat endwall. The flat endwall is made of different panels made of acrylic that are held together tightly by means of tap bolts. These acrylic panels and the movable hole panel can be moved around to take measurements across different points in the passage.

3.11.1 Movable Hole Panel

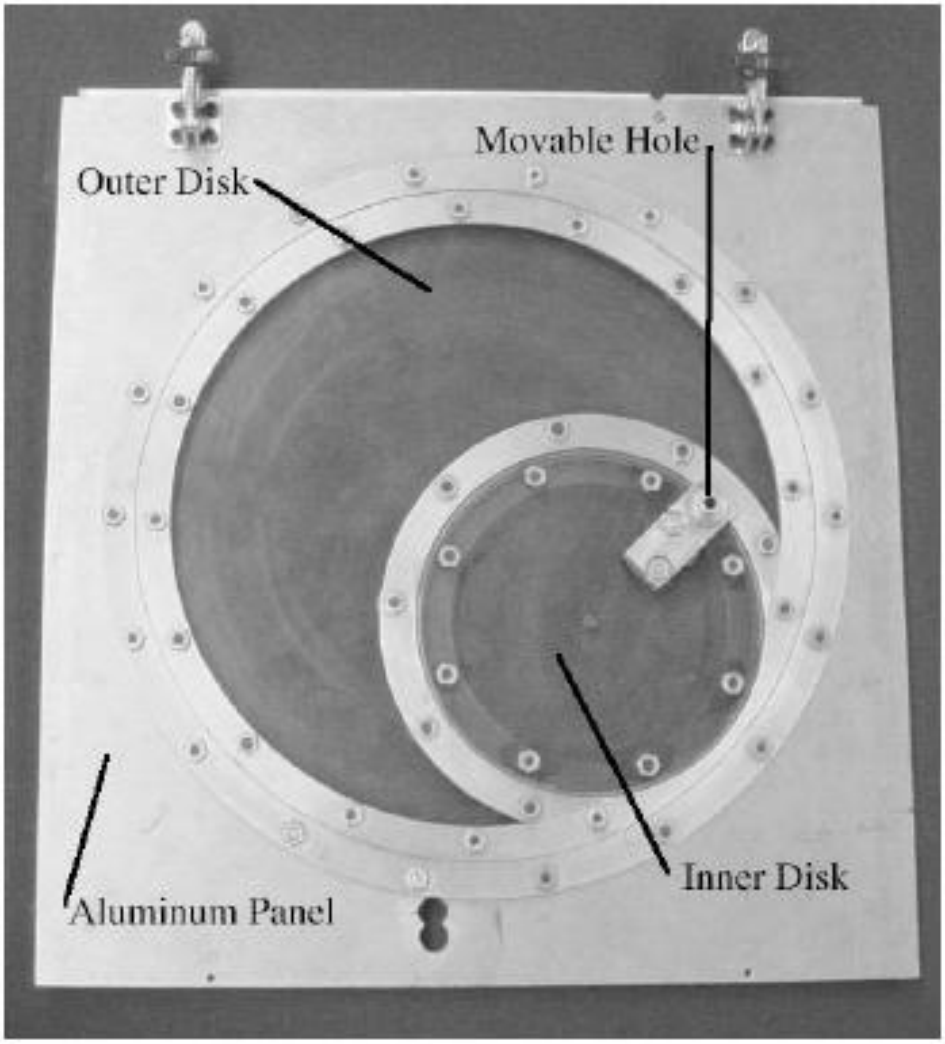

Figure 3.11.1 Movable Hole Panel (Erickson [24])

The movable hole panel is used for the purpose of supporting the probe holder (either the hotwire probe for velocity measurements or the thermocouple for temperature measurements). It consists of two circular discs supported within an aluminum disc. The inner disc has a hole at its edge for the insertion of the probe holder containing the probe. The inner disc rotates relative to the outer disc and hence the probe can be placed on any location on the outer disc. There are ball bearings between the inner and the outer discs

and also between the outer disc and the aluminum panel. To ensure smooth movement of the discs, these ball bearings need to be lubricated with time. There are tap bolts that hold the panel tightly with the rest of the panels of the flat endwall. The movable hole panel can be moved around and positioned at different locations on the flat endwall based on the location where the measurement is desired.

3.11.2 Automated 3-Axis Traverse System

The automated 3 axis traverse system consists of three Unislides, mounted mutually perpendicular to each other and can be traversed independently of each other. The movement of the Unislides is controlled by the MEDAQ software (Erickson[24]). The traverse arrangement is mounted on a table whose vertical height can be adjusted depending on the section of the passage where measurement is being made. For finer placement of the probe at a particular location, a joystick that controls the traverses in horizontal and vertical directions is used. This system allows measurements all across the endwall and also in the spanwise (endwall-normal) direction.

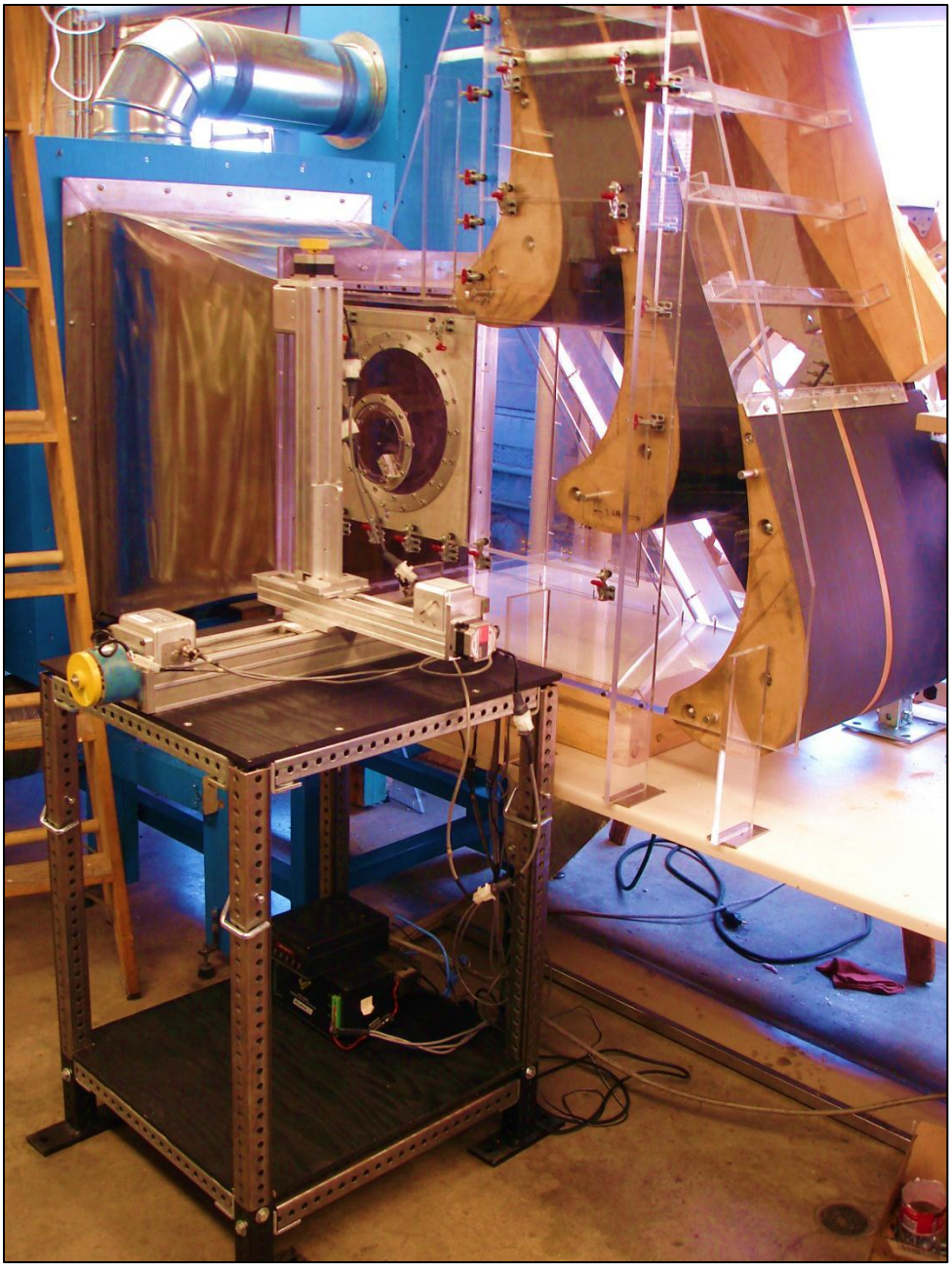

Figure 3.11.2 Automated 3-axis Traverse System

Chapter 4

Measurement Techniques and Principles

The present study involved measurements of velocity, pressure (both total and static) and temperature. This chapter explains the principle, calibration and steps involved in measuring these quantities. Also explained is the theory behind the measurement of various scales of turbulence.

4.1 Velocity Measurement: Hot Wire Anemometry

All velocity measurements in the study were made using hot wire anemometry. The principle behind this technique is the cooling of a heated probe by oncoming flow. The amount by which the heated probe gets cooled depends on the flow velocity; similar to a cylinder in cross flow situation and thus gives a measure of the flow velocity.

Most instruments use an electrically heated probe as the velocity sensor. If the pressure, composition and temperature of the oncoming fluid remains constant, the only parameter affecting the cooling of the heated probe is the fluid velocity [25].The instrument used for the present study is an A.A.lab AN-1005 hot wire bridge. The equipment works on the principle of constant temperature anemometry. The probe forms one of the resistors of a Wheatstone bridge circuit. When exposed to oncoming fluid flow, it is cooled by the fluid leading to a decrease in the resistance of the probe. This causes an imbalance in the Wheatstone bridge, and a proportional voltage is passed through the probe to heat it up and bring the bridge to balance again. Thus, this voltage is proportional to the oncoming fluid velocity. King [26] derived a linear relation between the voltage and fluid velocity, popularly known as the King's law, as shown below:

$$U^n = AV^2 + B \qquad (4.1)$$

Where n, A and B can be obtained by proper calibration.

4.2 Hot Wire Calibration

The calibration of the device was done using a calibration chamber designed by Wilson [27]. The chamber is supplied by pressurized air from the building. An inlet valve regulates the air flow through the chamber. Shown below is the schematic of the calibration chamber.

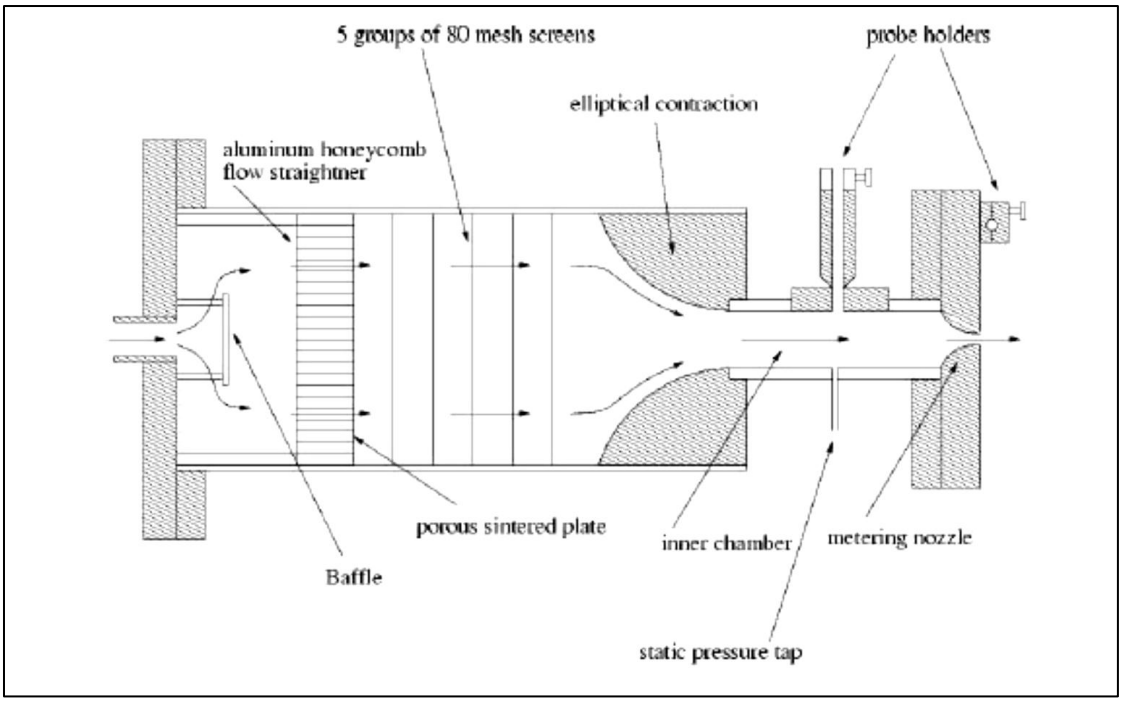

Figure 4.2.1 Hot Wire Calibration chamber schematic, adapted from Adolfson[28]

The building air enters the chamber and gets deflected by a baffle plate. Then, it passes through honeycomb aluminum flow straightener followed by a 2 mm thick plate of porous sintered stainless steel in order to damp out most of the turbulence present in it. An RTD is located upstream of the flow straightener to record the temperature inside the chamber. The flow straightener is followed by 5 sets if turbulence control screens. The

flow then passes through a 14:1 elliptical contraction and then to the calibration chamber. Finally it exits the chamber by means of a metering nozzle.

For the purpose of calibration, the hot wire probe was mounted in front of the metering nozzle such that the probe is normal to the flow direction. Care was taken that the probe is not too far away from the nozzle exit; otherwise diffusion effects would have an adverse impact on the calibration. The RTD was connected to a multimeter to get the resistance readings of the temperature probe. The static pressure tap at the calibration chamber was connected to a micro-manometer made by Dwyer. The flow through the chamber was varied by means of the regulating valves at the inlet. At each flow rate, the pressure difference between the chamber and the surroundings was measured from the micro-manometer. Also noted was the resistance shown by the multimeter.The voltage output by the hot wire bridge was also acquired at 1 kHz for 10 seconds by using the IOTECH ADC 488 along with the software MEDAQ. This procedure was repeated for 20 different reading by slowly increasing the flow. A MATLAB code (given in accompanying DVD) was used to process the results and obtain a velocity output. This velocity output was correlated with the voltage across the hot wire bridge to get an expression in accordance with King's law.

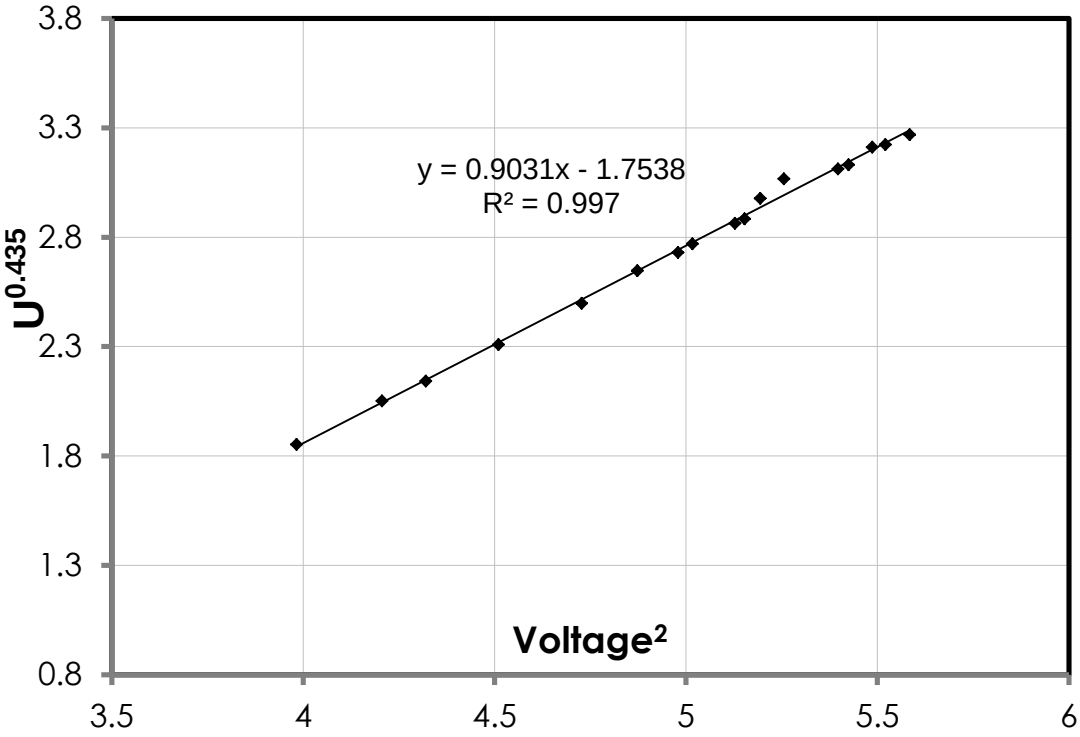

Figure 4.2.2 Hot Wire Calibration Curve

Shown is the linear curve obtained for the calibration of the hot wire probe. The calibration curve is :

$$U^{0.435} = 0.9031 * V^2 - 1.7538 \qquad (4.2)$$

It should be noted that this particular curve is given as an example. The probes must be calibrated often as the curves show drift with changing conditions.

4.3 Turbulence Measurements

The hot wire anemometry system together with the data acquisition hardware can sample data at a maximum frequency of 5 kHz. Since this is a fairly fast rate and the flow in the wind tunnel is stationary (mean quantities remain constant with time), the hot wire anemometry system can be used to measure several characteristics of turbulent flow such as:

- Turbulence Intensity (TI)
- Turbulent scales:
  - Integral Length Scale
  - Energy length scale
  - Taylor Microscale
  - Eddy Diffusivity

These measurements are essential in providing a complete description of the approach flow. These can also serve as input boundary conditions to computational researchers.

Turbulence Intensity

Turbulence Intensity is defined by the expression:

$$TI(\%) = \frac{u'_{rms}}{U} * 100 \qquad (4.3)$$

Physically it tells us what percentage of the mean velocity are the velocity fluctuations.

To measure turbulence intensity of the approach flow, velocity is sampled at 5 KHz for 60 seconds at a location upstream of the passage. The mean of all the data points is calculated as:

$$\bar{U} = \frac{\sum_1^N U(t)}{N} \qquad (4.4)$$

The velocity fluctuation at each data point is calculated by subtracting the velocity at that data point from the mean velocity.

$$u' = \bar{U} - U(t) \qquad (4.5)$$

The root mean square velocity fluctuation is calculated as:

$$u'_{rms} = \sqrt{\frac{\sum_{i=1}^{N} u'^{2}_{i}}{N}} \qquad (4.6)$$

Turbulence Spectrum and Scales

The turbulent kinetic energy is distributed among a wide range of fluctuation frequencies. These frequencies can be related to the length scales of turbulence using Taylor's frozen flow hypothesis [29]. In simple terms the turbulent fluctuations going past a sensor can be said to be frozen in time (partial derivatives w.r.t time of any property is zero) and hence the total change of the variable with time is only due to advection. The principles used in the measurement of turbulence energy density spectrum are discussed in this chapter. Energy spectrum is defined as the Fourier transform of the autocorrelation function. For a detailed description of the autocorrelation function the reader is referred to Tennekes and Lumley [29] and Smol'yakov [30]. The value of the energy spectrum gives the mean energy contained in that fluctuation frequency.

In order to obtain the energy density spectrum (or power spectrum), the hot wire probe is exposed to the oncoming flow at one point slightly upstream of the passage inlet. Data are then sampled at 5 kHz for 60 seconds. It is essential that errors due to stray frequencies (aliasing) are avoided, hence this time dependent fluctuation velocity is passed through a low pass filter with a cut off frequency of N/2 (Nyquist Criterion). All frequencies that are greater than the cut off frequency are filtered off.

Using the calibration curve as discussed earlier, the time varying velocity is obtained. The velocity fluctuation is then calculated as:

$$u'(t) = \bar{U} - U(t) \qquad (4.7)$$

Next, it is essential to transform the velocity fluctuations in the time domain to the frequency domain. A MATLAB based Fast Fourier Transform (FFT) function is used for

the purpose. The FFT is based on the Cooley-Tukey FFT algorithm is used for the purpose . The j^{th} element of the function is given as:

$$\varphi(j) = \frac{1}{\sqrt{N}} \sum_k u(t)_k e^{i.\frac{2\pi j}{N}.k} \qquad (4.8)$$

Where : k= index of *u(t)* array

N = Total number of samples (sampling frequency*time)

It should be noted that MATLAB does not use the normalizing constant $1/\sqrt{N}$ by default, hence each element of the output of the FFT function must be divided by the normalizing constant. This procedure would be differing depending on the software used for signal processing.

An array for frequencies is produced by using the expression:

$$\omega_j = \frac{\omega_s}{N} j \qquad (4.9)$$

The energy density is calculated using the expression provided by Stull [31].

$$E(\omega) = \frac{\phi(\omega)^2_{real} + \phi(\omega)^2_{imag}}{\Delta\omega \, N/2} \qquad (4.10)$$

Where $\Delta\omega = \frac{\omega_s}{N}$

For one measurement, the signal appeared to be quite scattered. Hence about 15 measurements were taken and the profiles were averaged out to get the mean energy density spectrum. The energy density plotted against the frequency gives the energy density spectrum as shown in figure 4.3.1. The ‘blue’ plot is the mean spectrum and the ‘green’ plot is the one obtained by applying a smoothening function to the mean spectrum.

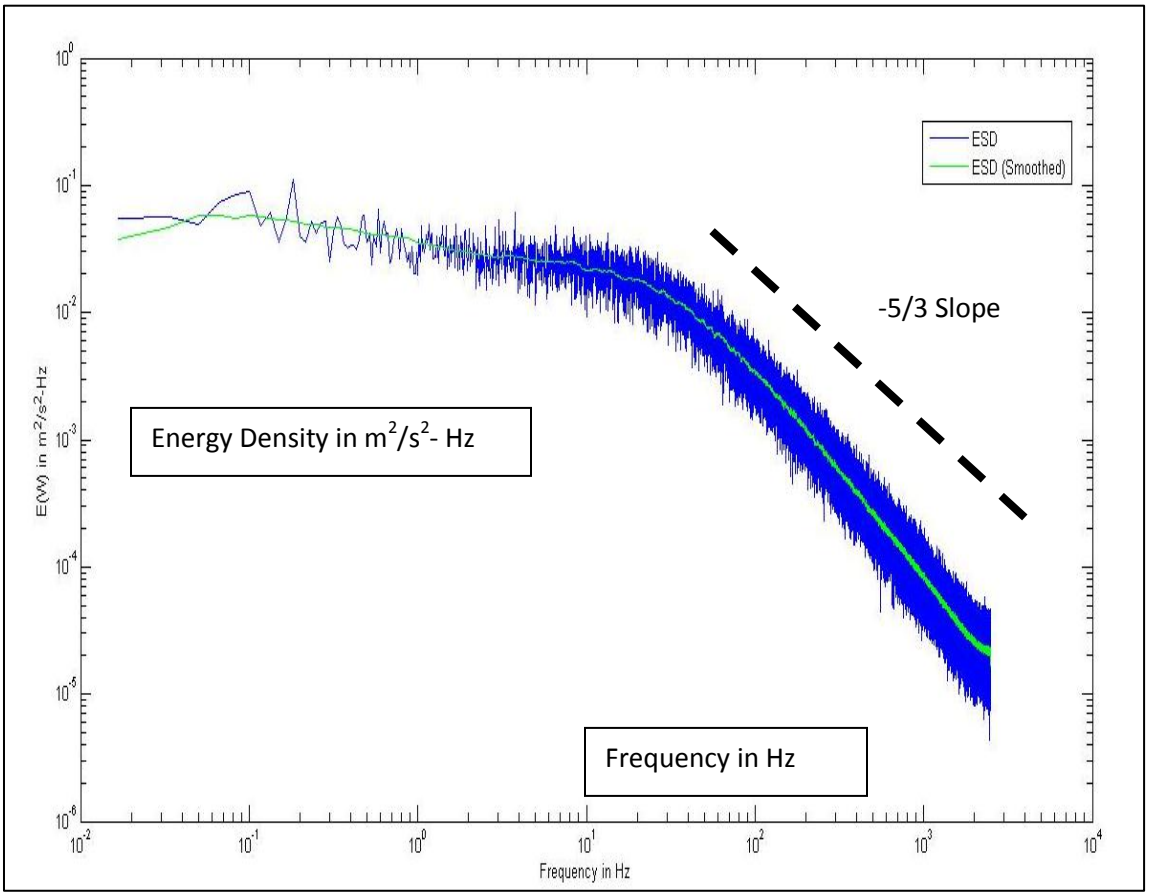

Figure 4.3.1 Energy Density Spectrum (Plot of Turbulence Kinetic Energy vs. Frequency of Fluctuations)

Figure 4.3.2 shows the corresponding energy spectrum. It can be seen that most of the turbulence kinetic energy peaks around a particular fluctuation frequency.

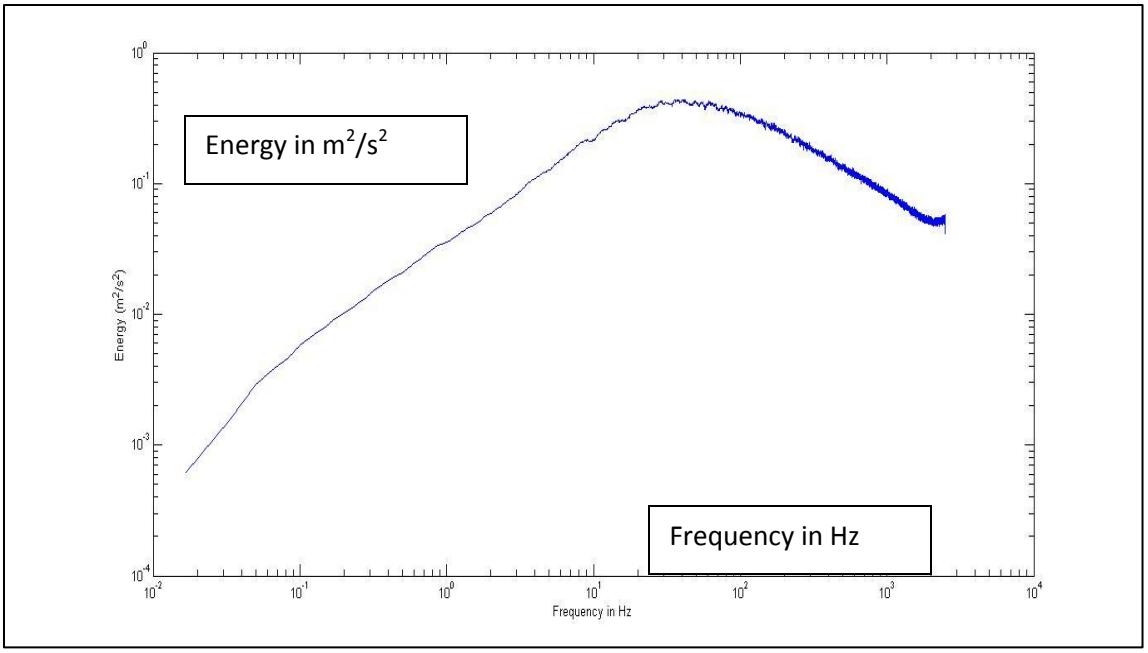

Figure 4.3.2 Energy Spectrum (Plot of Turbulence Kinetic Energy vs. Frequency of Fluctuations)

The energy density spectrum can be used to calculate different scales of turbulence as described below.

Integral Length Scale

Physically, this scale represents a characteristic length scale for the largest eddies in the flow.

From the energy density spectrum, this quantity can be calculated using the expression given by Hinze[32]:

$$\Lambda = \lim_{\omega \to 0} \frac{U_{avg} E(\omega)}{4u_{rms}^{\ 2}} \qquad (4.11)$$

Turbulence Dissipation Rate

This quantity gives the rate at which turbulence kinetic energy is converted into internal energy by viscous dissipation. This is calculated from the energy density spectrum in the -5/3 slope range. This range is called the inertial subrange. Physically, in this range, the

smaller eddies receive energy from the larger eddies and ultimately dissipate due to viscosity. The inertial subrange follows an empirical relationship given by Ames and Moffat [33]

$$E(\omega) = \frac{18}{55} A\varepsilon^{2/3}\omega^{-5/3}\left[\frac{2\pi}{\bar{U}}\right]^{-2/3} \qquad (4.12)$$

Where A is a constant taken as 1.62 by Ames and Moffat [33]

ε is the dissipation rate in m^2/s^3

Energy Length Scale:

This quantity indicates the size of the mean energy containing eddy. Ames and Moffat [33] express this quantity as:

$$Lu = 1.5\frac{u_{rms}^{3}}{\varepsilon} \qquad (4.13)$$

Taylor Micro Scale

This is the representation of the size of the smallest eddy that can exist in the flow, before viscous dissipation. It is located in the region where intertial subrange ends and viscous dissipation begins.

$$\lambda = \sqrt{\frac{15\nu u_{rms}^{2}}{\varepsilon}} \qquad (4.14)$$

4.4 Static and Total Pressure Measurement

Pressure measurements are made as part of flow qualification process. Blade static pressure profiles are measured along both suction and pressure surfaces of the blades forming the two passages of the cascade. Also, the static pressures normalized as a pressure coefficient given as

$$C_P = \frac{P_s - P_{s0}}{P_{t0} - P_{s0}} \qquad (4.15)$$

Where P_{t0} is the total pressure at the inlet of the passage. P_{s0} is the static pressure at the inlet, and P_s is the static pressure along the blade surfaces. The measurement of each of the pressures is described in chapter 5. In this section, the broader aspect of measurement of static and total pressure is discussed.

Static and total pressures are measured by a telescopic pitot tube. It is connected by means of plastic tubing to a Validyne pressure transducer, which converts pressure into a voltage signal that can be sampled by a data acquisition unit. Also, the static pressure taps along the blade surfaces are connected by means of plastic tubing to the pressure transducer. The following section discusses in detail the working principle and calibration procedure of the pressure transducer.

Pressure Transducer Working Principle

Pressure transducers are used for sampling pressure measurements at a high frequency. Variable reluctance type pressure transducers made by Validyne Engineering Corporation (model DP15) are used in the study. The transducers have a stainless steel diaphragm with a pressure range of 5.5 inches water. It contains a magnetically permeable stainless steel diaphragm clamped between two blocks of stainless steel. Embedded on each block is an E-shaped core with inductance coils. Under normal conditions equal gaps exist between the diaphragm and the E-shaped cores. When pressure is applied across one of the pressure ports, the diaphragm deflects, resulting in a reduction of one gap and an increase in the other. This produces a change in magnetic reluctance, leading to an increase in the inductance value of one coil and a decrease in the inductance value of the other. The transducer is connected to an AC bridge circuit whose output is, in turn, fed to a carrier demodulator which amplifies the AC signal and rectifies it to produce a +/- DC voltage. The sign of the DC voltage depends on the direction in which the high pressure is applied.

Transducer Calibration Process

Transducer calibration is done to derive a relationship between the differential pressure (gauge pressure) applied across the transducer's ports and the DC output produced by the carrier demodulator (CD15). The calibration jet facility used in the hot wire calibration process was used as a pressure source for transducer calibration. An inclined tube manometer was used for the differential pressure measurement produced by the calibration jet. A voltmeter was used to set the appropriate DC output range for the CD15. Data acquisition was done with the help of IOTECH ADC488 digitizer.

The output of the pressure transducer was connected to the CD15 input using Validyne's 4 pin cable. The output of CD15 was connected to a multimeter. Initially both ports of the pressure tranducer were left open. The 'ZERO' of the CD15 was adjusted so that the multimeter read 0V DC. The calibration jet's static pressure tap was connected to the high pressure port of the transducer and to the inclined tube manometer using equal length of plastic tubing. The other port of the pressure transducer was left open to the surroundings. Next the throttle to the calibration jet inlet was opened fully so that the inclined tube manometer read 5.5 inches of water. The 'SPAN' of CD15 was adjusted so that the multimeter read 10 V. This procedure configured the pressure transducer for +ve pressure values of 0-5.5 inches of water resulting in DC output of 0-10 V. If the connection to the pressure ports is reversed the transducer will be reading negative pressures. Next, the output of the CD15 was connected to the data acquisition unit by BNC cables. To begin the calibration process, the throttle of the calibration jet was slowly opened and the ΔP (difference of absolute and atmospheric pressure) was measured in inches of water from the inclined tube manometer. The DC output of CD15 is sampled at 1 kHz for 30 seconds. This procedure was carried until significant number of points between 0 and 5.5 inches of water were sampled. Now the connection to the pressure ports is reversed, meaning the port that was connected to the calibration jet's static pressure tap was now left open to the surroundings and the other port which was open to the surroundings was now connected to the calibration jet's static pressure tap.

Now the earlier procedure is repeated from 0-5.5 inches of water, with the transducer flexing in the opposite direction and giving negative DC output.

For each pressure input, the DC voltages sampled for 30 seconds were averaged. This gave one ΔP and one V for each point. A cubic polynomial fit was made to derive a relation between ΔP and V.

Figure 4.4.2 shows the arrangement for calibration of pressure transducers.

Figure 4.4.3 shows a sample plot for pressure transducer calibration. A slight non-linearity is observed at the high pressure range which might be due to the non-linear elastic stretching of the diaphragm. But since this effect is towards the high pressure range which is not reached in the wind tunnel, it is ignored.

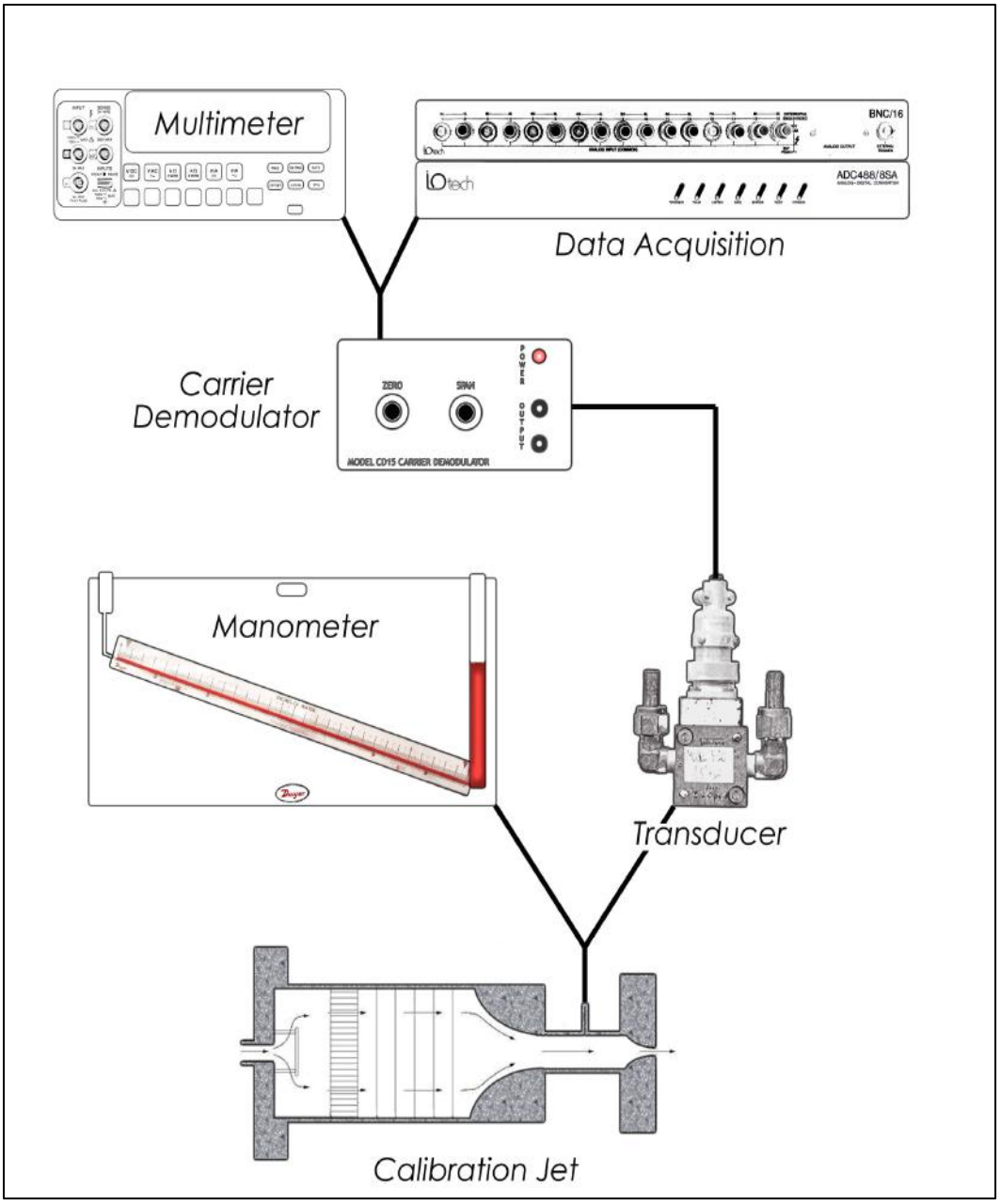

Figure 4.4.2 Schematic Set up for Pressure Transducer Calibration (Figure taken from Erickson [24])

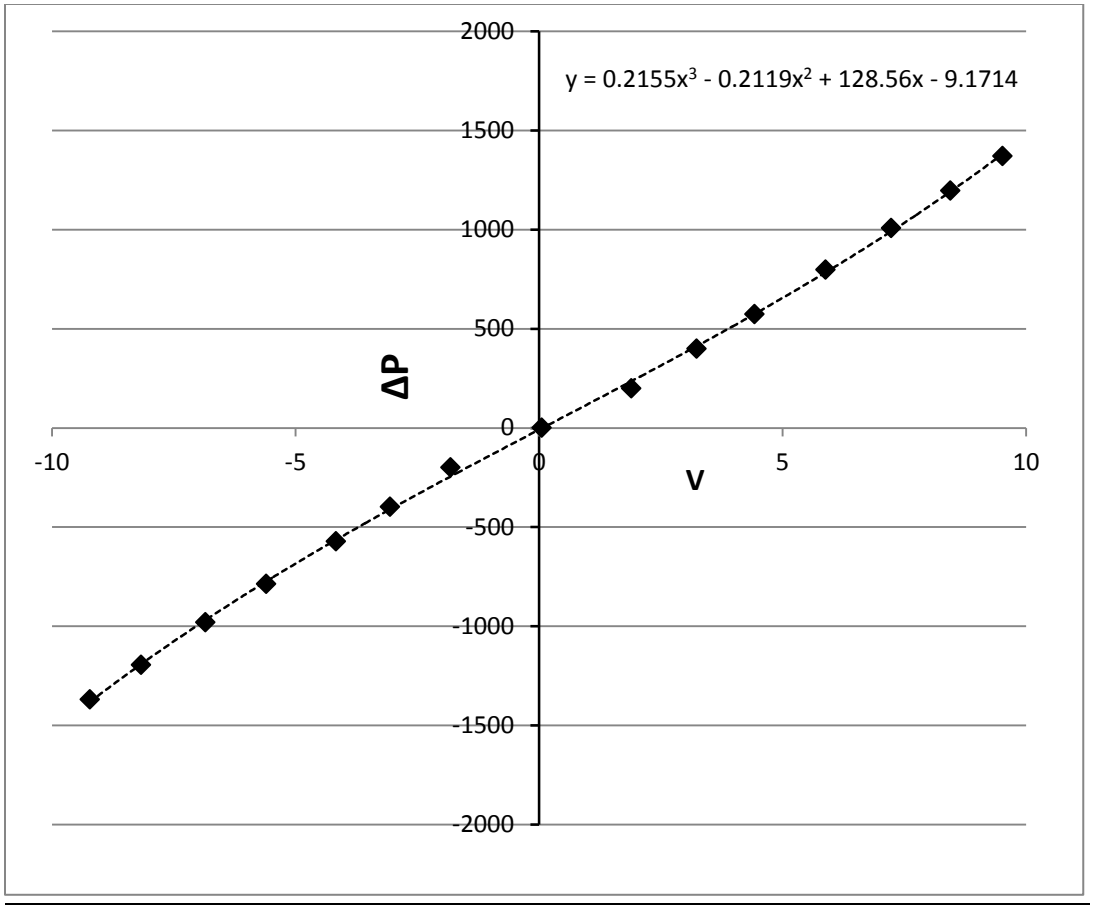

4.4.3 Sample Pressure Transducer Calibration Curve

4.5 Other Pressure Measurement Devices

Besides the pressure transducers, several other devices were used to aid pressure measurements. These were:

- Pitot Static Tubes
- Inclined Tube Manometer
- Micro-manometer

Pitot Static Tube

The Pitot static tube is a simple probe for differential pressure measurement. It can be used to measure both stagnation and static pressures. Along the perimeter of the barrel of the Pitot tube are tiny perforations. Flow streamlines are parallel to these perforations and hence these measure the static pressure in the flow.

The flow stagnates along the nose of the Pitot tube, hence stagnation pressure is measured at the nose. The difference between the static and stagnation pressures gives the velocity head of the flow. There are separate conduits within the Pitot tube for measurement of static and stagnation pressure. These conduits can be connected to a differential pressure measuring instrument such a a manometer or a pressure transducer by means of proper tubing.

Inclined Tube Manometer

An inclined tube manometer is used for differential pressure measurements that are necessary for leakage flow rate measurements and pressure transducer calibration. A Dwyer inclined tube manometer with a range of 0-6 inches H_2O is used in the present study. The instrument has two ports that can be connected to the flow across which the pressure drop needs to be measured. The liquid within the manometer is red gage oil. Generally, the high pressure end of the flow is connected to the inclined tube. The reported accuracy of the instrument is 0.01 inches H_2O (2.5 Pa).

U tube Manometer

The U tube manometer is used for measurement of pressure in the range of 0-1 inches H_2O. This measurement is required in the hot wire calibration process. A Dwyer Microtector model 1430 is used for the purpose. This device has a range of 0-1" H_2O with a resolution of 0.001 inches H_2O. The device contains a mixture of distilled water and Dwyer A 126 fluorescein as the fluid. When the micrometer pin touches the fluid, a closed electrical circuit is formed leading to the deflection of the ammeter pointer. Thus an accurate measurement of the liquid level can be read off the micrometer scale.

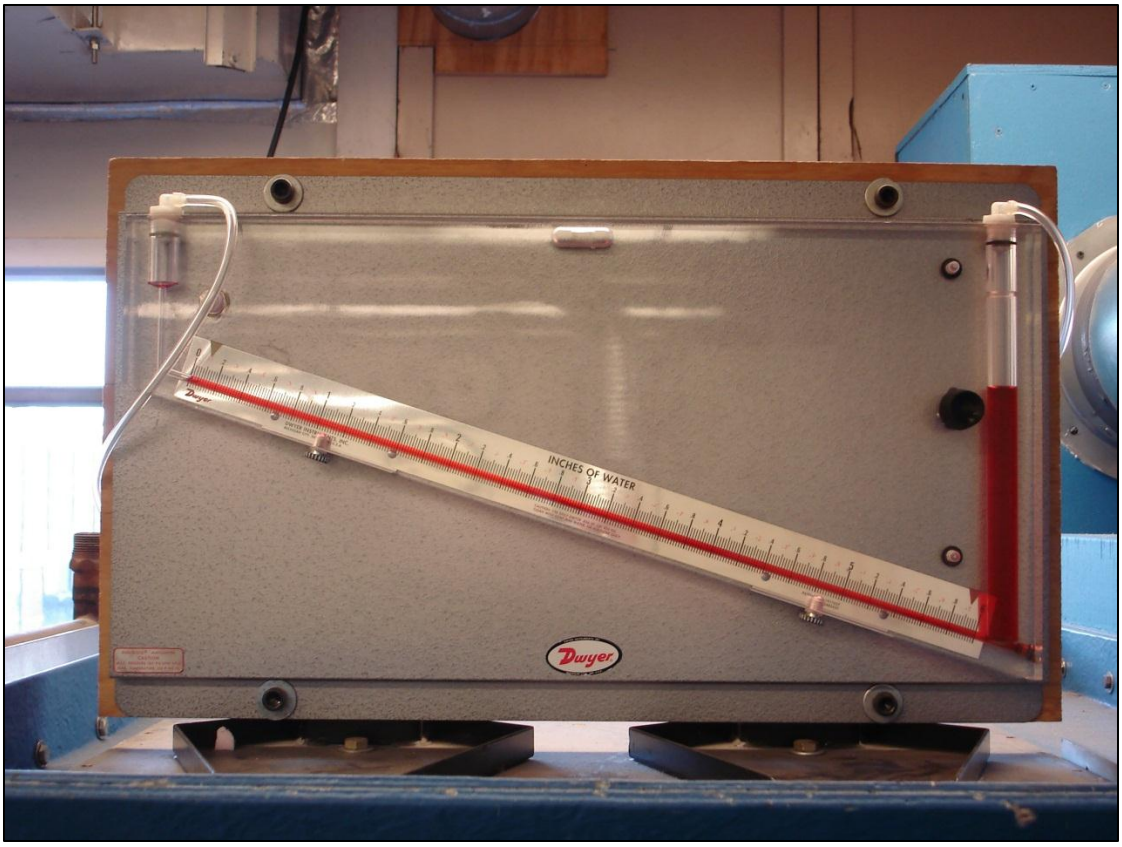

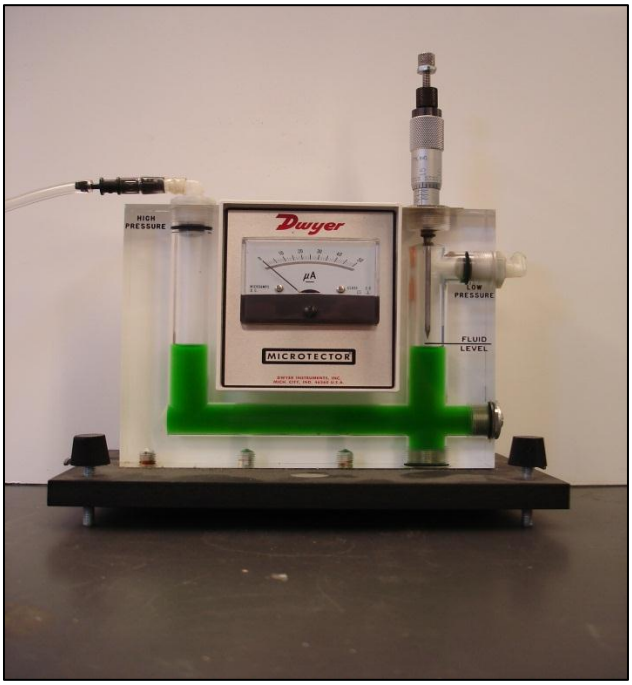

Figure 4.5.1 Inclined Tube Manometer (top) and Dwyer Microtector (bottom)

4.6 Measurement of Leakage Flow

A Laminar Flow Element (LFE), manufactured by Meriam instruments was used to measure the leakage flow rate. The inlet and the outlet of the LFE was connected to an inclined tube manometer to get the pressure drop across the LFE. This pressure drop is then used to calculate the leakage flow rate using a calibrated expression provided by the manufacturer:

$$Q = (50.0651 * \Delta P - 0.0692834 * \Delta P^2) \frac{\mu_{std}}{\mu_f} \qquad (4.16)$$

Where,

Q= Actual Flow Rate in ft^3/min.

ΔP= Pressure Drop Across the LFE in inches of water

μ_{std} = Dynamic Viscosity of Air at 70^o F.

μ_f = Dynamic Viscosity of Air at the Test Conditions and Relative Humidity

The viscosity correction ratio in equation 4.16 is obtained from tables in [34].

4.7 Temperature Measurements

All the temperature measurements in the present study were made by using Omega Type E thermocouples. Data were acquired using and Agilent 34970A data acquisition unit. The basis of operation of a thermocouple is the principle known as 'Seebeck effect'. As per this principle, temperature differences across a circuit lead to change in its electric potential. A thermocouple is made by making a junction of two dissimilar metals and exposing the junction to the desired location of temperature measurement. The thermocouple can only measure the temperature difference across two such junctions- one which is exposed to the location of the temperature measurement known as the hot junction and a second reference junction which is exposed to a known temperature (lower than the temperature to be measured) known as the cold junction. Often this reference

junction is located in an ice bath, so that the reference temperature is 0 ^{O}C. In the present study the Agilent 34970A unit has its own internal cold junction compensation, eliminating the use of a reference junction. The use of the device's internal cold junction compensation was deemed fit for the study as only temperature differences (ΔT) were required to be measured. Care must be taken while using the same method for measuring absolute temperatures as the internal cold junction compensation may add additional uncertainties. The data acquisition unit also has its own voltage-to temperature conversion based on N.I.S.T data (Burns et al. [35]). In order to ensure there were no major errors with the device a calibration check was performed by Erickson [24]. The reader is referred to Erickson [24] for a detailed description of the calibration principle. It was pointed out that no further check is necessary on the device. However, for additional confirmation of the accuracy of the device another check was done before beginning the measurements. A match between the temperatures of water in a well stirred bath heated to the a temperature of about 35^{O} C, indicated by a liquid in glass thermometer and the Agilent 34970A read out indicated that the device is functioning properly for the temperature range used in the study. As stated earlier, since temperature differences (ΔT) were being measured, the uncertainty associated with this method is low.

Chapter 5

Approach Flow Qualification

It is essential to establish that the flow approaching the stationary blade row passages is engine representative. This chapter explains the measurements made for the purpose of approach flow qualification and the results obtained. The following measurements were made:

- Blade Static Pressure Profiles
- Inlet Plane Velocity Field
- Inlet Plane Turbulence Field
- Inlet Plane Turbulence Spectra

5.1 Blade Static Pressure Profiles

Measurements of static pressure profiles along the blade surfaces is an important step to ensure flow periodicity i.e. equal amount of flow is passing through the two passages. If not, the tail boards at the exit of the passages must be adjusted until periodicity is ensured. Adjustment of the tailboards either increases or decreases the static pressure within one passage relative to the other, thus ensuring periodicity. Static pressure taps were located along both the suction and the pressure surfaces of the blades. These taps were connected to a switchboard of pressure valves through necessary tubing. The switchboard had single tubing going into the high pressure side of a Validyne^{TM} pressure transducer. By switching on a particular valve, the static pressure tap to which the valve is connected to, can be made active, and hence static pressure at that particular location on the blade can be measured using the calibration curve for the pressure transducer

discussed in chapter 4. The measured static pressures were non-dimensionalized as a pressure coefficient given by:

$$C_P = \frac{P_S - P_{Si}}{0.5\rho V_i^2} \qquad (5.1)$$

Where, Ps = Static pressure at a particular location on the blade

P_{Si} = Static pressure at the inlet to the blade passages

V_i = Velocity at the inlet to the blade passages

ρ = Density of the fluid i.e. air

In order to obtain P_{Si} and V_i, the total and static pressures were measured at the exit of the passages using a Pitot tube. The, difference between the two gave the velocity head from which the velocity at the exit of the passages, V_e was obtained. Then, using the continuity equation, the inlet velocity was obtained as:

$$V_i = \frac{A_i V_e}{A_e} \qquad (5.2)$$

Where, A_i = Passage inlet area

A_e = Passage exit area

Since the test facility is a stationary cascade and the losses are low, the total pressure measured at the exit was nearly the same as the total pressure at the inlet. Thus, by

subtracting the inlet velocity head from the total pressure at the exit, the static pressure at the inlet, P_{si} was obtained.

This method of obtaining static pressure at the inlet was considered to be more appropriate than direct measurement with the help of a static Pitot tube at the inlet because the flow at the entrance to the passages is of high turbulence intensity with large scale eddies. This could lead to inaccuracies in the measurement by a static pressure tap which requires fairly well behaved streamlines for accurate measurements.

The total and static pressure taps of the Pitot located at the exit of the passages were connected by suitable tubing to the high pressure ends of the two separate pressure transducers. The pressure transducers were connected to an Iotech ADC488 analog to digital converter for data acquisition. Data were sampled at 1 kHz for 30 seconds using a program, MEDAQ, written by Erickson [24]. Figure 6.1 shows the non-dimensional pressure coefficient plotted against X/C, where X is the distance along the blade surface from the leading edge and C is the true chord length of the blades. Positive X/C values denote suction surface and negative values denote pressure surface. Passage 1 is bound by the suction surface of blade 1and the pressure surface of blade 2. Passage 2 is formed by the suction surface of blade 2 and the pressure surface of blade 3. (Refer to figure 3.6.2 c, overall cascade layout)

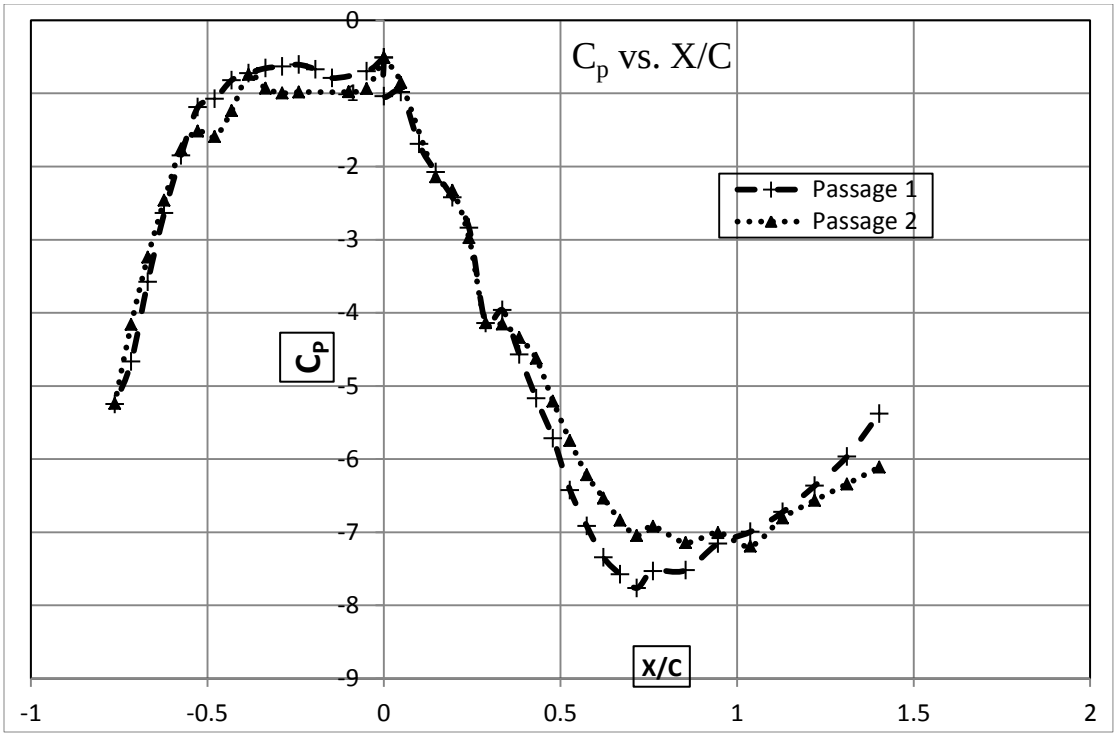

Figure 5.1.1 Non-dimensional static pressure profiles along blade surfaces

It can be seen in figure 5.1.1 that there are regions along the blade surfaces where the non-dimensional static pressure profiles match fairly well for both passages. There is a region around the throat where the profiles are separated on the suction surface. Also, along the pressure surfaces, small differences can be seen near the stagnation point X/C=0. Repeated adjustments of the tailboards led to the same profiles being generated. However, such small differences were considered tolerable for our study and were not believed to have a drastic impact on the measurements. Also, these pressure profiles match closely with those obtained by Erickson [24] on the same test facility.

5.2 Inlet Plane Velocity Field

The approach flow velocity distribution was obtained at a plane upstream of the entrance to the passages (X/C_{ax}=-0.58). A TSI 1218 boundary layer hot wire probe was used for the measurements. The use of a boundary layer allowed velocity measurements close to the wall. The probe was held by a probe holder and was inserted into the flow field

through the moving hole panel and was traversed over the entire inlet plane with the help of the three axis traversal mechanism. Data were sampled at 5 kHz for 30 seconds by means of an IOTECH ADC488 analog to digital converter. Velocity was obtained using the hot wire calibration curve discussed in chapter 4. Figure 5.2.1 shows the inlet plane velocity field. This contour plot has been generated by TECPLOT 360 software.

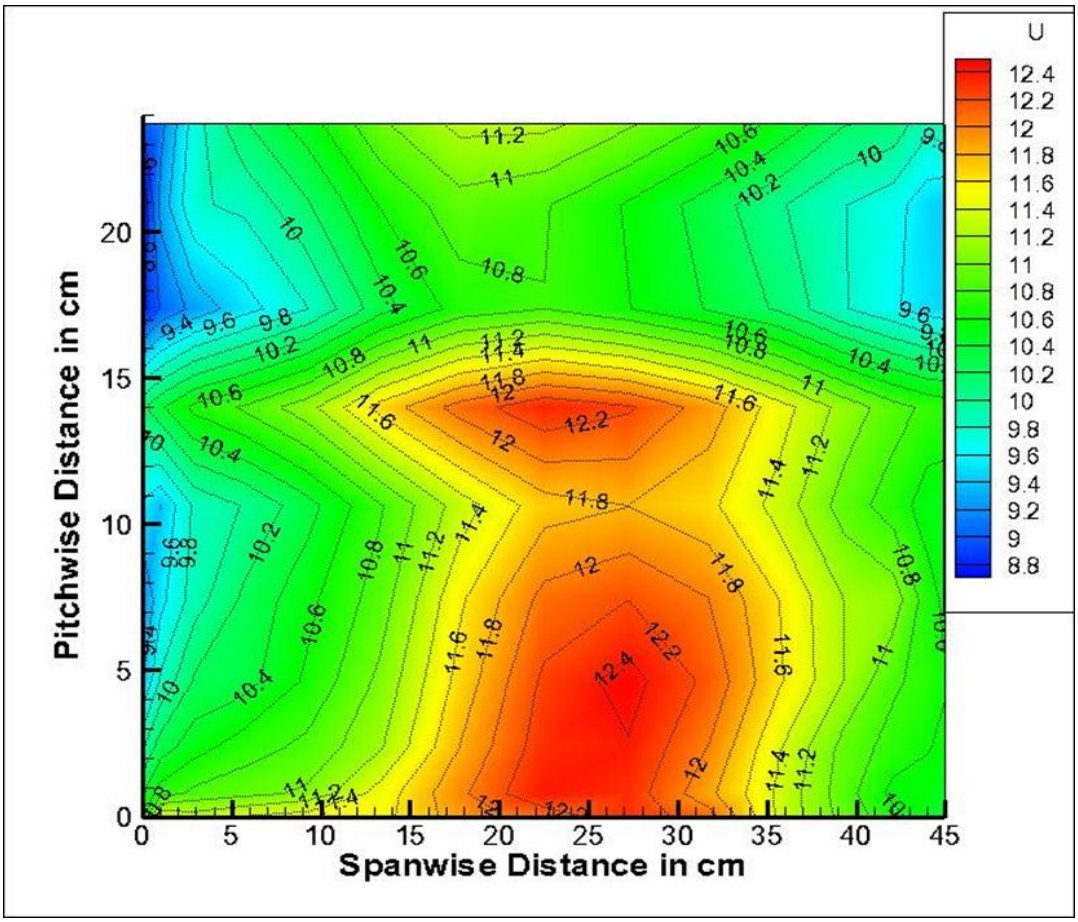

Figure 5.2.1 Inlet Plane Velocity Distribution

It can be seen that the velocity field is fairly uniform with a mean velocity of 11 m/sec. Based on this mean velocity the Reynolds number (based on true chord length) is found to be ~ 430,000. Nearer to the walls the velocity tends to reduce which is due to large scale eddies that extend their influence deep into the flow. Some low velocity regions are

observed near the corners as well. However most of the low momentum fluid is removed from the test section through the bleed slots so as to avoid any secondary flow effects due this region of slow moving fluid.

5.3 Inlet Plane Turbulence Field

The inlet plane turbulence field was computed from the velocity measurements in the form of a root mean square velocity distribution (which indicates the turbulence level) and a distribution of turbulence intensity (root mean square velocity measured as a percentage). For each data point sampled at 5 kHz for 60 seconds, the fluctuation in velocity was computed as follows,

$$u_i^{'} = u_{mean} - u_i \qquad (5.4)$$

Where, $u^{'}$ = velocity fluctuation in m/sec.

u_{mean}= mean velocity of all the samples at that particular point on the inlet plane

u= velocity of a particular data point contained in the sample

Now the root mean square velocity also called turbulence level can be computed as ,

$$U_{rms} = \sqrt{\frac{\sum_{i=1}^{N} u_i^{'2}}{N}} \qquad (5.5)$$

Where N is the number of data points in the sample.

The turbulence intensity is calculated as

$$TI = \frac{U_{rms}}{U_{mean}} \times 100 \qquad (5.6)$$

Figure 5.3.1 shows the root mean square velocity over the inlet plane and Figure 5.3.2 shows the turbulence intensity distribution over the inlet plane.

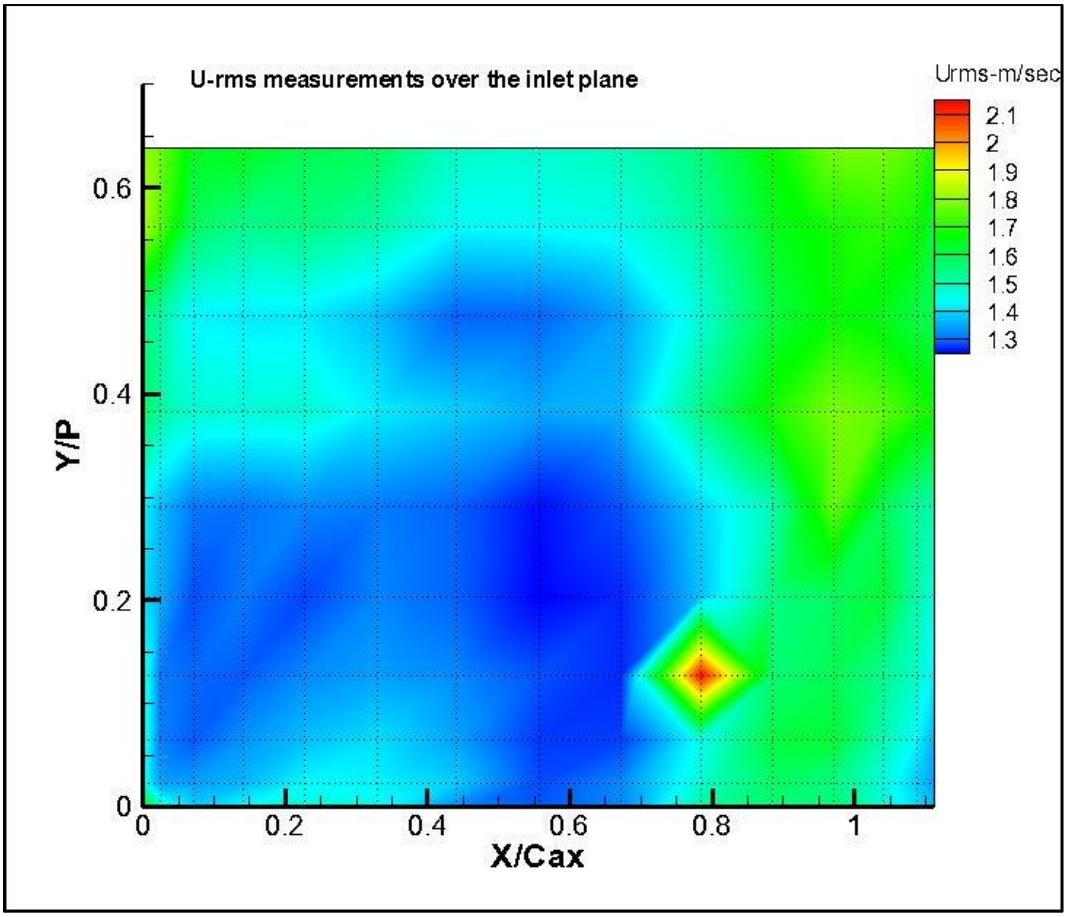

Figure 5.3.1 Root Mean Square Velocity Distribution over the Inlet Plane

It can be seen that the fluctuation levels are fairly uniform in the central core region. They tend to increase nearer to the walls, which could possibly be the effect of large turbulent eddies.

There can be seen a spot of unusually high fluctuation at about X/C_{ax}=0.8 and Y/P=0.1. It is believed that this is a single point measurement error and does not have any physical significance; hence can be ignored. The distribution obtained is similar to one obtained by Erickson [24] on the same test facility and hence validates the approach flow.

Figure 5.3.2 shows the inlet plane turbulence intensity distribution. It can be seen that the turbulence intensity is distributed in a uniform manner over the inlet plane with a mean intensity of about 13 % Such a distribution is typical of the flow coming out of a well-mixed combustor. The effect of vortices around the corners is evident in the higher turbulence intensities.

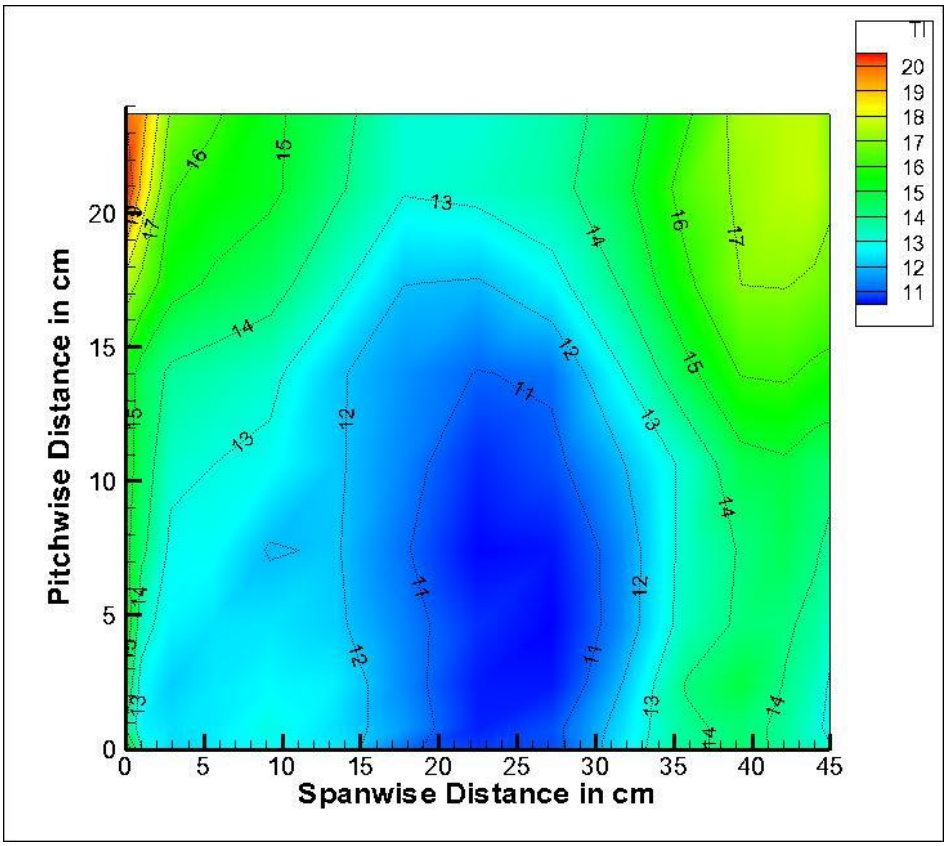

Figure 5.3.2 Inlet Plane Turbulence Intensity Distribution

5.4 Turbulence Spectrum

The turbulence spectrum is calculated to compute various scales of turbulence. At a point in the inlet plane a total of 15 velocity waveforms are captured at 5 kHz for 60 seconds. These time-domain data is transformed into a frequency domain using a fast Fourier transform scheme as described in chapter 5.

Figure 5.4.1 shows the energy density spectrum. It shows the energy/Hz contained at various fluctuation frequencies.

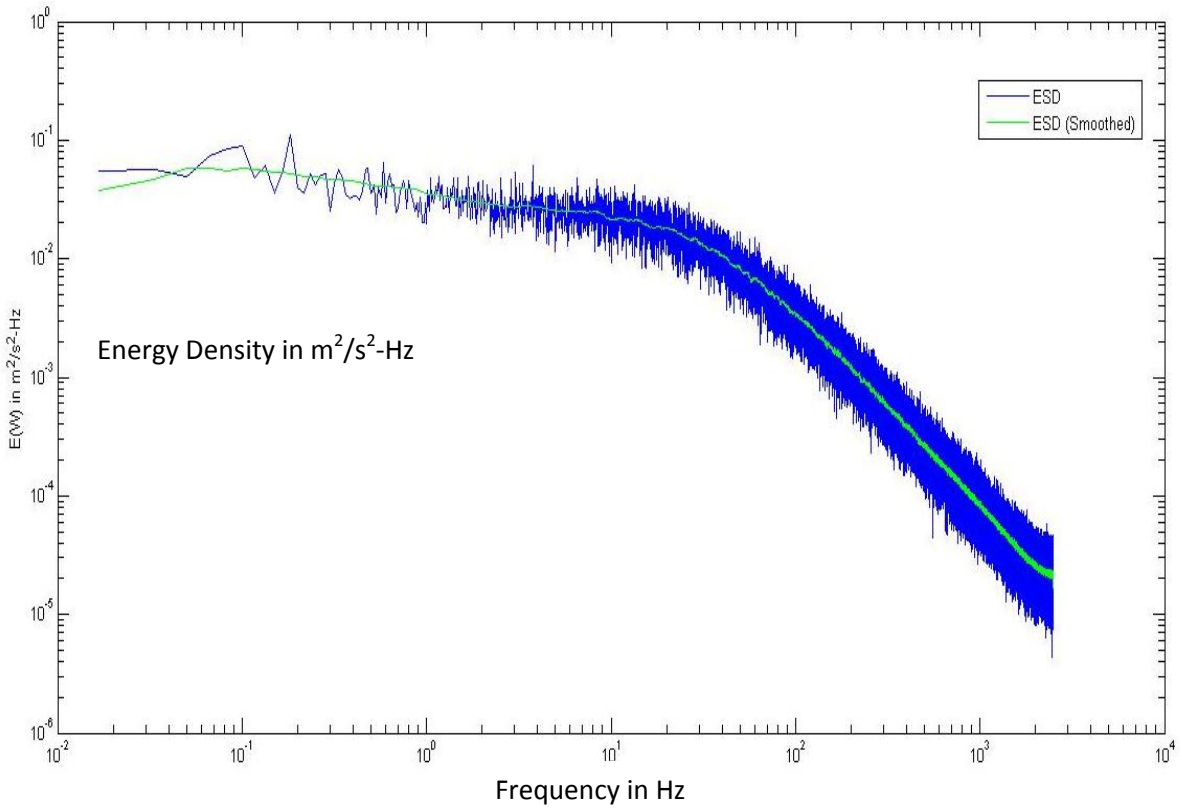

Figure 5.4.1 Energy Density Spectrum for Approach Flow

The energy density spectrum was used to calculate various turbulent scales as explained below.

Integral length scale

This is a measure of the length scales of the largest eddies present in the flow. It is calculated using the following expression:

$$\Lambda = \frac{U_{avg} E(\omega)_1}{4u_{rms}^{\ 2}} \qquad (5.7)$$

where the subscript 1 represents the first frequency band.

Turbulence dissipation rate

It is the rate at which the kinetic energy is transferred from the large eddies to the smaller eddies. It is calculated as :

$$\varepsilon = 16.2 \frac{E(\omega)_{(smooth,25000)}^{3/2} \omega_{25000}^{3/2}}{U_{avg}} \qquad (5.7)$$

Where "smooth" refers to the power spectral density curve after smoothing and the 25000 refers to the 25000th frequency point which is around 400 Hz and is on the -5/3 sloped line in the inertial subrange of the spectrum.

Energy length scale

This gives the size of the average energy containing eddy. It is calculated as:

$$Lu = 1.5 \frac{u_{rms}^{3}}{\varepsilon} \qquad (5.8)$$

Taylor micro scale

This is the size of the smallest eddy that can exist before viscous dissipation. It can be calculated as:

$$\lambda = \sqrt{\frac{15 \nu u_{rms}^2}{\varepsilon}} \qquad (5.9)$$

Table 5.4.1 gives the values of various scales of turbulence in the approach flow to the flow passages.

Table 5.4.1 Scales of Turbulence in the Approach Flow

Name	Value	Normalized value (Over true chord length of 0.5579 m)
Integral Length Scale	0.109 m	0.195
Turbulence Dissipation Rate	38.3 m^2/s^3	-
Energy Length Scale	0.066 m	0.119
Taylor Micro scale	0.0029 m	0.0052

5.5 Approach Flow Temperature Distribution

The approach flow temperature distribution is measured and verified that it is representative of a typical combustor. The temperature profile is generated by varying the power input to a series of heaters located in the passage upstream of the inlet plane. Several iterative steps are needed to achieve a distribution that is engine representative.

The approach flow temperature distribution is obtained as a dimensionless recovery temperature given by:

$$\theta = 1 - \frac{T_{X,Y,Z} - T_{mid}}{T_W - T_{mid}} \qquad (5.10)$$

Where,

$T_{X,Y,Z}$ is local temperature at a particular location in the spanwise direction; it is measured by a thermocouple that is traversed in the spanwise direction. T_{mid} is the temperature of

the flow at a mid-span location, given by a thermocouple located at that location. T_w is the temperature of the endwall upstream of the leakage slot which is given by a thermocouple located on the lip of the endwall simulation a stator endwall.

It should be noted that in the present experiment the near wall flow is heated and the passage flow is cold. This is the reverse of a situation in a real engine. However the quantities are measured in non-dimensional form, this adjustment would indicate trends similar to that of a real engine.

Figure 5.5.1 shows the approach flow temperature profile thus generated.

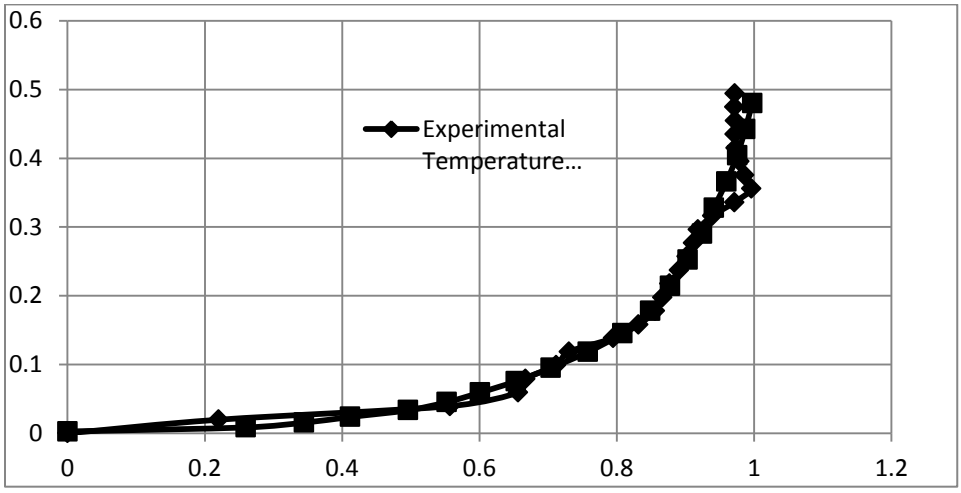

Figure 5.5.1 Approach Flow Temperature Profile Used in the Experiment in Comparison to Engine Representative Temperature Profile (Labeled as 'Solar CFD Data')

Chapter 6

Experimental Procedure

This chapter discusses the experimental procedure followed to measure the essential parameters of the study namely the endwall adiabatic effectiveness values and the non-dimensional passage temperature fields. A brief overview of the concept of adiabatic effectiveness and non-dimensional passage temperature fields is provided and the procedure for measuring those is described in detail.

6.1.1 Adiabatic wall temperature and film cooling effectiveness

It was essential for this study to measure the film cooling effectiveness of the coolant in the leakage flow and in the combustor exit approach flow over the contoured endwall at different conditions. When a secondary coolant fluid is passed over a heated surface, it acts as a heat sink. The heat flux from the wall can be then represented as:

$$q_w = h*(T_w - T_{aw}) \qquad (6.1)$$

Where T_{aw} is the adiabatic wall temperature; it is the surface temperature at which there is no heat transfer. If the wall itself is of low conductivity, as is the case with the present study, the wall temperature is equal to the adiabatic wall temperature. This leads to a zero near wall temperature gradient i.e.

$$\left.\frac{\partial T}{\partial y}\right|_{y=0} = 0. \qquad (6.2)$$

The effectiveness of the leakage flow to cool the adiabatic endwall is measured in terms of a non-dimensional quantity called adiabatic effectiveness. Goldstein, 1971, [35] described adiabatic effectiveness as:

$$\eta = \frac{T_{x,y,z=0} - T_\infty}{T_l - T_\infty} \qquad (6.3)$$

This quantity represents the ratio of the difference between the adiabatic wall temperature and the mainstream flow temperature to the difference between the temperatures of the leakage flow and the mainstream flow. Under the best case scenario, all the leakage flow would form a protective film over the wall and the wall would assume the temperature of the leakage flow, leading to an adiabatic effectiveness of 1. However, the complex fluid mechanics of the flow conditions within the passage lead to mixing between the leakage flow and the mainstream flow, causing a variation in adiabatic effectiveness values over different locations. In the present study, adiabatic effectiveness values were measured at different locations and their variation was related to the fluid mechanics within the rotor passage.

6.1.2 Procedure

The wind tunnel was started and was allowed to run for a period of 2 hours in order to achieve steady state. The leakage flow is heated by means of resistance heaters to about $8\text{-}10^0$ C above the mainstream flow. The mean leakage flow temperature is measured by 4 thermocouples located in the rim-seal gap. The mainstream flow temperature is measured by a thermocouple located at a mid-span, mid-pitch location slightly upstream of the leakage slot. The approach flow temperature profile is established using the scheme described in chapter 5 .Since the study is done in the presence of a combustor exit temperature profile; it is ensured that the leakage flow temperature and the wall temperature upstream of the leakage slot are equal.

A total of 111 points were identified on the contoured endwall, starting from the stagnation point $X/C_{ax}=0$ to the trailing edge $X/C_{ax}=0.98$, as shown in figure 6.1.2. At each point wall temperature was measured using a E type thermocouple mounted on a 3-axis traverse and inserted into the flow field through the moveable panel, described in chapter 3. The adiabatic wall condition was verified by taking 9 temperature measurements in wall normal direction upto a distance of 5 mm away from the wall and verifying that no temperature gradients exist near the wall. The non-dimensional recovery temperature, θ, for five randomly selected points is shown in figure 6.1.1 and it can be seen that there is no temperature gradient near the wall verifying that adiabatic wall

conditions are achieved. Each of the temperatures was sampled for 20 seconds at 1 Hz using the software MEDAQ (developed by Erickson [24]). This procedure was repeated at each of the leakage Mass Flow Ratios of 0.5 %, 1.0 % and 1.5 %.. Since the procedure measures adiabatic effectiveness in terms of temperature differences, the uncertainty associated with the method is small and is about 1-1.3 %. Most of the uncertainty is due to the variation in the temperature of the room from which the tunnel draws in the air.

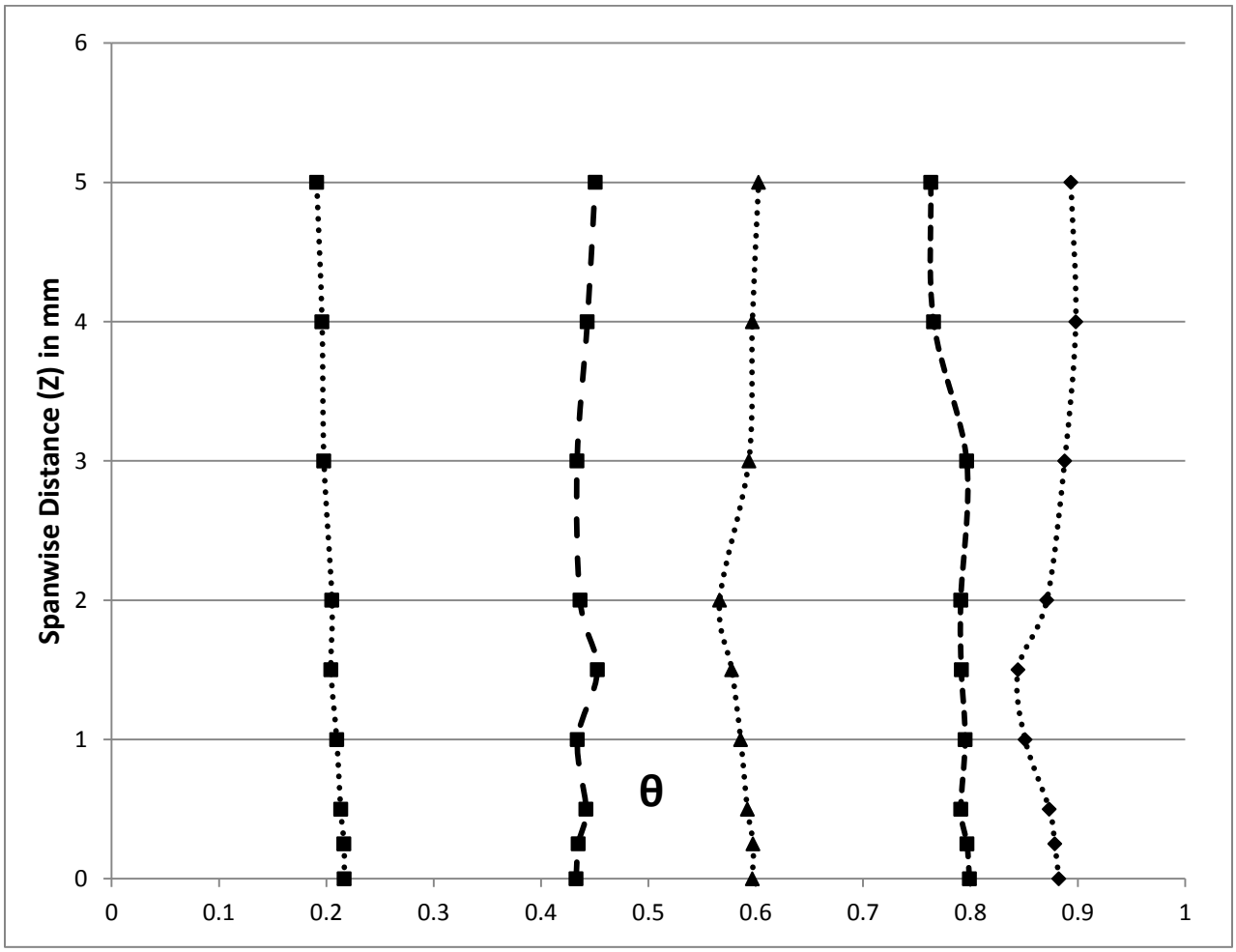

Figure 6.1.1: Randomly Selected Endwall Normal Non-Dimensional Temperature Profiles to Verify Adiabatic Wall Conditions

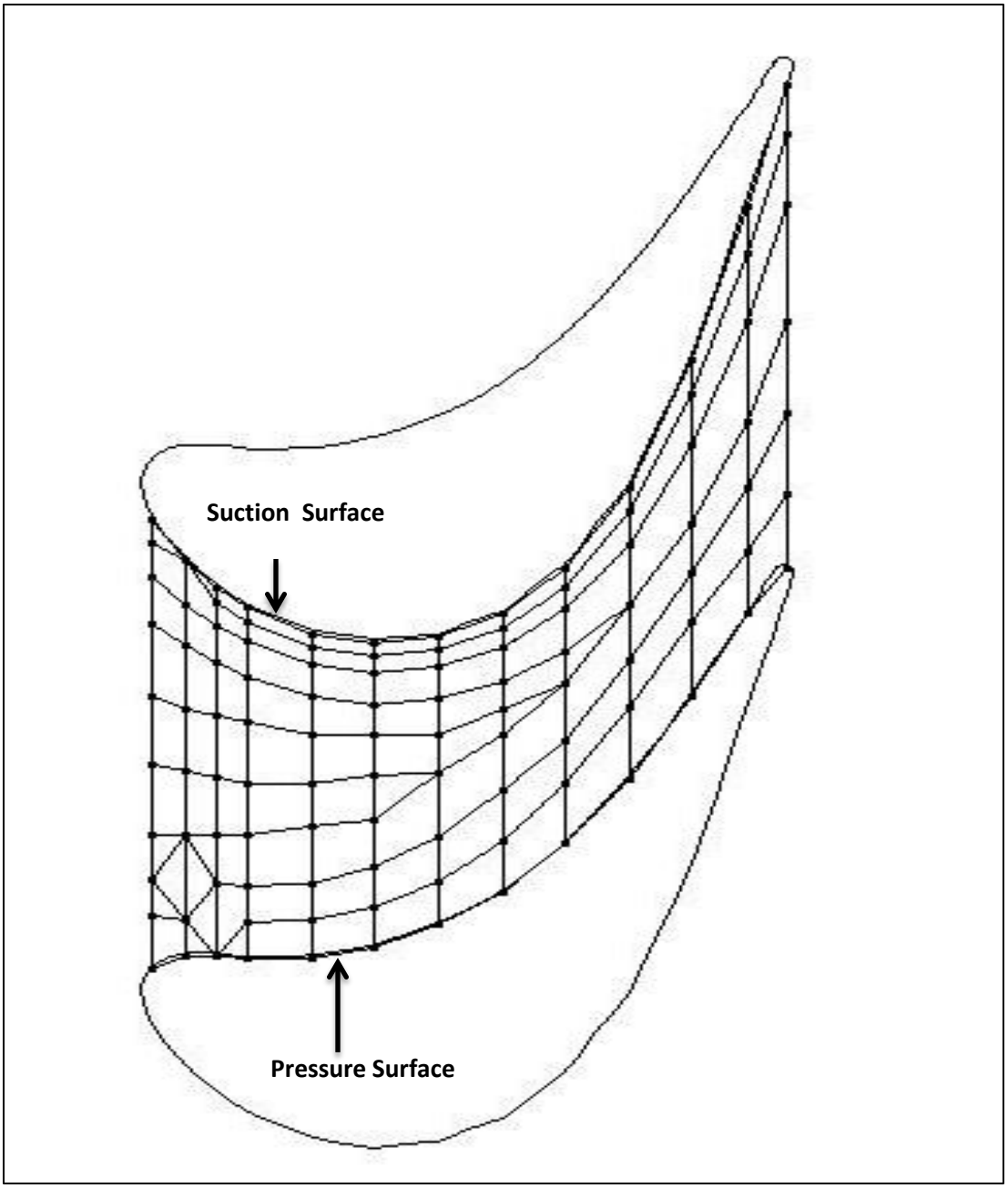

Figure 6.1.2 Measurement Locations on the Endwall (Measurements are made on the intersections of the gridlines)

6.2.1 Passage Temperature Field Measurements

In order to explain the variation in adiabatic effectiveness values at different locations of the passage, it is important to understand the mixing of the leakage flow with the approach flow. This mixing is studied by taking passage temperature field measurements. As mentioned in chapter 3, for the present study, the leakage and near wall approach flow is heated and the mainstream flow is cool. Hence, thermal signatures can provide a means to identify where the 'heated' near wall flow has migrated within the passage, making passage temperature field measurements important. The passage temperature fields are measured and plotted as a non-dimensional recovery temperature given as ,

$$\theta = \frac{T_{x,y,z} - T_{\infty}}{T_l - T_{\infty}}. \qquad (6.4)$$

Here, $T_{x,y,z}$ is the temperature at any spanwise location. Regions of higher recovery temperature will indicate the presence of heated near wall flow and regions of lower values will indicate the presence of cooler mainstream flow.

6.2.2 Procedure

Four rows of points stretching from the suction to the pressure surface were identified within the passage located at X/C_{ax}=0.0, 0.25,0.45 and 0,92. At each of these points, temperatures were measured starting at the wall and then progressively moving out in the spanwise direction . Each of the temperatures was samples at 1 Hz for 20 seconds. This procedure was repeated for the different leakage flow rates of 0.5 %, 1.0 % and 1.5 % MFR

Shown in figure 6.2.1 are the passage temperature measurement points.

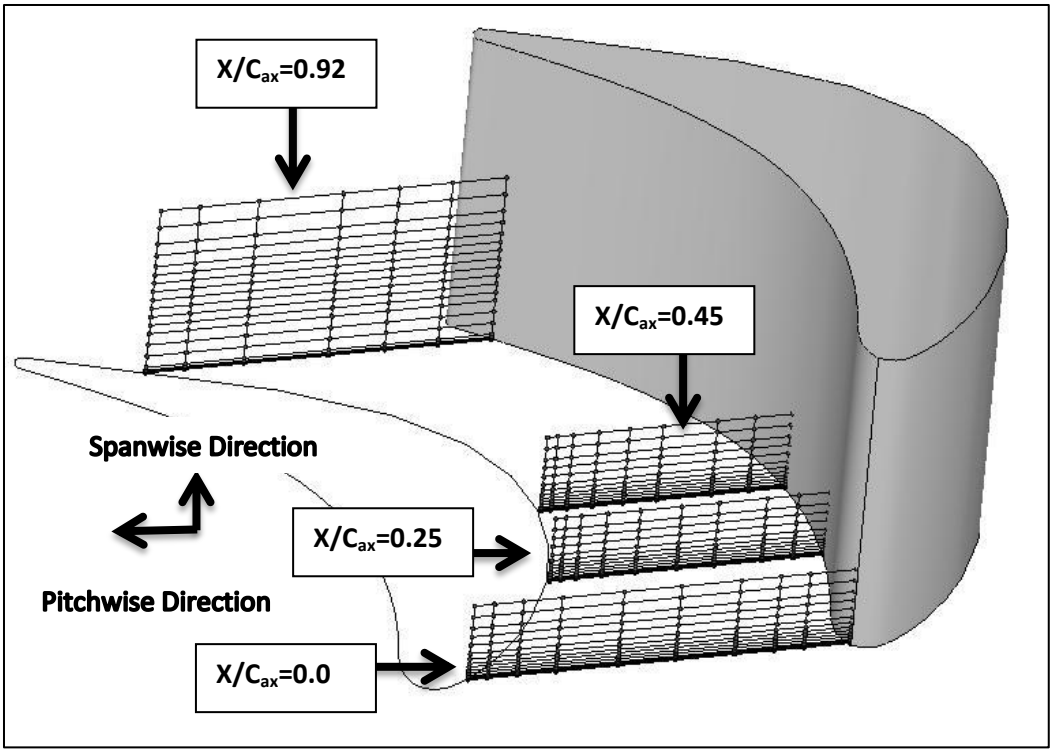

Figure 6.2.1 Passage Temperature Measurement Planes

Chapter 7

Experimental Results and Discussion

This chapter discusses in detail the experimental results obtained from the study. First the passage thermal fields are discussed to obtain a broad understanding of the migration of the coolant (both in the leakage flow and in the approach flow) within the passage. Next the adiabatic effectiveness contours for the endwall profile used in the present study i.e. for the shark nose endwall are discussed. In order to obtain an understanding of how a contouring scheme would affect the near wall coolant flow, the results from the shark nose endwall are compared to the results obtained from another profile called the dolphin nose endwall. The investigation on the dolphin nose profile was done by researcher Yuhyen Seah as part of the same project sponsored by Solar Turbines Inc. The data were obtained by personal communication with the researcher. Next, the effect of the additional coolant in the approach flow due to an engine representative combustor exit temperature profile is studied using 'augmentation' contours. Augmentation is simply the increase in adiabatic effectiveness by using an engine representative combustor exit temperature profile relative to other temperature profiles. Two separate sets of augmentation contours for the shark nose endwall are made using the principle of linear superposition- the first which shows the augmentation in adiabatic effectiveness in using an engine representative combustor exit temperature profile against a flat temperature profile (no coolant in the approach flow), documented by Erickson[24] and the second which shows augmentation in adiabatic effectiveness values in using the engine representative profile against a profile that had coolant only up to 10% of the span as documented by Erickson [24]. The second set of augmentation contours in particular give an idea about the intensity of mixing at different regions of the passage. Finally a case with the leakage flow having the same temperature as that of the mainstream flow, and the approach flow having the usual profile with coolant present near the wall, i.e. a case with coolant in only the approach flow is discussed. This case, although not being

realistic, will be used to confirm the hypotheses developed about leakage flow migration, as it will be easy to 'track' the leakage flow due to its different thermal signature.

7.1 Passage Temperature Fields

As discussed in chapter 7, non-dimensional recovery temperature distribution was measured along planes located at four streamwise locations within the passage i.e. at X/C_{ax}=0,0.25,0.44 and 0.92. These temperature fields give an indication of the migration of the near wall coolant in the spanwise direction. Figure 7.1.1 shows the passage temperature distributions for a leakage mass flow ratio of 1.5%. The first plane at the beginning of the passage is at a streamwise location of X/C_{ax}=0, the second plane is at a streamwise location of X/C_{ax}=0.25, the third plane is at a location of X/C_{ax}=0.45 and the fourth plane is at X/C_{ax}=0.92.

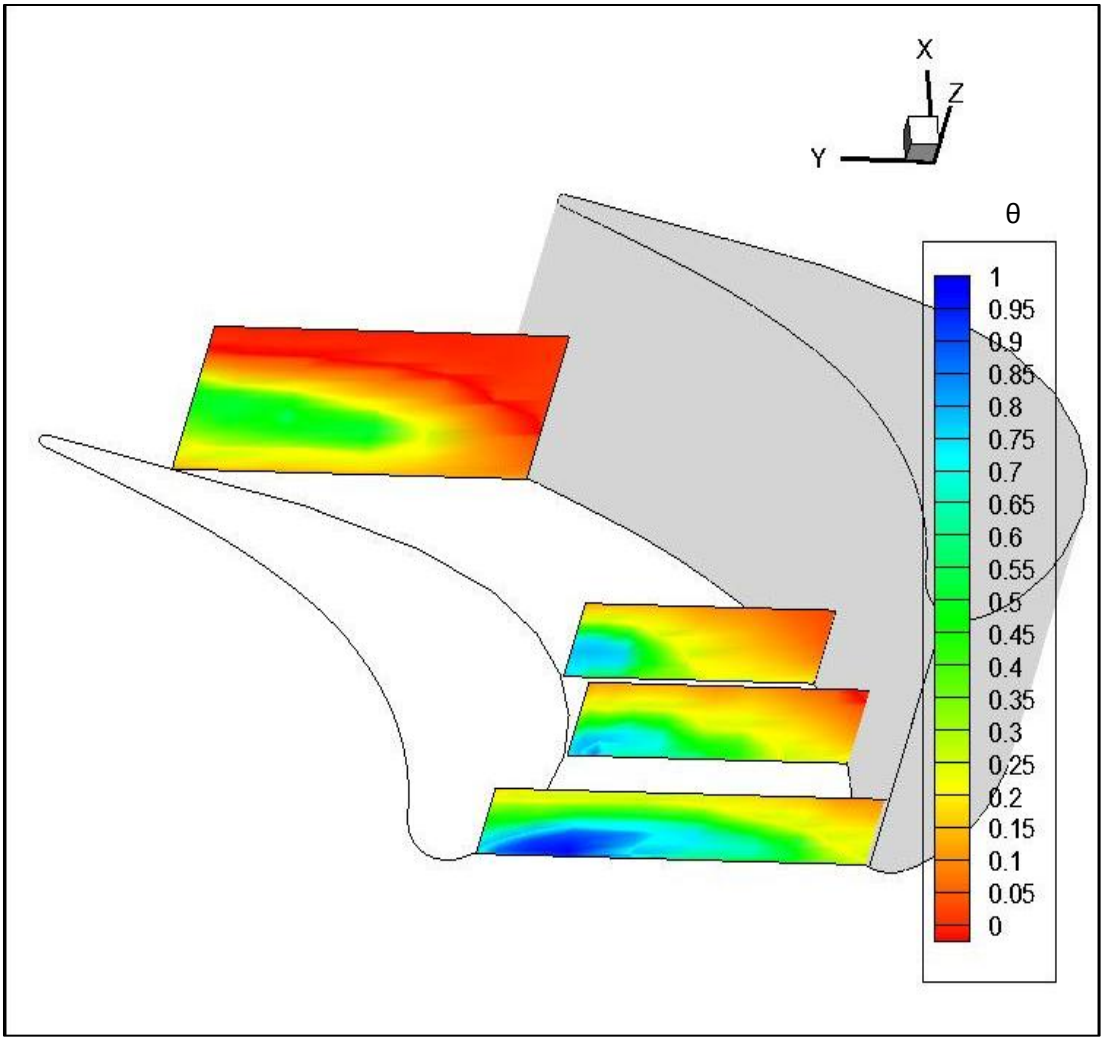

Figure 7.1.1 Passage Temperature Fields for 1.5 % Leakage MFR

It can be seen that most of the coolant is being pushed towards the suction side by the pressure-to-suction pressure gradient. This trend seems to be consistent all over the passage. However, at the beginning of the passage i.e. at $X/C_{ax}=0$, it can be seen that there is some coolant penetrating toward the pressure side. This 'penetration' of the coolant towards the pressure side progressively decreases as one moves towards the exit of the passage. It is believed that at the beginning of the passage, it is the leakage flow which helps the near wall coolant to counter the pressure-to-suction pressure gradient, leading to the presence to coolant near the pressure side. As one moves further downstream into the passage the leakage flow loses its energy, hence an increasing

amount of coolant is pushed toward the suction side, depriving the pressure side. It can also be seen that the 'coolest' region of a particular plane gradually moves up in the spanwise direction as one moves from the beginning toward the end of the passage. This is directly related to the development of the passage vortex. Thus the passage vortex carries with itself the coolant flow, and lifts it completely off the endwall toward the exit of the passage. One can see some amount of coolant, although low, staying near the endwall near the trailing edge. This is believed to be the coolant in the approach flow that still provides some cooling effect to the endwall near the trailing edge.

Figure 7.1.2 shows the passage temperature distributions for the case with a leakage mass flow ratio of 1.0 %.

The overall migration of the coolant (both in the approach flow as well as in the leakage flow) follows similar trends as that of the 1.5 % leakage MFR case. However, when on the plane at $X/C_{ax}=0$ (first plane at the beginning of the passage) it can be seen that the 1.0 % leakage MFR case shows somewhat less amount of coolant near the pressure side as compared to the 1.5 % MFR case. The higher leakage flow rate in the 1.5 % MFR case might be more effective in countering the pressure-to-suction pressure gradient and keeping relatively more coolant near the pressure surface than the 1.0% MFR case.

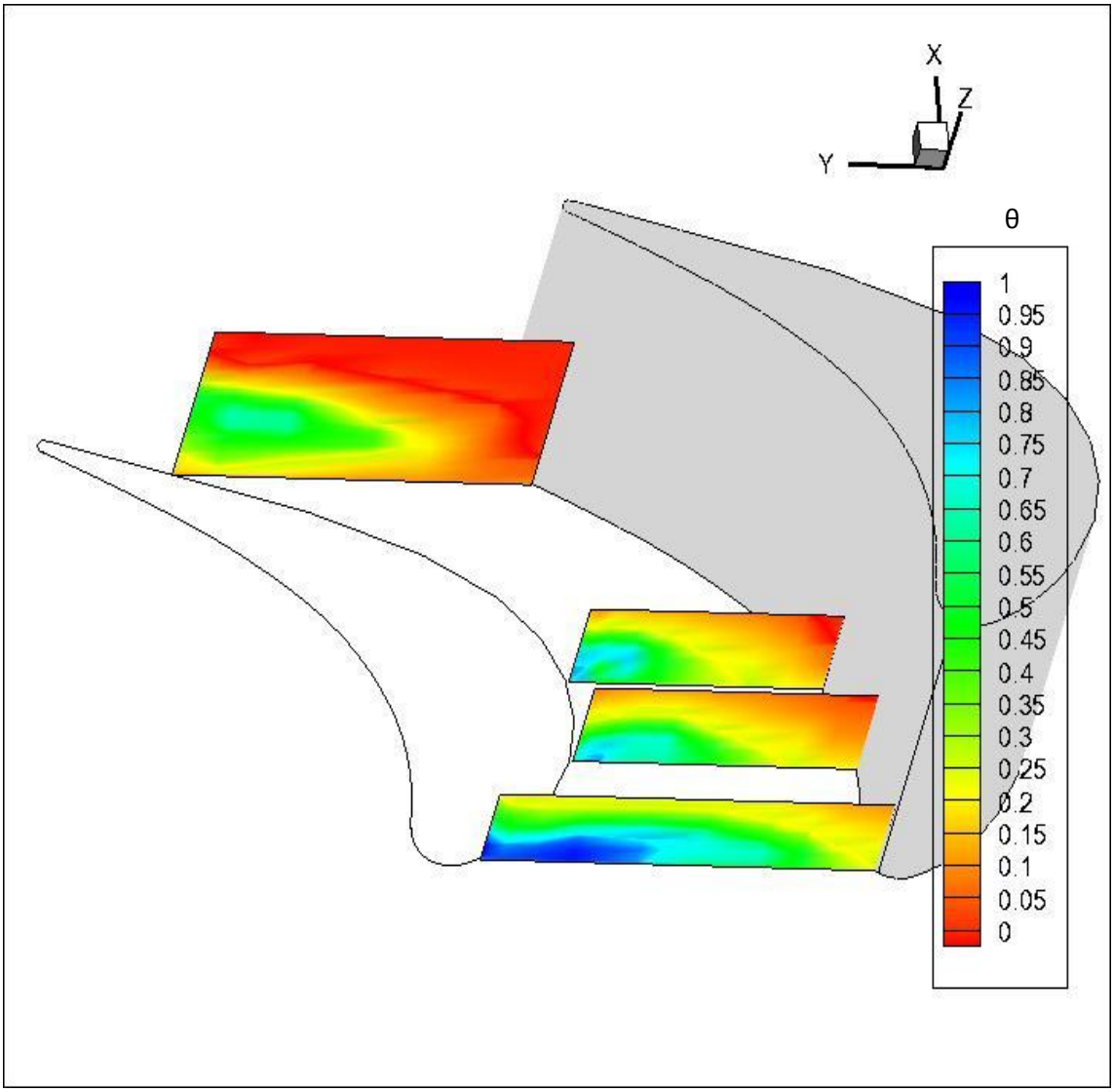

Figure 7.1.2 Passage Temperature Fields for 1.0 % Leakage MFR

Figure 7.1.3 shows the temperature field distributions for 0.5 % leakage mass flow ratio case. It can be seen that in case of the 0.5% MFR case the amount of coolant near the suction side of the plane at $X/C_{ax}=0$ has significantly decreased in comparison to the 1.0% and 1.5% leakage MFR cases..

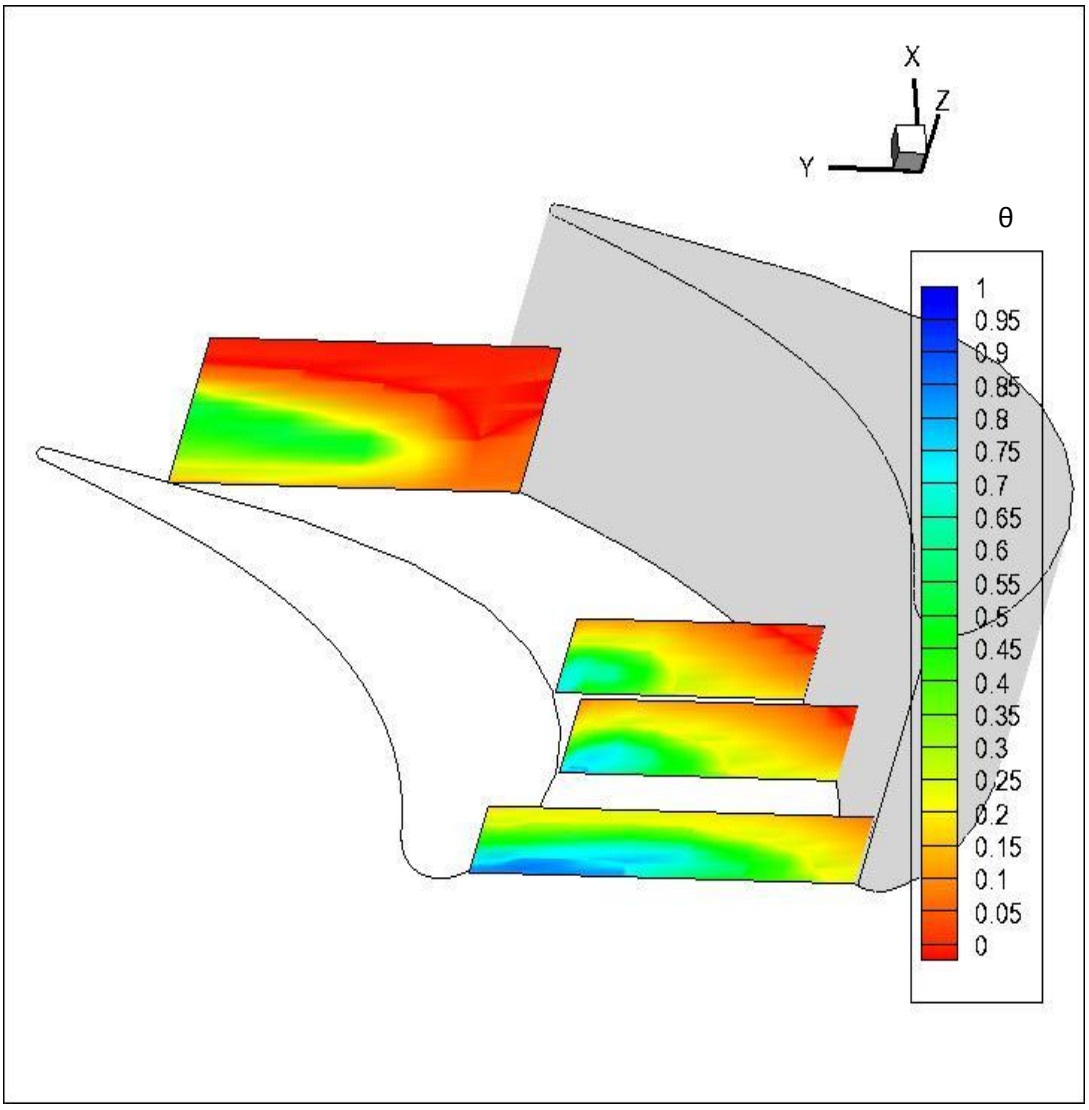

Figure 7.1.3 Passage Temperature Fields for 0.5 % Leakage MFR

Also as the leakage flow rate is weaker, there is less opposition of the near wall coolant to the pressure-to-suction pressure gradient, thereby decreasing the amount of coolant near the pressure side as compared to cases with higher leakage flow rates

7.2 Endwall Adiabatic Effectiveness Contours

Since the endwall material is of low conductivity, the heat transfer within the wall i.e. the case of the wall acting as a heat sink is low and hence can be treated as an adiabatic wall. Temperature measurements were taken across the 110 points on the endwall at varying leakage mass flow ratios (MFR) of 0.5% ,1.0% and 1.5%. Adiabatic wall condition was verified by taking near wall temperature measurements up to a distance of 5 mm away from the wall and verifying that there was no temperature gradient close to the wall as discussed in chapter 6.The wall temperatures were used to obtain the endwall adiabatic effectiveness values at the respective locations given as:

$$\eta = \frac{T_{X,Y,Z=0} - T_{mid.}}{T_{leakage} - T_{mid}} \qquad (7.1)$$

These adiabatic effectiveness values were plotted in the form of contour plots using software called TECPLOT 360. The software interpolates the adiabatic effectiveness values were between any two points to obtain the contour plots. Figure 7.2.1 shows the adiabatic effectiveness contours for the Shark nose endwall for a leakage mass flow ratio (MFR) of 1.5 % under engine representative approach flow temperature profile.

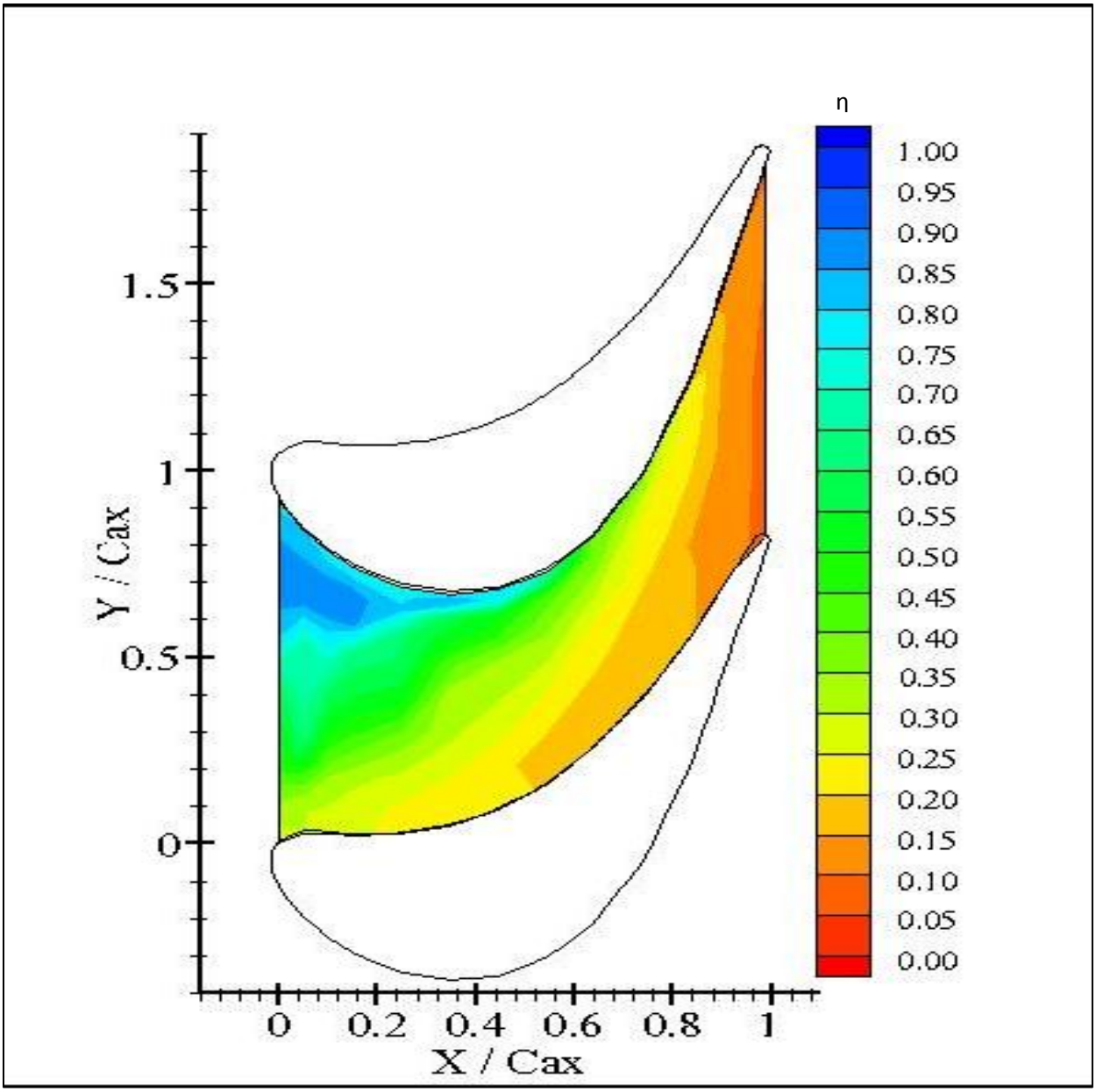

Figure 7.2.1 Endwall Adiabatic Effectiveness Contours for Shark Nose Endwall at 1.5 % Leakage MFR

It can be observed from figure 7.2.1 that the adiabatic effectiveness values are higher towards the beginning of the passage and progressively go on decreasing moving further into the passage, indicating mixing of the coolant (both in the approach flow and the leakage flow) with the mainstream flow. Also, at any streamwise location, the values

increase as one moves from the pressure side toward the suction side. This is because the cross stream pressure gradient between the pressure side and the suction side pushes the near wall coolant toward the suction side, resulting in higher adiabatic effectiveness values toward the suction side. Increasing values of effectiveness in the center pitch region but somewhat toward the pressure side can be seen at the beginning of the passage indicating a strong 'competition' between the coolant being accelerated in the streamwise direction by the contoured endwall and the pressure-to-suction pressure gradient that pushed the coolant toward the suction side. Also shown is a tiny strip of lower adiabatic effectiveness values adjacent to the suction side, indicating the effect of the suction side leg of the horseshoe vortex which tends to lift the coolant off the endwall mixing it with the mainstream flow. There seems to be some cooling value, although low, indicated by the adiabatic effectiveness value of ~ 0.15 near the trailing edge. This may be due to coolant in the approach flow, having been washed from the outer reaches of the coolant thermal layer, down the pressure surface and across the endwall. If so, this process continues throughout the entire passage. The effectiveness values in this region were measured to be negligible in studies with no combustor cooling flow (Erickson [24]), suggesting that the combustor coolant in the engine-representative case approach flow is useful toward providing thermal protection to the endwall, even near the trailing edge.

Figure 7.2.2 shows the adiabatic effectiveness contours on the Shark nose endwall at leakage mass flow ratio (MFR) of 1.0% under an engine representative approach flow temperature profile.

The trends in adiabatic effectiveness values over the passage for the case of 1.0% MFR are similar to those for the case of 1.5 % MFR. Towards the downstream half of the passage, the values are almost identical for the two cases, indicating that by this location the coolant from the leakage flow has lost its effectiveness and the combustor coolant in the approach flow is responsible for endwall protection. However, subtle differences are noticed near the beginning of the passage between the 1.5 % MFR and 1.0 % MFR cases. It can be seen that the migration of coolant fluid toward the pressure side, as observed in

case of the 1.5% MFR case in the beginning of the passage, is missing in the 1.0 % MFR case. This indicates that as the flow rate of the leakage flow is decreased, there is less energized coolant flow to counter the cross-stream pressure gradient. It is also expected that the leakage flow rate will exit the slot in a pitchwise more uniform manner when the leakage flow rate is higher. The net effect is relatively higher adiabatic effectiveness values toward the pressure surface in the 1.5 % leakage MFR case than in the 1.0 % leakage MFR case. Also visible is that the region of lower adiabatic effectiveness values adjacent to the suction side has increased in area with a lowering of the leakage mass flow rate, indicating that the high leakage mass flow rate leads to a weaker effect of the suction side leg of the horseshoe vortex; that is, with higher leakage flows rates, the area of influence of the suction side leg of the horse shoe vortex is reduced.

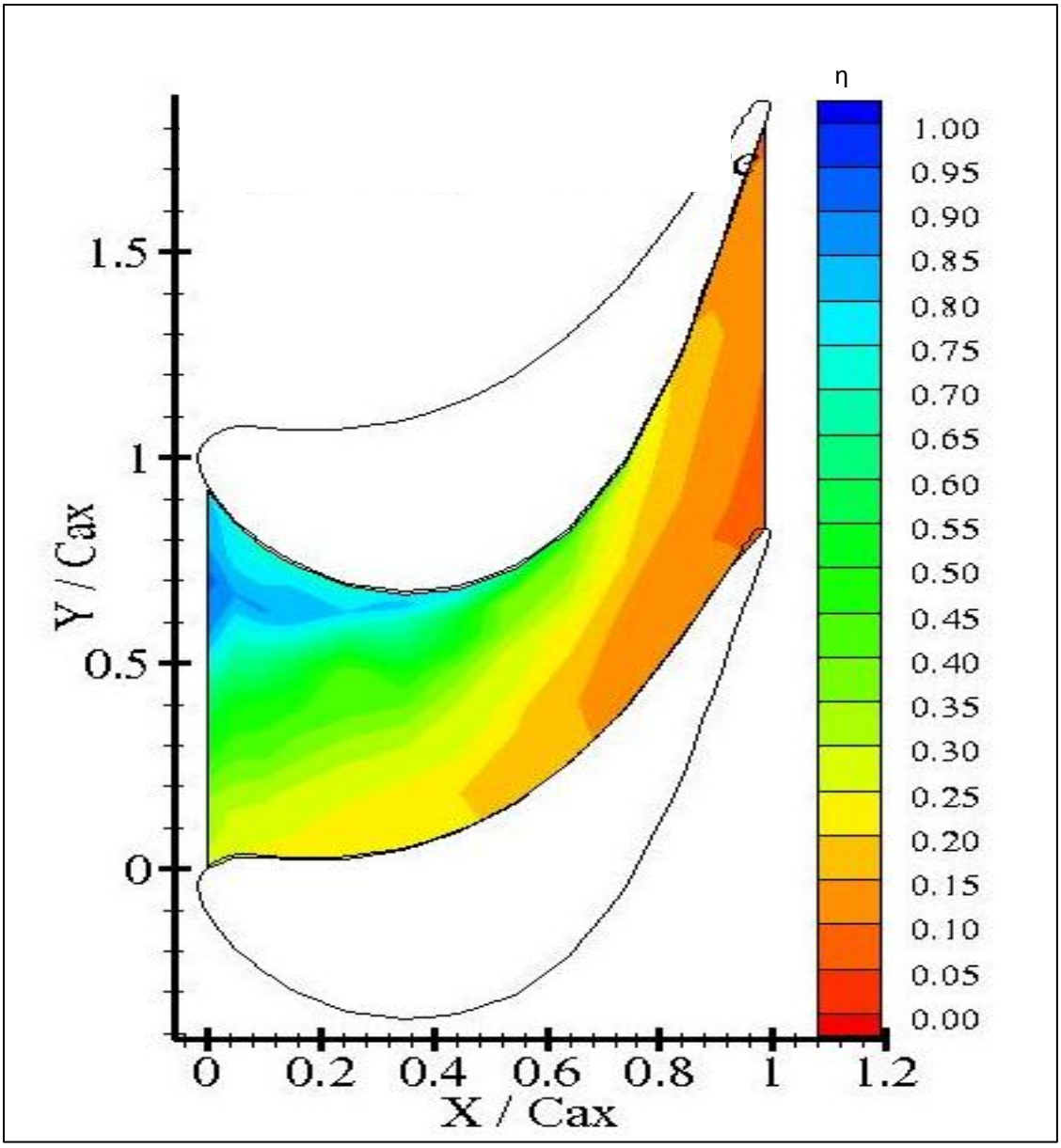

Figure 7.2 2 Endwall Adiabatic Effectiveness Contours for Shark Nose Endwall at 1.0% Leakage MFR

Figure 7.2.3 shows the adiabatic effectiveness contours for the case with leakage mass flow ratio (MFR) of 0.5 %.

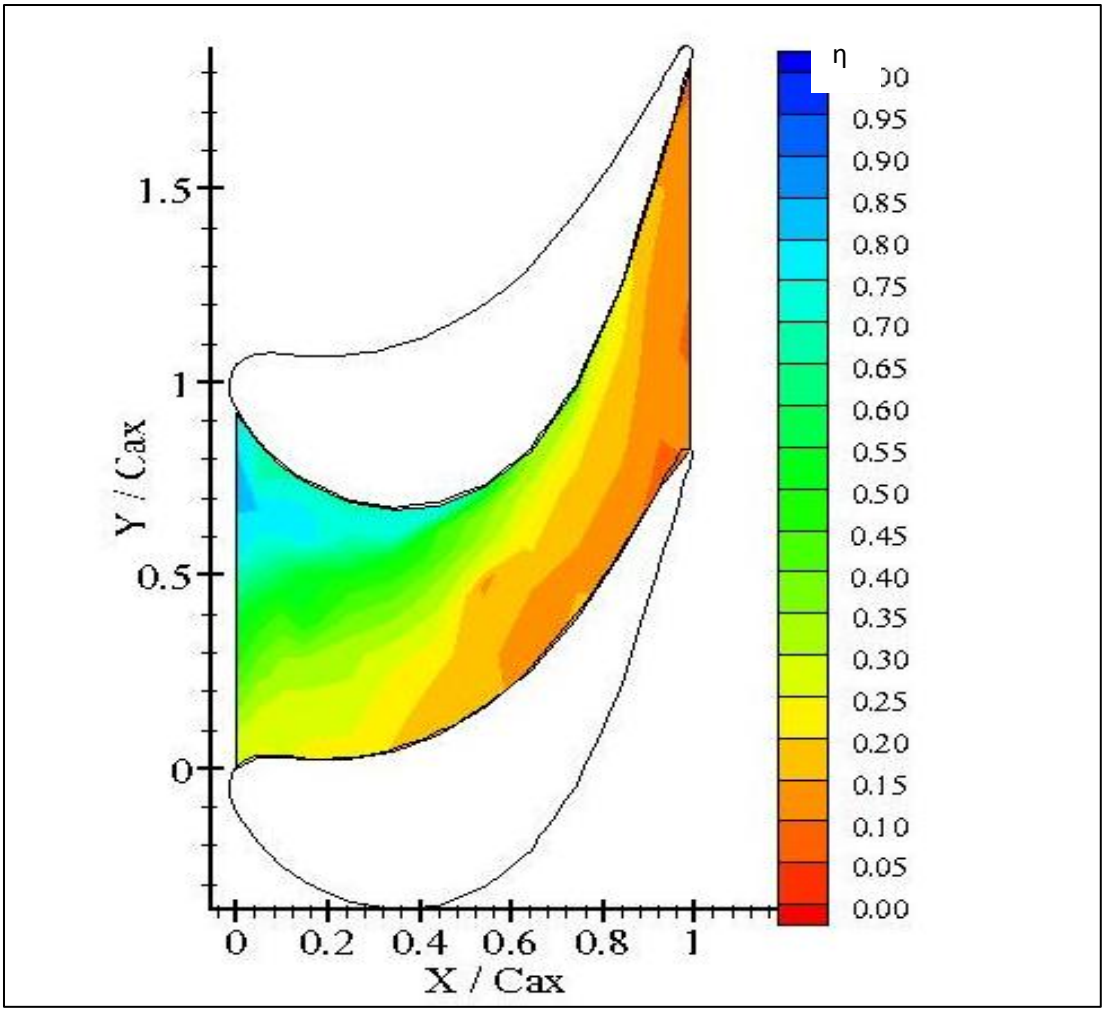

Figure 7.2. 3 Endwall Adiabatic Effectiveness Contours for Shark Nose Endwall at 0.5% Leakage MFR

In the 0.5 % MFR case, values of adiabatic effectiveness are lower on the suction and pressure sides, relative to values for the higher MFR cases. These trends indicate that the leakage flow energizes the near-wall coolant at the beginning of the passage to counter the cross-stream pressure gradient effects in the leakage slot and in the upstream portion of the passage. This effect results in higher adiabatic effectiveness values toward the pressure side with increasing leakage flow rates. Toward the downstream regions of the passage, quite expectedly, the adiabatic effectiveness values for the 0.5 % leakage MFR case are nearly identical to values for the 1.0% and 1.5% MFR cases, supporting the

hypothesis that in this region, only the combustor coolant in the approach flow contributes to the downstream region's endwall cooling.

7.3 Comparison of Shark Nose and Dolphin Nose Endwall Profiles

The adiabatic effectiveness contours indicated that the streamwise acceleration of the near wall coolant by the contoured endwall affects the flow distribution in the passage. In order to have a detailed understanding of how a particular contouring scheme would affect the near wall coolant flow, adiabatic effectiveness values obtained from the shark nose profile in the present study are compared to those obtained with a different endwall called the dolphin nose. The data for the dolphin nose endwall were collected by Yuhyen Seah, a researcher at Heat Transfer Laboratory, Mechanical Engineering, University of Minnesota, as part of the same project sponsored by Solar Turbines Inc. Line plots showing adiabatic effectiveness values from suction side to pressure side are made at four streamwise locations: X/C_{ax}=0.0,0.25,0.45 and 0.92. Also plotted at these locations are the adiabatic effectiveness values with different leakage mass flow ratios (MFRs) to indicate the influence of the leakage flow on the adiabatic effectiveness values for each of the two contouring schemes.

Figure 7.3.1 shows the difference in shark and dolphin nose contours. It can be seen that the shark nose contour has a gradual gradient starting at X/C_{ax}= -0.21 and ending at X/C_{ax}=0.31. The dolphin nose contour on the other hand has a steep gradient starting at X/C_{ax}= -0.14 and ending at X/C_{ax}= 0.06. Thus, the dolphin nose contour is expected to provide a rapid acceleration to the near wall flow at the beginning of the passage whereas the shark nose profile is expected to provide a much more gradual but prolonged acceleration to the near wall flow.

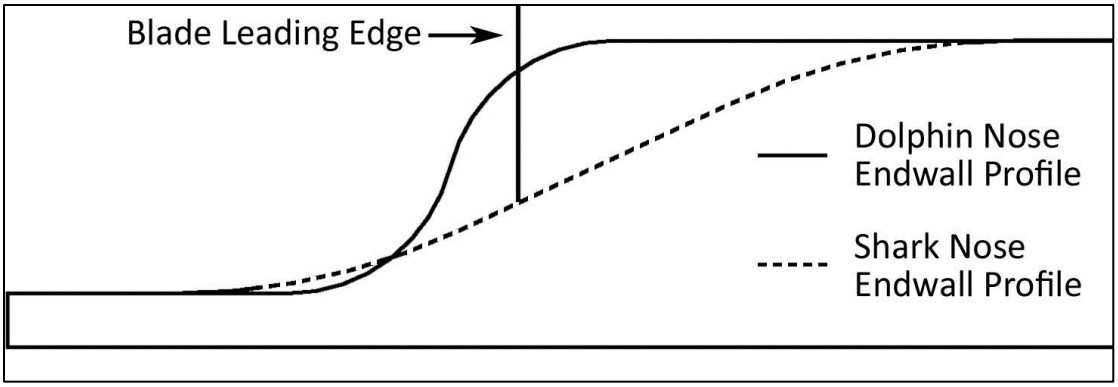

Figure 7.3.1 Shark and Dolphin Nose Contours

Figure 7.3.2 (a) shows the comparison of adiabatic effectiveness values for the Shark and the Dolphin nose endwall profiles for the three leakage mass flow ratios at the streamwise location of $X/C_{ax}=0$. Figure 7.3.2 (b) shows the variation of adiabatic effectiveness for the Shark and Dolphin nose profiles at $X/C_{ax}=0$ with varying leakage flow rates. In each of the plots, the ordinate shows the adiabatic effectiveness values and the abscissa shows Y/C_{ax} , the location in the pitch-wise direction. The left side of the plot is the pressure side and the right side is the suction side.

Close to the pressure surface (left) the adiabatic effectiveness values for 1.0 % and 0.5 % MFR cases are identical for the shark nose and dolphin nose endwalls, and differ only slightly for the 1.5 % case. The behavior is identical for the shark and dolphin nose profiles for 1.0% and 0.5 % MFR cases close to the pressure side, maybe due to the effect of the pressure side leg of the horseshoe vortex; the leakage flow rate is not strong enough to influence the cross-stream pressure gradient. When the leakage flow rate is 1.5 %, it seems to have enough energy, obtained by a combined effect of steep acceleration with the dolphin nose profile and increased flow rate, to influence the horseshoe vortex, increasing adiabatic effectiveness values in the dolphin nose profile case. This is made clear in figure 5, where the dolphin nose profile with 1.5 % MFR stands out from the others. The shark nose profile cases are identical to one another.

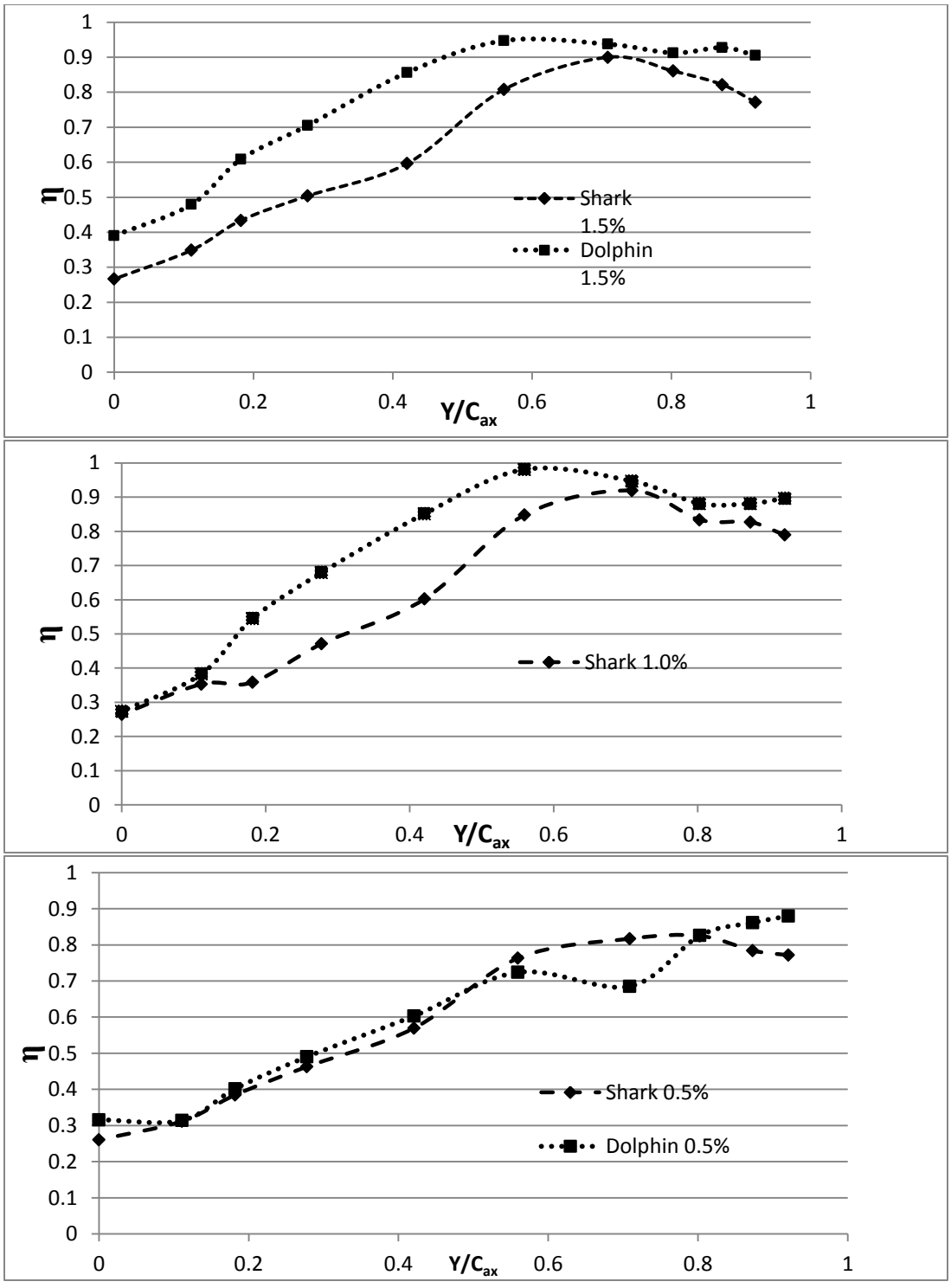

Figure 7.3.2 (a) Comparison of Adiabatic Effectiveness Values for the Shark and Dolphin Nose Profiles using the Engine-representative Combustor Coolant Temperature Profile in the Approach Flow, $X/C_{ax} = 0$

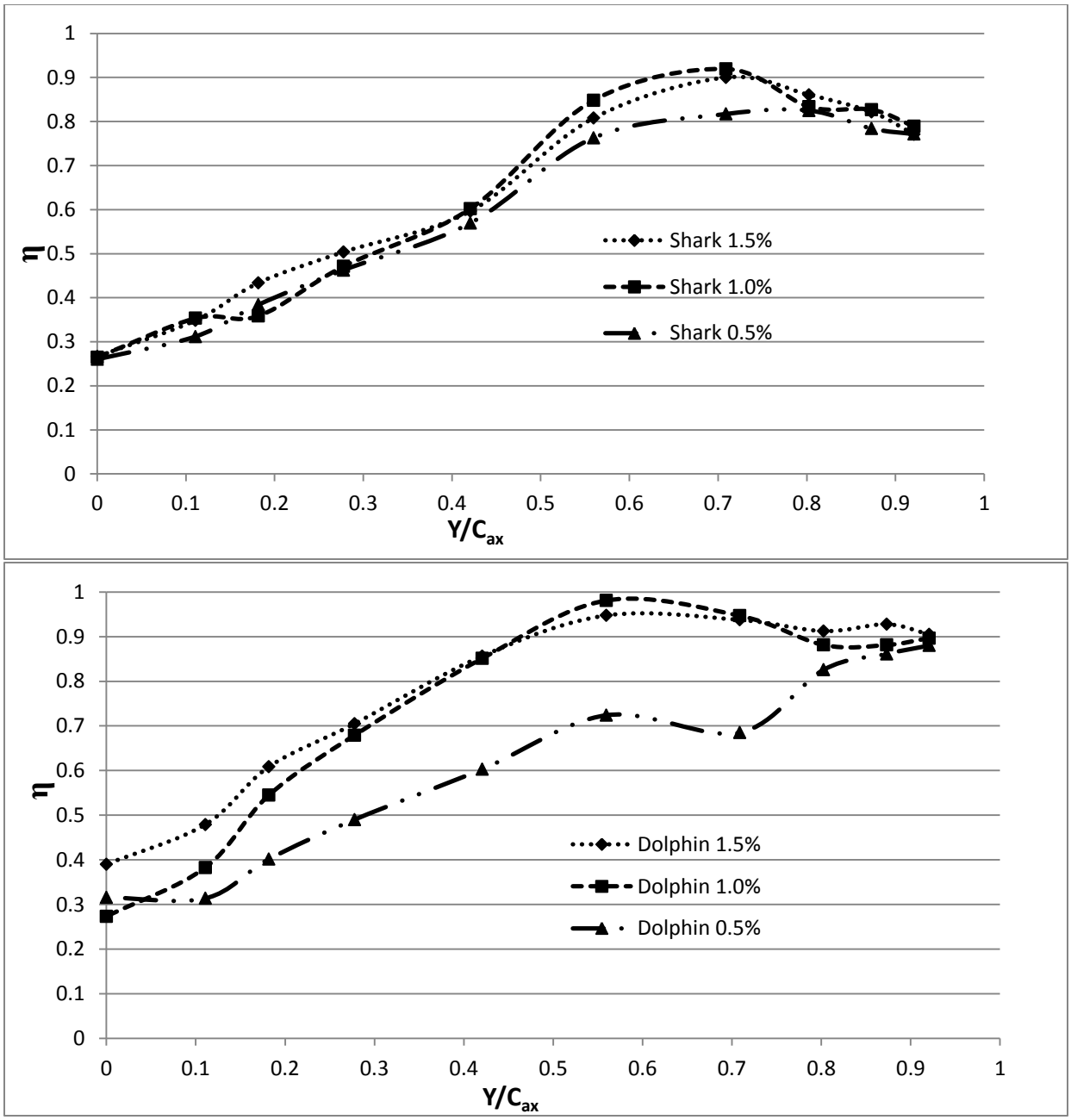

Figure 7.3.2 (b) Comparison of Adiabatic Effectiveness Values for Different MFRs on the Shark or Dolphin Nose Profiles using the Engine-representative Combustor Coolant Temperature Profile in the Approach Flow, $X/C_{ax} = 0$

Moving away from the pressure side toward the suction side,one notes that the dolphin nose profile shows better performance than that of the shark nose profile. This is due to

the more energized near-wall coolant (coming from both the leakage and the approach flow) in the case of the dolphin nose contour due to its steep gradient in the beginning of the passage. However, with 0.5 % MFR, the cases with the two endwall profiles have identical behavior, indicating that the energy of the coolant in the leakage flow is not strong enough to counter the cross-stream pressure gradient and influence the secondary flows. Again, figure 5 shows that for the dolphin nose profile, the 1.5% and 1.0% leakage flow cases stand out from the 0.5% case whereas for the shark nose profile all three cases are almost identical. This indicates that the leakage, if provided with adequate energy (as in the case of the dolphin nose with its steep gradient), actually helps in countering the pressure gradient between the pressure and the suction surface.

Close to the suction side, both the shark nose and the dolphin nose profile cases show a dip in adiabatic effectiveness values due to the effect of the suction side leg of the horseshoe vortex. However, this dip is much more pronounced in the case of the shark nose endwall profile, again indicating that the lower energy of the leakage flow in the case of the shark nose profile is less effective in weakening the suction side leg of the horseshoe vortex than in the case of the dolphin nose endwall.

Figure 7.3.3 (a) shows the comparison of adiabatic effectiveness values for the Shark and the Dolphin nose endwall profiles for the three leakage mass flow ratios at the streamwise location of X/C_{ax}=0.25. Figure 7.3.3 (b) shows the variation of adiabatic effectiveness for the Shark and Dolphin nose profiles at X/C_{ax}=0.25 with varying leakage flow rates.

Close to the pressure side, for the three MFR cases, the shark and the dolphin nose profiles are identical at X/C_{ax}=0.25, indicating that the 1.5 % MFR case, which showed some weakening of the vortices near the pressure side in the upstream portion of the passage, has lost its energy by this streamwise location. Also, nearer the suction side, the differences between the shark and the dolphin nose profile cases have decreased, indicating that the near-wall fluid has lost some of its initial energy given by the dolphin nose (there is no streamwise gradient for the dolphin nose at this point). In the case of the shark nose, the near-wall flow is accelerating due to continuation of the surface slope.

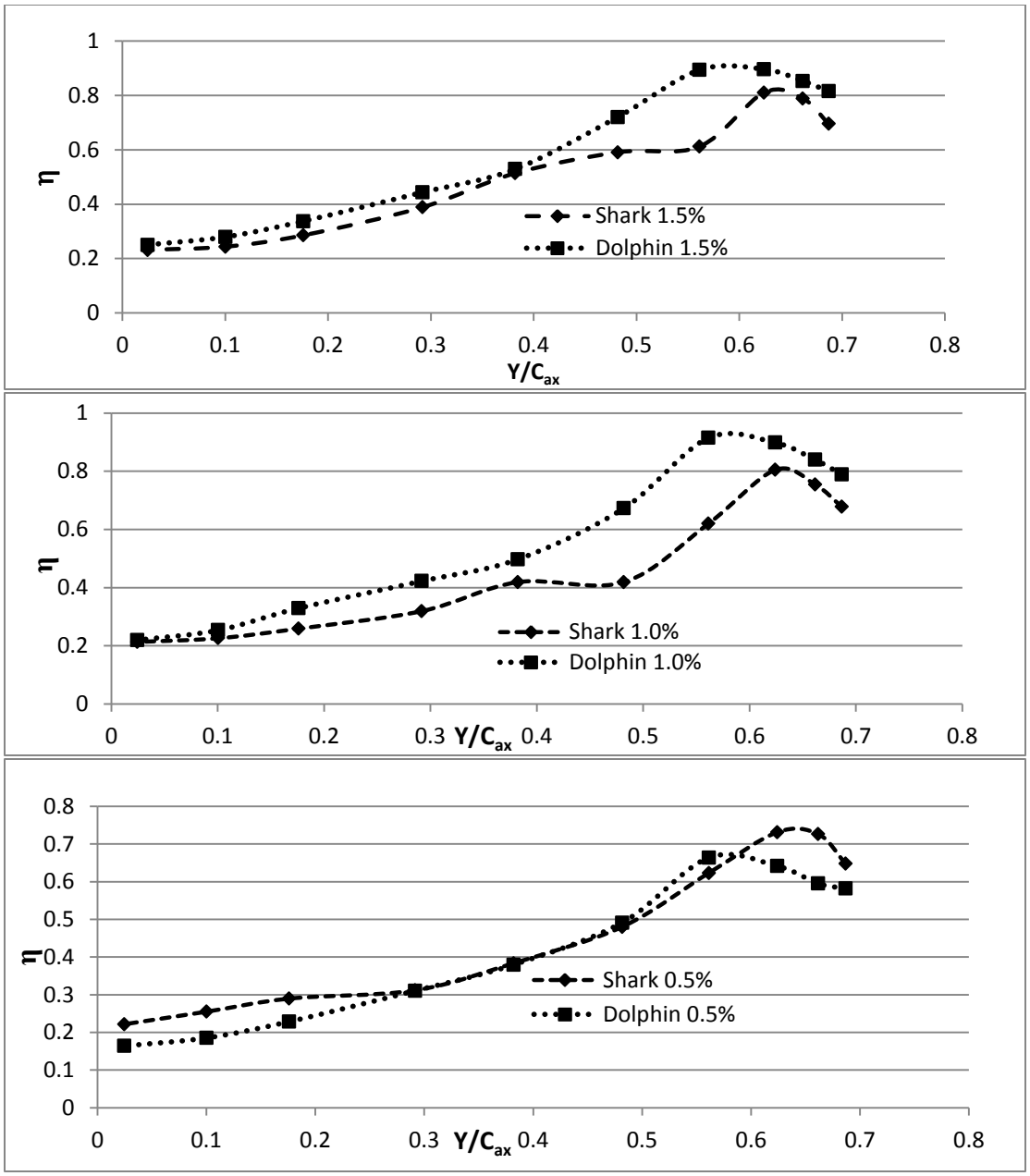

Figure 7.3.3 (a) Comparison of Adiabatic Effectiveness Values for the Shark and Dolphin Nose Profiles using the Engine-representative Combustor Coolant Temperature Profile in the Approach Flow, X/C_{ax}=0.25

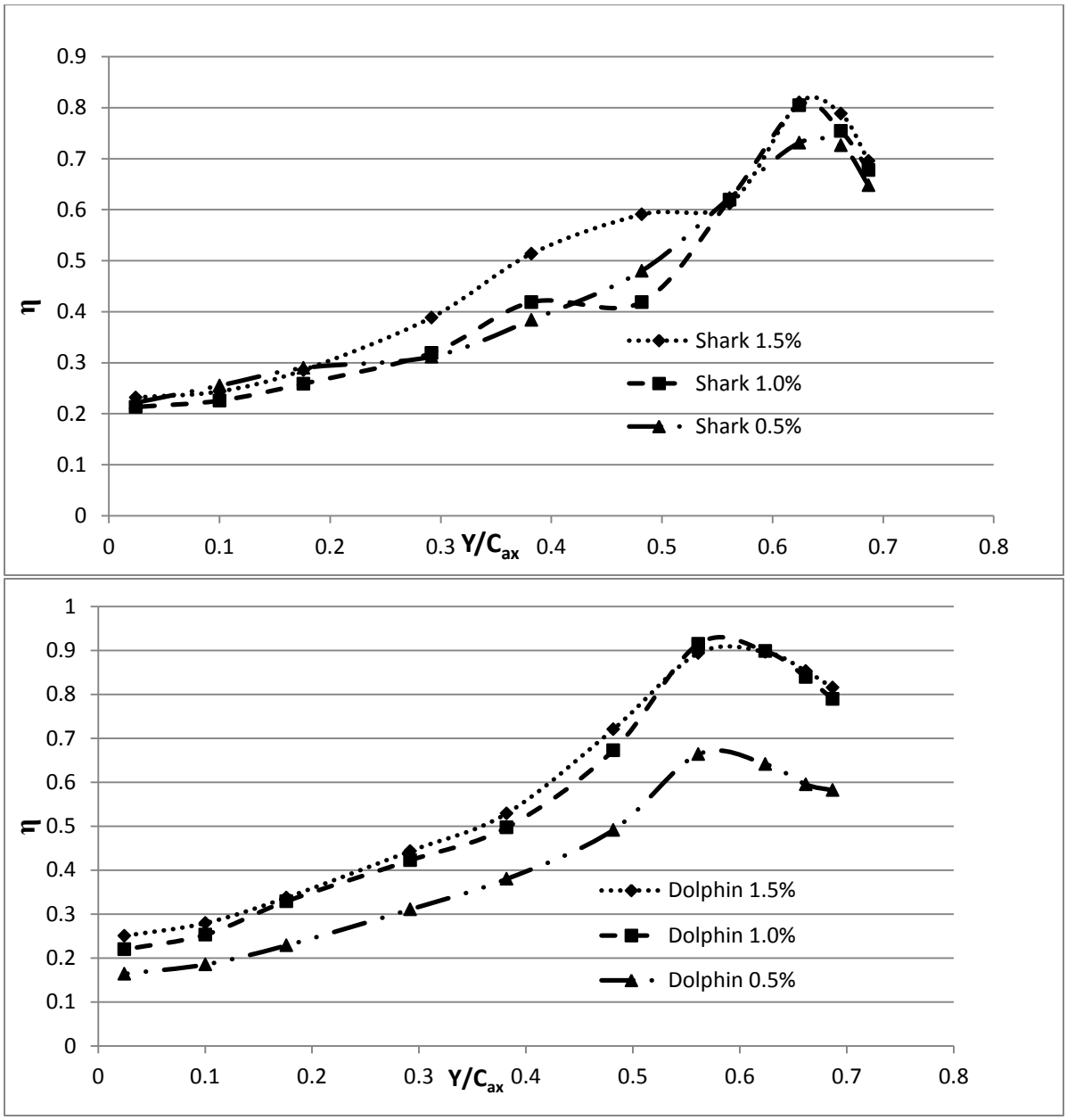

Fig. 7.3.3 (b) Comparison of Adiabatic Effectiveness Values for different MFRs on the Shark or Dolphin Nose Profiles using the Engine-representative Combustor Coolant Temperature Profile in the Approach Flow, X/C_{ax}=0.25

Both profiles show similar steep dips near the suction side, again indicating that the "history" of strong acceleration of leakage flow, which had countered this steep dip in the upstream portions of the passage for the dolphin nose profile, is fading by this streamwise location.

Figure 7.3.4 (a) shows the comparison of adiabatic effectiveness values for the Shark and the Dolphin nose endwall profiles for the three leakage mass flow ratios at the streamwise location of X/C_{ax}=0.45. Figure 7.3.4 (b) shows the variation of adiabatic effectiveness for the Shark and Dolphin nose profiles at X/C_{ax}=0.45 with varying leakage flow rates.

It can be seen that both the shark and dolphin nose profiles match at the streamwise location X/C_{ax}=0.45. This indicates that the continued gradient of the shark nose profile has energized the near wall flow so that values match those of the dolphin nose profile. The effects of the initially strong acceleration for the dolphin nose case have faded. Also ,in figure 7.3.4(b), it can be seen that values for all three MFR cases match those for the shark nose, indicating that leakage flow coolant is playing essentially no role in determining adiabatic effectiveness values. For the dolphin nose, values for the 0.5% case are still lower than those for the other cases near the pressure side.

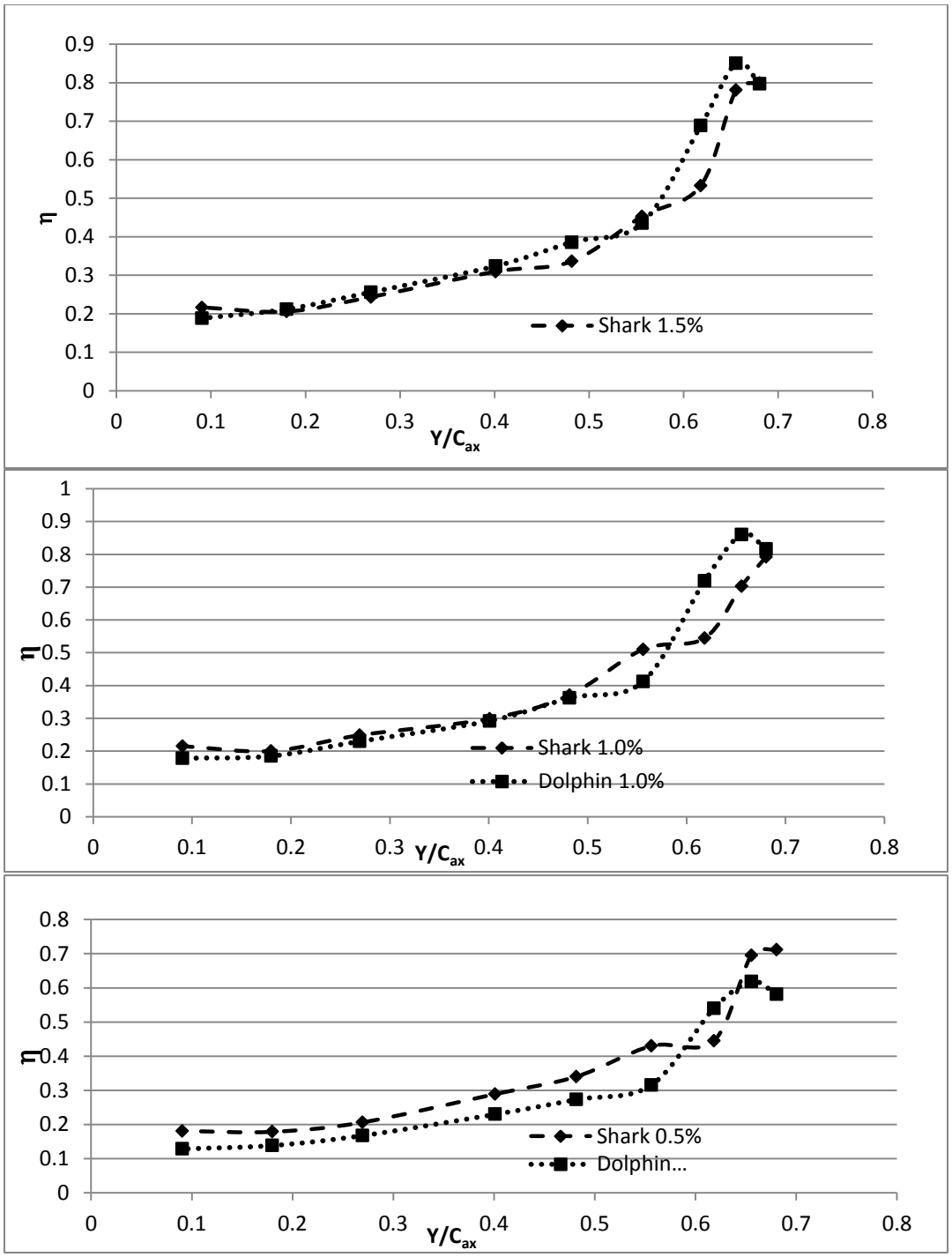

Figure 7.3.4 (a) Comparison of Adiabatic Effectiveness Values for the Shark and Dolphin Nose Profiles using the Engine-representative Combustor Coolant Temperature Profile in the Approach Flow, X/C_{ax}=0.45

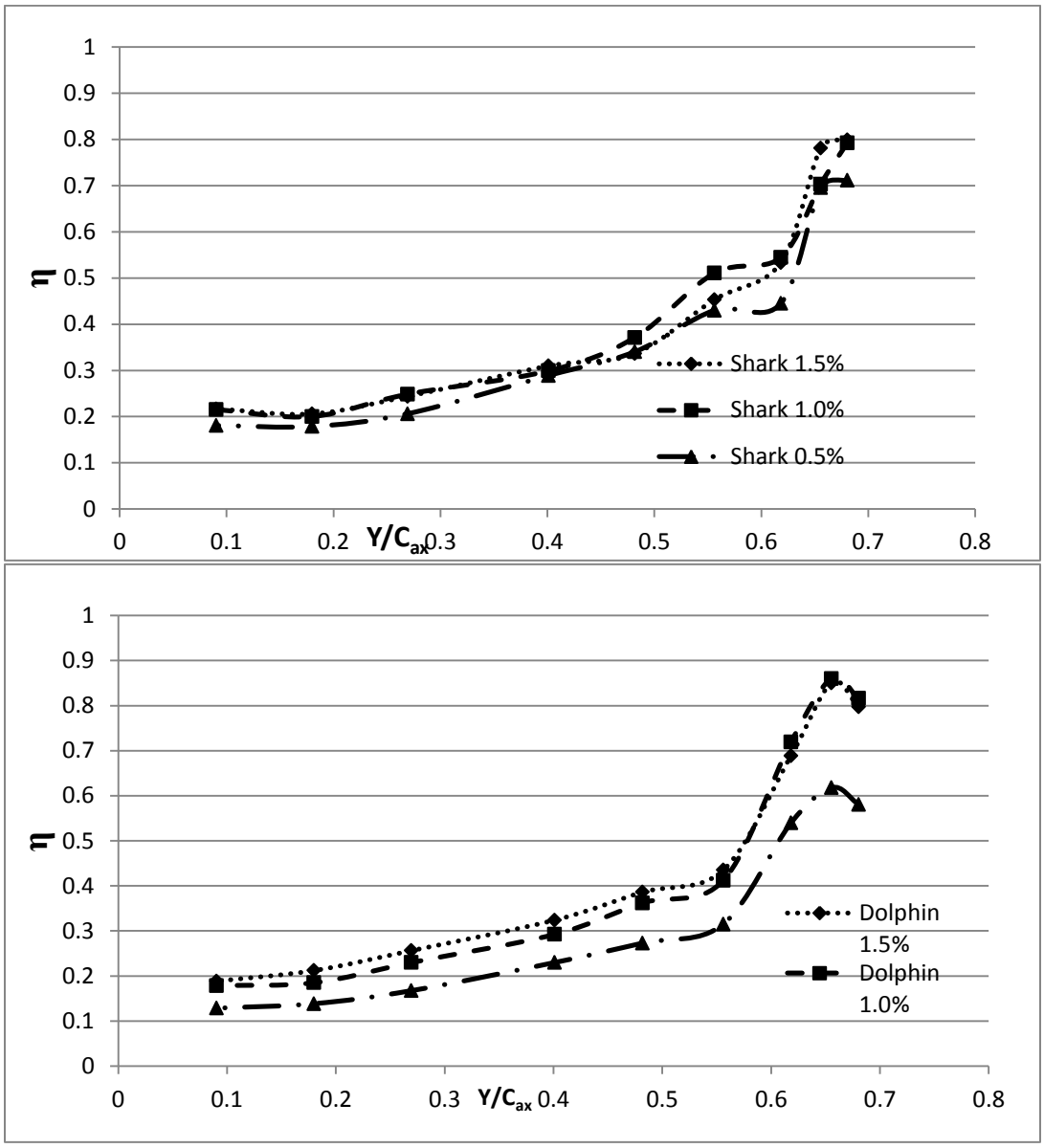

Fig. 7.3.4 (b) Comparison of Adiabatic Effectiveness Values for different MFRs on the Shark or Dolphin Nose Profiles using the Engine-representative Combustor Coolant Temperature Profile in the Approach Flow, X/C_{ax}=0.45

Figure 7.3.5 shows the adiabatic values of all leakage flow rates for both Shark and Dolphin nose endwalls at the location X/C_{ax}=0.92.

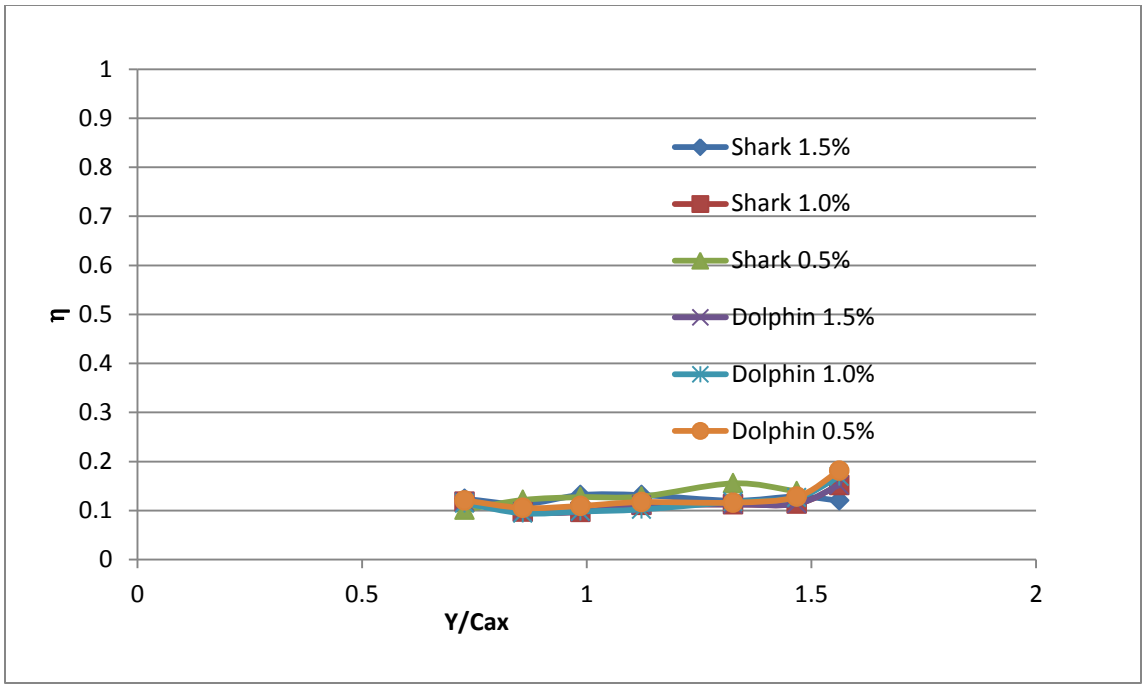

Fig. 7.3.5 Comparison of Adiabatic Effectiveness Values for different MFRs on the Shark or Dolphin Nose Profiles using the Engine-representative Combustor Coolant Temperature Profile in the Approach Flow, X/C_{ax}=0.45

Near the exit of the passage, there is no effect of leakage flow or of one endwall contouring shape over the other on adiabatic effectiveness values. Also, the adiabatic effectiveness values donot vary from the pressure side to the suction side, indicating that the secondary flow structures near this location of the passage do not exist on the endwall, rather they have migrated upwards in the spanwise direction.

7.4 Augmentation (increase over the base case) in adiabatic effectiveness due to introducing the engine-representative combustor exit temperature profile

In the present study, an engine representative combustor exit temperature profile was used to study the endwall film cooling effectiveness of the coolant both in the combustor exit flow as well as in the leakage flow. Studies have been conducted in the past by Erickson [24] using a flat combustor exit temperature profile, meaning there was no

coolant in the combustor exit flow, named Erickson-1. Erickson[24] also conducted studies with a thin combustor exit temperature profile that had coolant in the combustor exit flow only up to 10 % of the span, named Erickson-2. The three profiles are shown in the figure 7.4.1. The 'Solar CFD' profile indicated in the figure was the engine representative temperature profile supplied by Solar Turbines Inc.

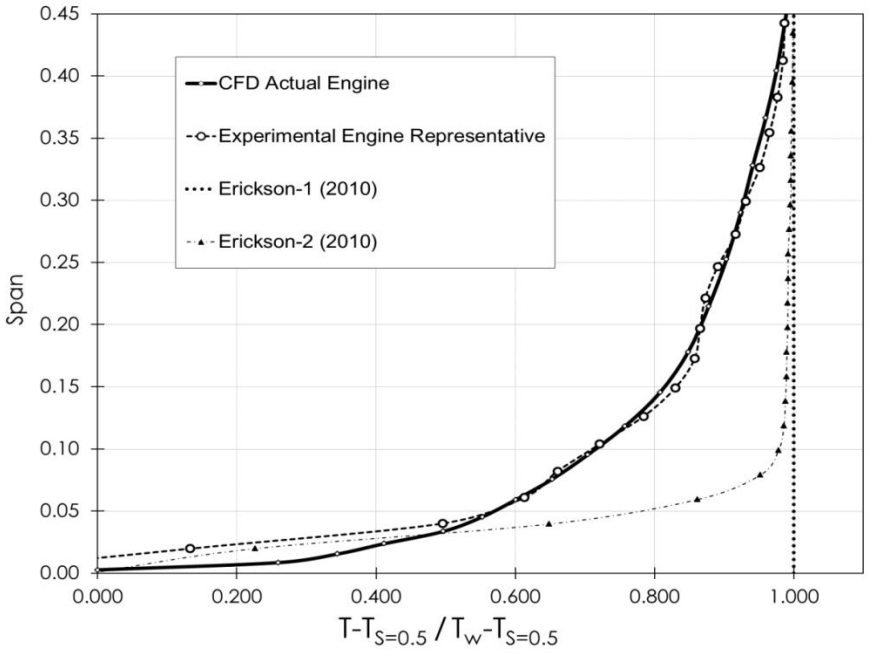

Figure 7.4.1. Approach flow temperature profiles used in the comparison study, the desired profile is marked "CFD Actual Engine"

By using the principle of linear superposition, the advantage of using an engine representative combustor exit temperature profile over a flat profile can be calculated as an augmentation in adiabatic effectiveness given as:

$$\eta_{augmentation} = \eta_{engine-representative} - \eta_{erickson-1} \qquad (7.2)$$

These values of augmentation in adiabatic effectiveness on the Shark nose endwall by using an engine representative combustor exit temperature profile over a flat profile are shown as contour plots in figure 7.4.2

It can be seen in figure 7.4.2, that there is a region of higher augmentation near the suction side at the beginning of the passage for the 0.5 % MFR case and this gradually decreases for cases with higher leakage flow rates. This trend indicates that the higher leakage flow rates have greater influence near the suction side at the beginning of the passage, hence the contribution to endwall protection by the additional coolant in the approach flow is comparatively less as the leakage flow rate increases. Near the pressure side, all the cooling is mostly provided by the coolant in the approach flow, indicated by the similarity of the augmentation values in these regions with those of the adiabatic effectiveness values shown earlier in the chapter (figures 7.2.1, 7.2.2 and 7.2.3). Also , the augmentation values are quite similar to the adiabatic effectiveness values with an engine representative temperature profile, near the exit of the passage, indicating that near the exit of the passage it is the coolant in the approach flow that contributes to all the cooling that can be achieved.

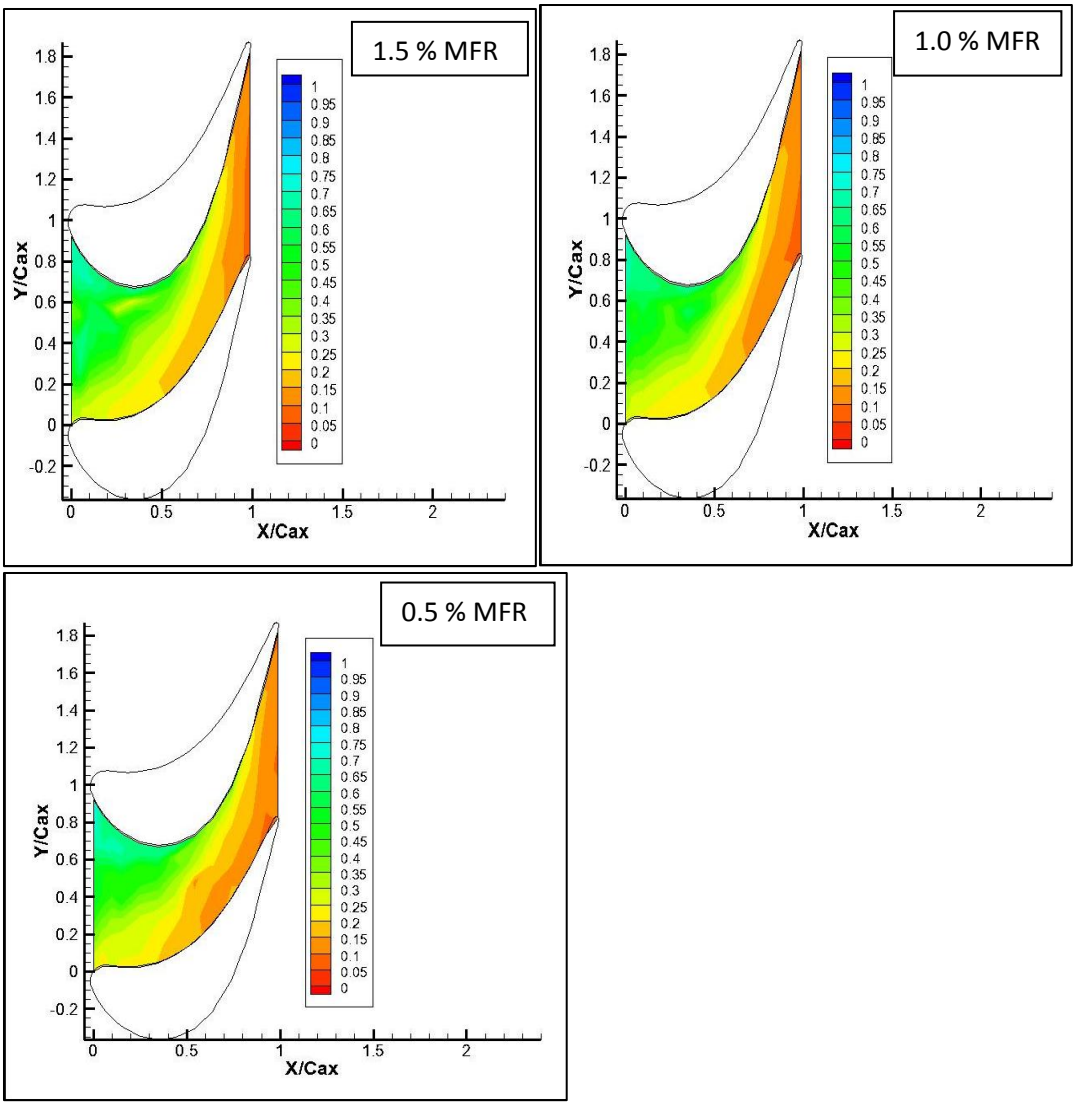

Figure 7.4.2 Augmentation of Adiabatic Effectiveness by using an Engine Representative Combustor-exit Temperature Profile, over a Flat Combustor exit Temperature Profile

Augmentation in adiabatic effectiveness by using an engine representative combustor exit temperature profile over the temperature profile that contained coolant only up to 10 % of the span (Erickson-2) is given as:

$$\eta_{augmentation} = \eta_{engine-representative} - \eta_{erickson-2} \qquad (7.3)$$

These values give an indication of the intensity of mixing within the passage. If there is vigorous mixing within the passage, coolant from the upper reaches of the span will be brought down to cool the endwall in the engine representative approach flow temperature profile. However, for the erickson-2 case, there is no coolant in the upper reaches of the span.This will lead to a high augmentation value at locations where there is vigorous mixing.

Figure 7.4.3 shows the augmentation values over Erickson-2 profile on the shark nose endwall.

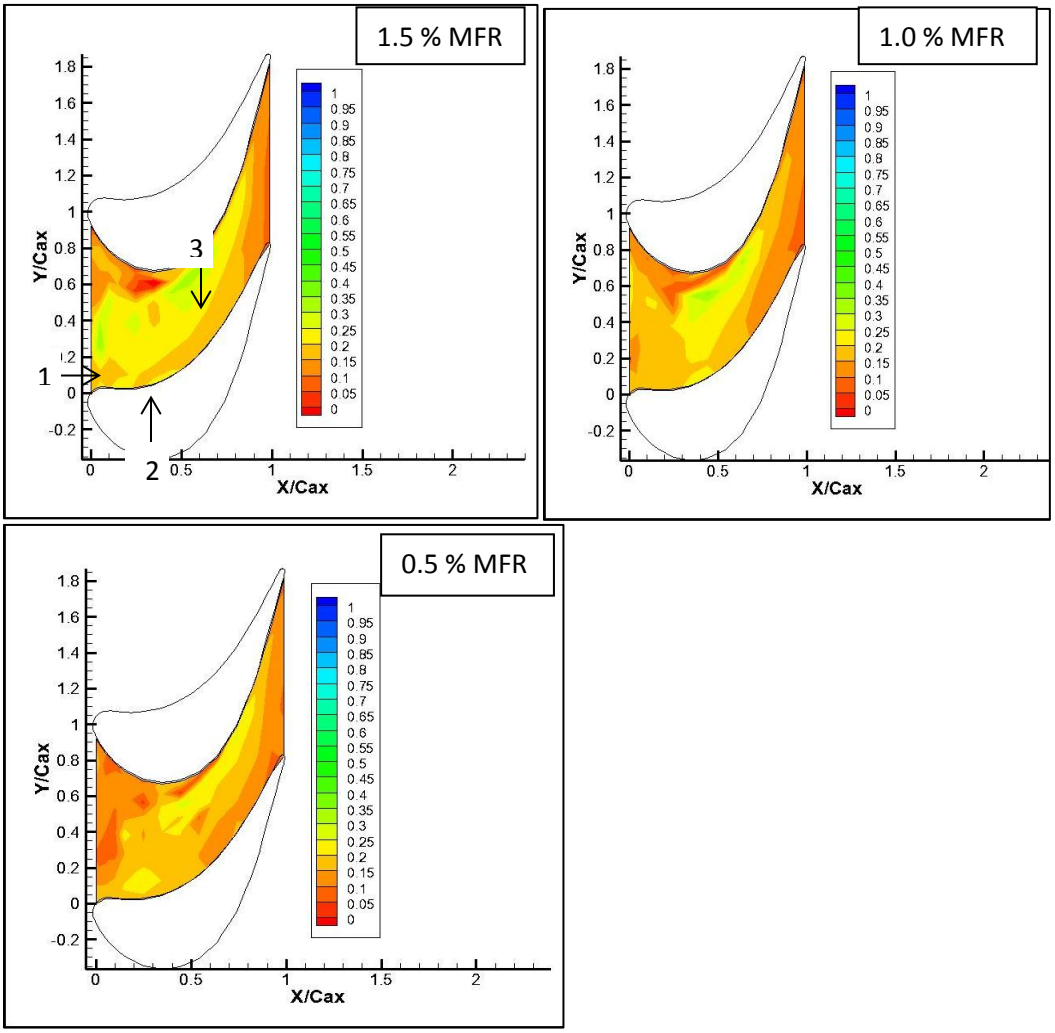

Figure 7.4.3 Augmentation of Adiabatic Effectiveness by using an Engine Representative Combustor-exit Temperature Profile, over Erickson-2 Profile

From figure 7.4.3, three distinct regions of high augmentation values can be identified in case of 1.5 leakage MFR :

- A small region of higher augmentation values at the beginning of the passage in between the suction and the pressure sides. This region seems to be missing for the lower leakage flow rates. It indicates that the higher leakage flow rate leads to intense mixing at the biginning of the passage, leading to more coolant being brought down from the upper reaches of the span.

- A big region of moderately high augmentation values. This seems to be following the path of the passage vortex. It can be seen that this region gets smaller for the 1.0% MFR case and becomes even smaller for the 0.5 % case. This indicates that the higher leakage flow rates lead to more vigorous mixing along the path of the passage vortex.

- Another small region located near the suction side at about X/C_{ax}=0.5. This too becomes smaller for the 1.0 % MFR case and disappears for the 0.5 % MFR case.

7.5 Unheated Leakage Flow and Heated Approach Flow Cases

The present study was done to simulate a situation with coolant present both in the approach flow and leakage flow. Experimentally, such a condition was achieved by heating up the near wall approach flow as well as the leakage flow to about 8-10 degrees above the mainstream flow temperature. However, due to mixing between the near wall flow with the leakage with both being at the same temperature, it is difficult to know exactly where the leakage flow has gone within the passage. Hence in order to 'track' the leakage flow using thermal signatures, it must be kept at a temperature that is different from the near wall heated approach flow. This is done by having unheated leakage (with its temperature being equal to the mainstream passage flow temperature) and heated

approach flow.It should be noted that this case is run with the objective of tracking the leakage flow only; the situation being unrealistic for all other practical purposes.

Passage temperature fields were measured in the same manner as described in section 7.1. Measurements were made only for planes at X/C_{ax}=0.0 ,0.25 and 0.92. Measurements were not made on the plane at X/C_{ax}=0.45.

With unheated leakage-heated near wall approach flow , the recovery temperature is calculated as:

$$\theta = \frac{T_{x,y,z} - T_{\infty}}{T_W - T_{\infty}} \qquad (7.4)$$

Since the wall temperature is kept the same as the mean temperature of the heated leakage flow in the previous cases, by the principle of linear superposition, the non-dimensional leakage contribution can be calculated as:

$$\theta_{leakage-contribution} = \theta_{heated\_leakage} - \theta_{unheated\_leakage} \qquad (7.5)$$

Plotting this non-dimensional leakage contribution provides an idea of where in the passage the leakage flow might have migrated.

.

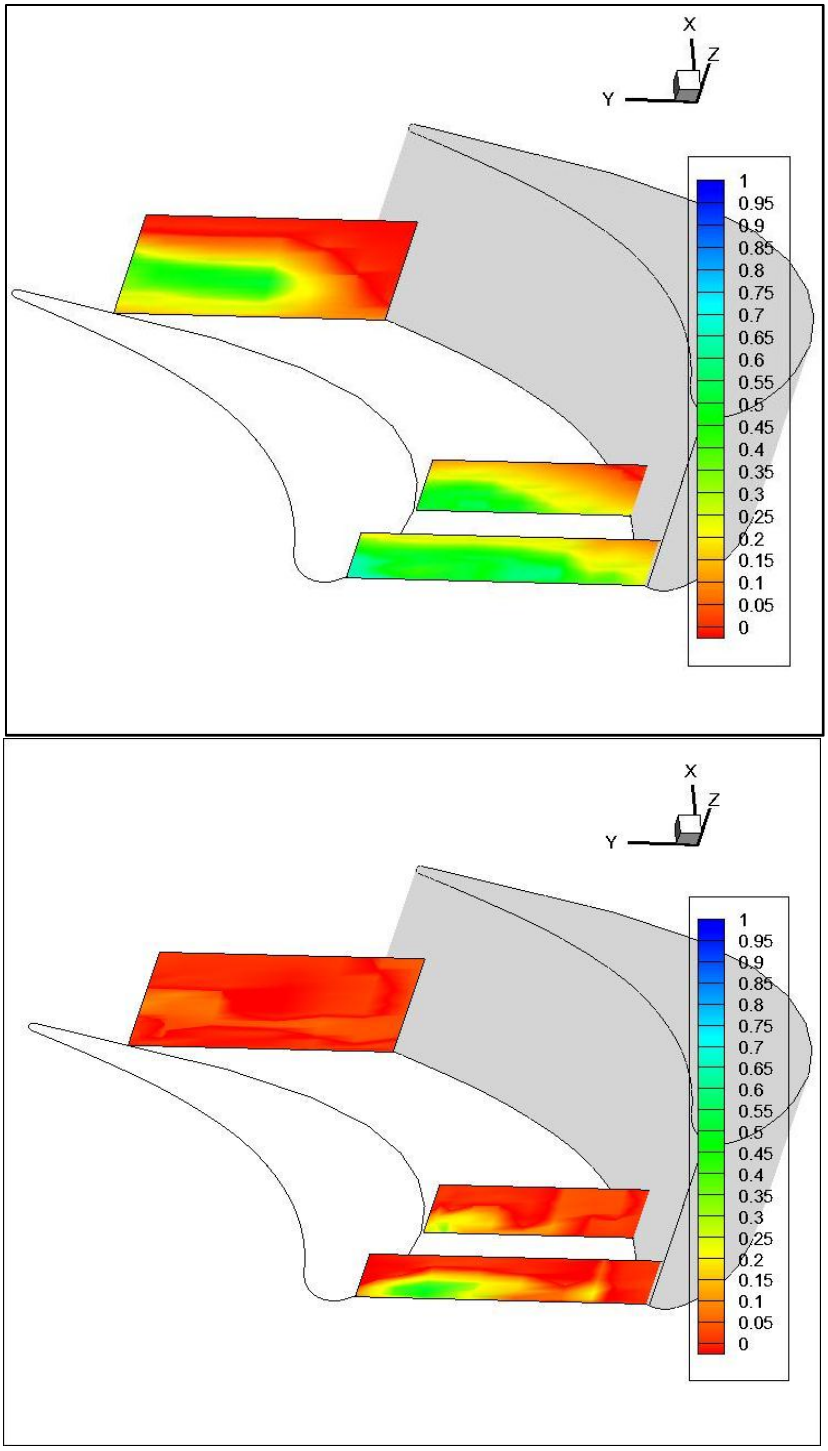

Figure 7.5.1 Passage temperature fields with unheated leakage-heated near wall approach flow (top) and non-dimensional leakage contribution (bottom) at 1.5 % leakage MFR

Figure 7.5.1 shows the passage temperature distribution for the unheated leakage-heated near wall approach flow situation for a leakage flow rate of 1.5% MFR. The plot on the bottom is that of the leakage contribution. It can be seen from both the plots that most of the leakage flow is confined to a region around the suction side. It seems that some part of the leakage flow , on the stagnation plane, is trapped near towards the pressure side, indicated by a tiny region of slightly higher values of leakage contribution. As expected, moving downstream from the passage inlet, the region of influence for the leakage flow shrinks, and is completely diminished by the passage exit.

Figure 7.5.2 shows similar plots with a leakage MFR of 1.0%. The region of influence of the leakage flow has shrunk compared to that of the 1.5 % leakage MFR case.The small region of higher contribution near the pressure side, observed in Figure 7.5.1, has also faded. This indicates that with higher leakage flow rates, the leakage flow has more energy to counter the effect of secondary flows which tend to mix it with the mainstram passage flow.

There is a region of slightly high leakage contibution at 1.0% leakage MFR at X/C_{ax}=0.92. The same tiny region of higher recovery temperature was also seen in figure 7.1.2 for the 1.0 % heated leakage MFR case.

Figure 7.5.3 shows similar plots for the 0.5 % leakage MFR case. Again, the region of influence of leakage flow has further shrunk in comparison to 1.0% MFR case. There is no region of high contribution near the pressure side at the inlet plane. Also, there seems to be no effect of leakage flow at the exit.

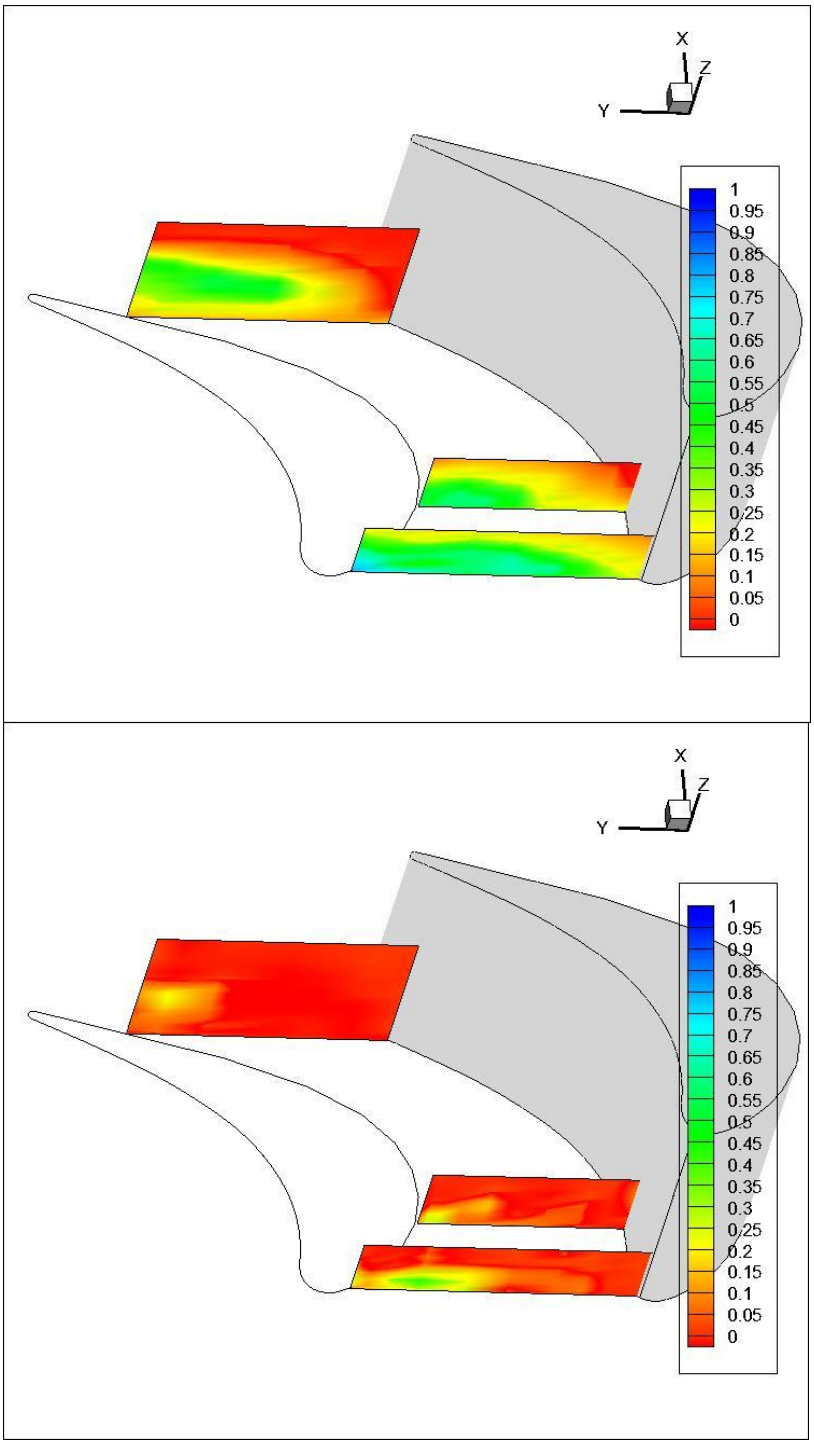

Figure 7.5.2 Passage temperature fields with unheated leakage-heated near wall approach flow (top) and non-dimensional leakage contribution (bottom) at 1.0 % leakage MFR

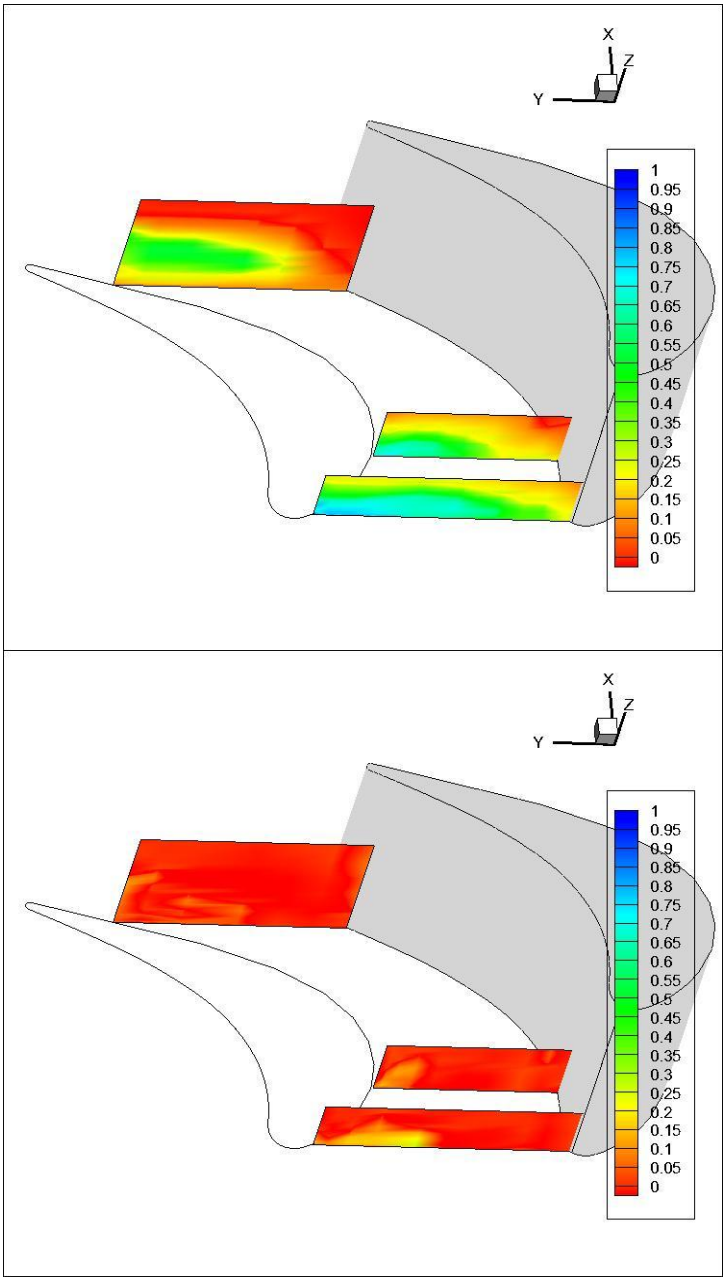

Figure 7.5.3 Passage temperature fields with unheated leakage-heated near wall approach flow (top) and non-dimensional leakage contribution (bottom) at 0.5 % leakage MFR

While thermal field plots give an idea about the migration of leakage flow within the passage, adiabatic effectiveness plots with this unheated leakage flow heated approach

flow situation are made inorder to track the amount of leakage flow actually staying on the endwall. With the leakage flow unheated, the adiabatic effectiveness is calculated as:

$$\eta_{unheated\_leakage\text{–}heated\_approach} = \frac{T_{x,y,z=0} - T_{\infty}}{T_W - T_{\infty}} \qquad (7.6)$$

The leakage contribution is calculated as:

$$\eta_{leakage\_contribution} = \eta_{heated\_leakage\text{–}heated\_approach} - \eta_{unheated\_leakage\text{–}heated\_approach} \qquad (7.7)$$

Where $$\eta_{heated\_leakage\_heated\_approach} = \frac{T_{x,y,z=0} - T_{\infty}}{T_l - T_{\infty}} \qquad (7.8)$$

The wall temperature , $T_{W,}$ is kept the same as the heated leakage temperature T_l, making it possible to get the leakage contribution by just subtracting the quantities.

Figure 7.5.4 shows the adiabatic effectiveness values with the unheated leakage heated approach flow situation, with the corresponding plot of leakage contribution for the case with1.5 % leakage MFR. It can be seen from the figure that the region of maximum contribution of leakage flow is near the suction side at the beginning of the passage. This is an expected result as most of the leakage flow would be pushed toward the suction side due to the strong cross stream pressure gradient. A tiny region of moderately higher contribution is seen near the pressure side in the entry region of the passage at about Y/C_{ax}=0.25. This seems to be the effect of the trace of coolant found in this location as indicated by the temperature field plots.

Figure 7.5.5 shows similar plots for the case with 1.0% leakage MFR.

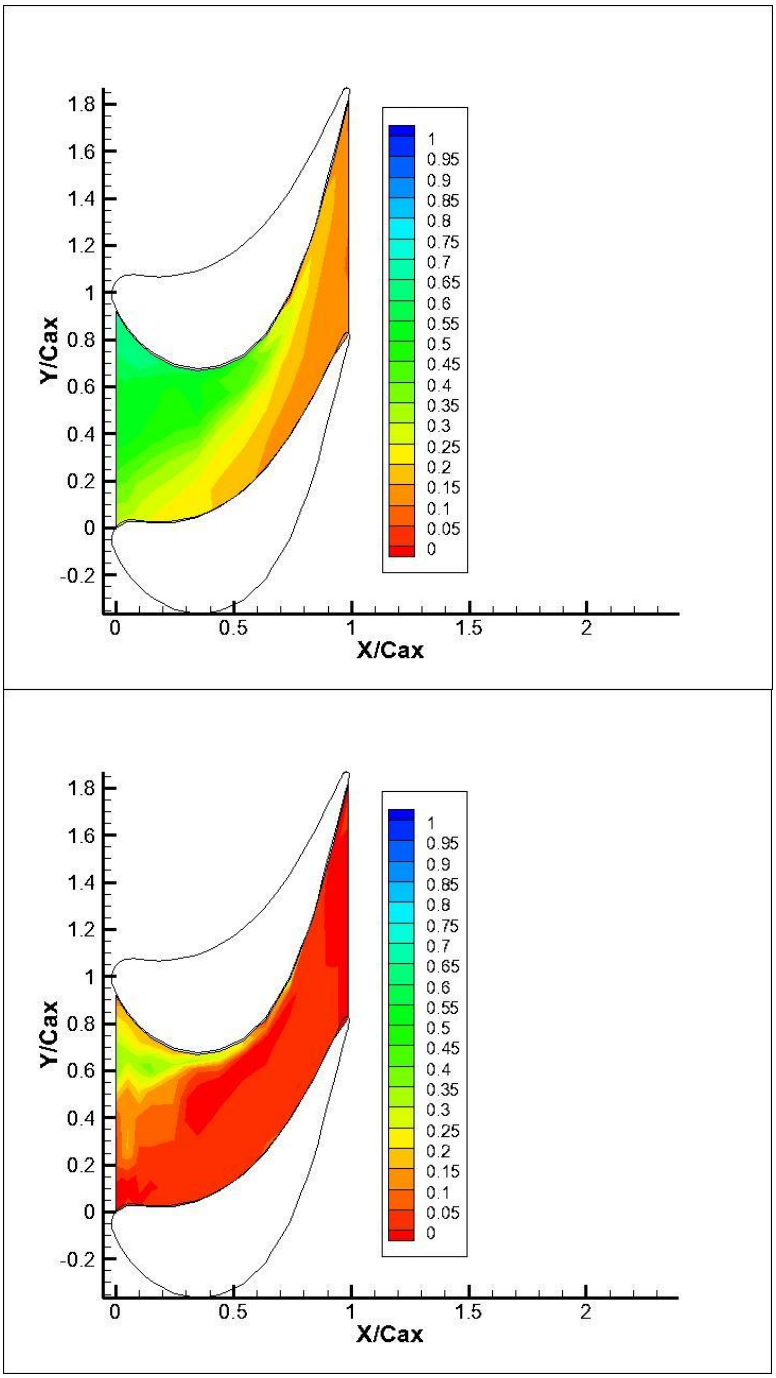

Figure 7.5.4 Adiabatic effectiveness contours for unheated leakage flow and heated approach flow case (top) and corresponding leakage contribution contours (bottom) at 1.5% leakage MFR.

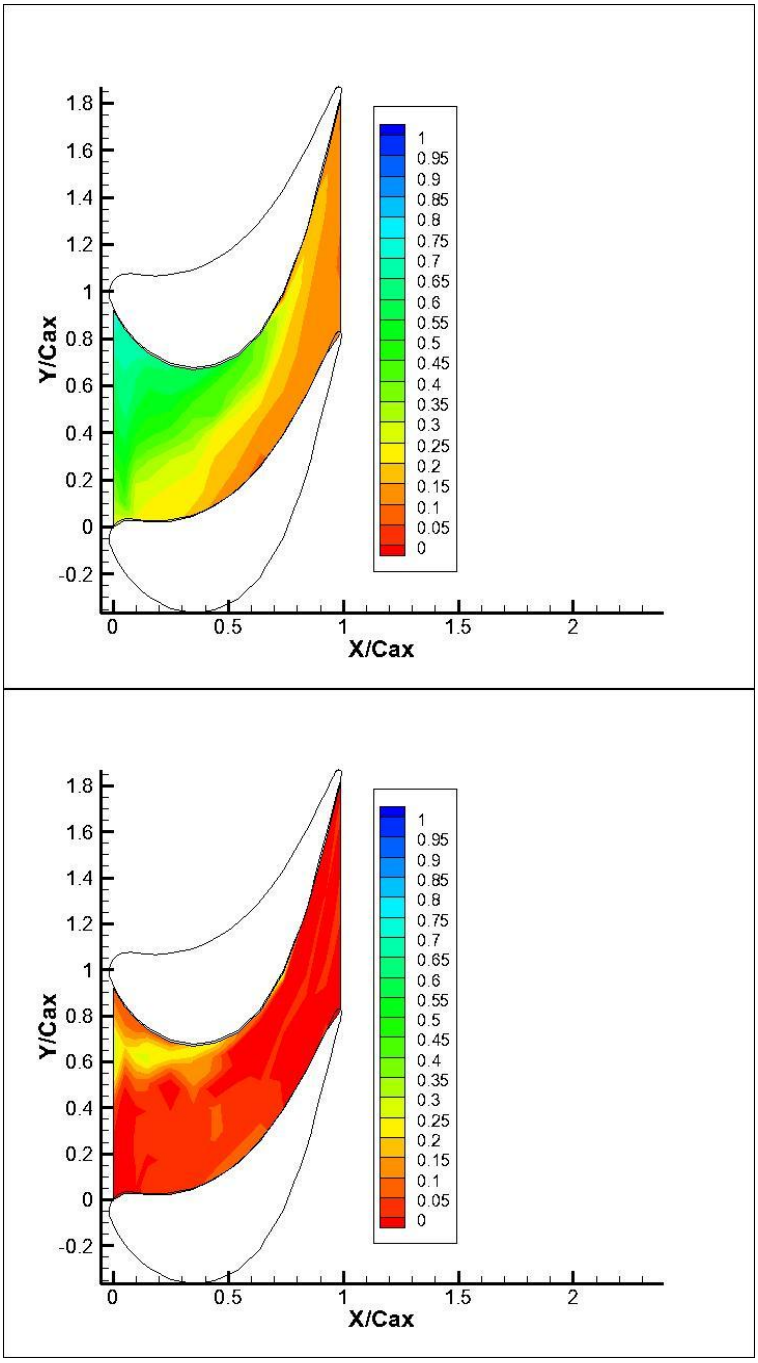

Figure 7.5.5 Adiabatic effectiveness contours for unheated leakage flow and heated approach flow case (top) and corresponding leakage contribution contours (bottom) at 1.0% leakage MFR.

It can be seen from figure 7.5.5 that the region of influence of the leakage flow has shrunk in comparison to the 1.5% leakage MFR case. This, again, is expected because as the leakage flow rate is decreased, it has less energy to counter the secondary flows which tend to mix it with the mainstream passage flow. Figure7.5.6 shows similar plots for the case with 0.5 % leakage MFR.

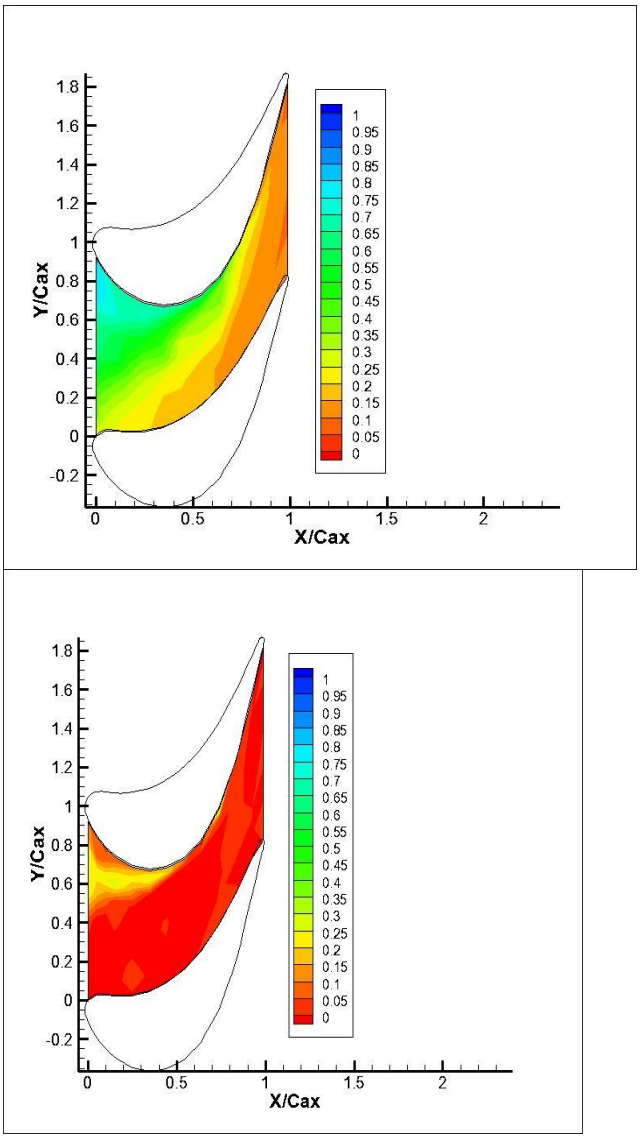

Figure 7.5.6 Adiabatic effectiveness contours for unheated leakage flow and heated approach flow case (top) and corresponding leakage contribution contours (bottom) at 0.5% leakage MFR.

It is interesting to note that the leakage contribution in case of the 0.5% leakage MFR case looks quite similar to the 1.0% MFR case. It is believed that this could be due to the ingression of the passage flow into the leakage plenum for the 0.5% MFR case. As the near wall passage flow is heated, whatever flow comes out of the leakage slot is a mix of this ingressed passage flow and original leakage flow, thus increasing the overall heated flow coming out of the slot and leading to an increase in the leakage contribution.

Chapter 8

Conclusions

An experimental study on the effect of an engine representative combustor exit temperature profile on the adiabatic effectiveness distribution on a contoured hub endwall at different disc cavity leakage flow rates was done. Tests were conducted in a linear rotor cascade with engine representative fluid mechanics. The endwall contour resembled a 'shark nose' and its' design was provided by turbine manufacturer Solar Turbines Inc. The leakage flow is bled through a leakage slot with an engine representative geometry. Leakage mass flow rates of 0.5 %, 1.0% and 1.5% of the passage flow were tested. The approach flow to the cascade passages had a Reynolds number of ~ 430,000 based on mean flow velocity at the inlet and the true chord length of the blades. The mean free stream turbulence intensity was ~ 13 %. An engine representative combustor exit temperature profile was generated by heating the near wall flow through a temperature control slot supplying pre-heated flow and resistance heaters that were placed at specific distances away from the wall.

Measurements made include passage thermal fields and endwall adiabatic effectiveness values. These measurements were compared to an earlier study on a hub endwall with a different contouring scheme called the 'dolphin nose'. The comparison gives insight into the effect of contouring on adiabatic effectiveness distribution at different leakage flow rates, in the presence of an engine representative temperature profile. Also, augmentation in adiabatic effectiveness values by using an engine representative approach flow temperature profile relative to a flat (no thermal boundary layer) temperature profile and relative to another profile with a thin thermal boundary layer are reported. The data for generating the augmentation values were obtained from a study on the same endwall as used by Erickson [24], in which approach flow profiles with no thermal boundary layer and a thin thermal boundary layer had been tested. In order to 'track' the leakage flow mixing with the approach flow, a separate case with unheated leakage flow and heated

near wall approach flow (case with leakage flow temperature being equal to the mainstream passage flow temperature, in presence of an engine representative approach flow temperature profile) was tested.

The passage thermal field measurements indicate that the near wall coolant (present in both the approach flow and the leakage flow) is pushed towards the suction side due to the pressure-to-suction pressure gradient. Higher leakage flow rates lead to a more uniform pitchwise coolant distribution at the beginning of the passage (at a streamwise location of $X/C_{ax}=0$), suggesting that increasing the leakage flow rate helps to more effectively counter the cross stream pressure gradient. As one moves deep into the passage, one sees that the amount of coolant staying near the endwall decreasing indicating mixing of the coolant with the mainstream flow. Near the end of the passage ($X/C_{ax}=0.92$) most of the coolant is seen to be present away from the endwall, in the middle of the passage. This indicates that the coolant has been mixed out in the passage vortex, which has been reported in the literature to be present at the same location at the exit of the passage.

Endwall adiabatic effectiveness distributions indicate that with increasing leakage flow rates, the cooling on the pressure side near the beginning of the passage is increased. Also, in presence of an approach flow temperature profile, there is some cooling (although less) towards the end of the passage. This is a significant result and indicates that the coolant in the approach flow can provide endwall cooling near the passage exit. Comparison of the adiabatic effectiveness values on the 'shark nose' endwall profile to those on the 'dolphin nose' profile (investigated by researcher Yuhyen Seah at the University of Minnesota, Heat Transfer Laboratory; data obtained from Seah by personal communication) indicate that due to its mild gradient the 'shark nose' profile accelerates the near wall flow at the beginning of the passage less rapidly than the 'dolphin nose' profile, leading to more mixing of the near wall fluid with the mainstream flow and lower adiabatic effectiveness values. However the gradient in 'shark nose' profile continues upto a location of $X/C_{ax}=0.31$ and while the gradient in 'dolphin nose' profile ends at $X/C_{ax}=0.06$. As a result, the adiabatic effectiveness values for the shark nose case match

up with the dolphin nose case deep within the passage. The results also show that the variation in adiabatic effectiveness values with changing leakage flow rates is less in the case of the shark nose case than in the case of the dolphin nose case, indicating that the endwall adiabatic effectiveness for shark nose contouring scheme is less sensitive to changing leakage flow rates.

Augmentation plots indicate the additional cooling provided by having an engine representative temperature profile in comparison to a flat temperature profile (no coolant in the approach flow) and a profile with a thin thermal boundary layer (coolant up to 10% of the span). It is noticed that it is the coolant in the approach flow that contributes to most of the cooling as one moves deep into the passage. The augmentation values over the thin thermal boundary layer case identify localized areas of intense mixing, suggesting that coolant has been brought down from the upper reaches of the span to the endwall.

The measurements with an unheated leakage and a heated approach flow help to track the leakage flow within the passage. It is seen that most of the 'influence' of the leakage flow is restricted near the suction side at the beginning of the passage. As one moves deep into the passage the leakage flow mixes out with the passage flow. Increasing leakage flow rates helps toward having a uniform pitchwise coolant distribution.

The present study provides turbine manufacturers data regarding the influence of an engine representative combustor exit temperature profile on endwall adiabatic effectiveness distribution at different disc cavity leakage flow rates. Also, an attempt has been made to compare the results of one contouring scheme to a different scheme in order to provide guidance to turbine designers. The results regarding mixing of the leakage flow with the passage flow indicate that more detailed flow measurements are necessary to understand the influence of leakage flow rates on the secondary flow structures within a passage.

BIBLIOGRAPHY

1. Sieverding, C.H., 1985, “Recent Progress in the Understanding of Basic Aspects of Secondary Flows in Turbine Blade Passages,” ASME J. of Turbomachinery, 114, pp. 248-257
2. Langston, L.S., 2000, “ Secondary Flows in Axial Turbines: A Review”, ICHMT 2000, International Symposium on Heat Transfer in Gas Turbine Systems, Annals of the New York Academy of Sciences, 934, pp 11-26
3. Simon, T.W. and Piggush, J.D., 2006, “Turbine Endwall Aerodynamics and Heat Transfer”, J. of Propulsion and Power, 22, pp 301-312
4. Langston, L.S., Nice, M.L., and Hooper, R.M., “Three Dimensional Flow within a Turbine Cascade Passage”, J. of Engineering for Power, Volume 99(2), pp. 21-28
5. Langston, L. S., 1980, "Crossflows in a Turbine Cascade Passage," J. of Engineering for Power, Volume. 102(4), pp. 866-874
6. Sieverding, C. H., and Van den Bosch, P., 1983, “The Use of Coloured Smoke to Visualize Secondary Flows in a Turbine-Blade Cascade,” ASME J. of Fluid Mechanics,
   134, pp. 85-89.
7. Sharma, J.P., and Butler, T.L., 1987, “ Predictions of Endwall Losses and Secondary Flows in Axial Flow Turbine Cascades”, ASME J. of Turbomachinery, 109, pp.229-236
8. Wang, H.P., Olson, S.J., Goldstein, R.J., and Eckert, E.R.G., 1997, “Flow Visualization in a Linear Turbine Cascade of High Performance Turbine Blades,” ASME J. of Turbomachinery, 119, pp. 1-8
9. Graziani, R.A., Blair, M.F., Taylor, J.R., and Mayle, R.E., 1980, “ An Experimental Study of Endwall and Airfoil Surface Heat Transfer in a Large Scale Turbine Blade Cascade”, J. of Engineering for Gas Turbines and Power, 102, pp. 257-267

10. Goldstein, R. J., and Spores, R.A., 1988, “Turbulent Transport on the Endwall in the Region between Adjacent Turbine Blades,” ASME J. of Heat Transfer, 110, pp. 862-869
11. Blair, M.F., 1974, “ An Experimental Study of Heat Transfer and Film Cooling on Large Scale Turbine Endwalls”, J. of Heat Transfer, 96, pp. 524-529
12. Piggush, J.D. , and Simon, T.W., 2007, “Heat Transfer Measurements in a First Stage Nozzle Cascade Having Endwall Contouring: Misalignment and Leakage Studies”, J. of Turbomachinery, 129, pp. 782-790
13. Thrift, A.A., and Thole, K.A., 2012, “Influence of Flow Injection Angle on a Leading Edge Horse Shoe Vortex”, International J. of Heat and Mass Transfer, 55, pp. 4651-4664
14. Popovic, I., and Hodson, H.P., 2010, “ Aerothermal Impact of the Interaction between Hub Leakage and Mainstream Flows in Highly Loaded HP Turbine Blades”, Proceedings of ASME Turbo Expo 2010, GT2010-22311
15. Suryanarayanan, A.,Mhetras,S.P.,Schobeiri,M.T.,Han, J.C., “ Film-Cooling Effectiveness on a Rotating Blade Platform”, Proceedings of ASME Turbo Expo, 2006, GT2006-90034
16. Lynch, S.P., Sundaram, N., Thole, K.A., Kohli, A and Lehane, C., 2011, “Heat Transfer for a Turbine Blade with Non-axisymmetric Endwall Contouring”, ASME J. Of Turbomachinery, 133(1)
17. Mirzamoghadam, A.V., Heitland, G., Morris, M.C., Smoke, J., Malak, M. and Howe, J., 2008, “3D CFD Ingestion Evaluation of a High Pressure Turbine Rim Seal Disk Cavity, GT2008-50531
18. Pau, M., Paniagua, G., Delhaye, D., De la Loma, A ., Ginibre, P., 2008, “Aerothermal Impact of Stator-Rim Purge Flow and Rotor-Platform Film Cooling on a Transonic Turbine Stage”, Proceedings of ASME Turbo Expo, 2008,GT2008-51295
19. Scheupbach, P., Abhari, R.S., Rose, M.G., and Gier, J., 2009, “Influence of Rim Seal Purge Flow on the Performance of an Endwall Profiled Axial Turbine”, Proceedings of the ASME Turbo Expo 2009, GT2009-59653

20. Hermanson, K. and Thole, K. A., 2000, "Effect of Inlet Conditions on Endwall Secondary Flows," Journal of Propulsion and Power, Vol. 16, No. 2, pp. 286-297
21. Barringer, M. D., Thole, K. A., and Polanka, M. D., 2009, "An Experimental Study of Combustor Exit Profile Shapes on Endwall Heat Transfer in High Pressure Turbine Vanes," ASME J. of Turbomachinery, 131
22. Mathison, R.M., Haldeman, C.W., and Dunn, M.G., 2010, "Aerodynamics and Heat Transfer for a Cooled One and One-Half Stage High Pressure Turbine-Part I:Vane Inlet Temperature Profile Generation and Migration", Proceedings of the ASME Turbo Expo 2010, GT2010-22716
23. Taremi, F.,Sjolander, S.A.,Praisner,T., "Application of Endwall Contouring to Transonic Turbine Cascades:Experimental Measurements at Design Conditions", ASME J. of Turbomachinery, 131
24. Erickson, R.D., 2010, " Experimental Investigation of Disc Cavity Leakage Flow and Hub Endwall Contouring in a Linear Rotor Cascade" , Master's Thesis, University of Minnesota, Twin Cities, USA
25. Goldstein, R.J., 1996, "Fluid Mechanics Measurements", *Taylor and Francis*
26. King, L.V., 1914, "On the Convection of Heat from Small Cylinders in a Stream of Fluid Determination of Convection Constants of small Platinum Wires with Application to Hot Wire Anemometry," Philos. Trans. R. Soc., London, Ser. A, 214, pp.373-432
27. Wilson, D. J., 1970, "An Experimental Investigation of the Mean Velocity, Temperature and Turbulence Fields in Plane and Curved Two-Dimensional Wall Jets: Coanda Effect", Ph.D. Thesis, University of Minnesota, Minneapolis, MN.
28. Adolfson, D.A., 2003, "Oscillatory and Unidirectional Fluid Mechanics Investigations in a Simulation of a Stirling Engine Expansion Space," M.S. Thesis, University of Minnesota, Minneapolis, MN.
29. Tennekes, H., Lumley, J. L., 1972, A First Course in Turbulence, MIT Press
30. Smol'yakov, A.V. and Tkachenko, V.M., 1983, " The Measurement of Turbulent Fluctuations", Springer (Translated by S. Chomet, King's College, London)
31. Stull, R. B., 2008, An Introduction to Boundary Layer Meteorology, Springer

32. Hinze, J. O., 1975, Turbulence, 2nd ed., McGraw-Hill
33. Ames, F. E., Moffat, R. J., 1990, "Heat Transfer with High Intensity, Large Scale Turbulence: The Flat Plate Turbulent Boundary Layer and the Cylindrical Stagnation Point," Report No. HMT-44, Stanford University, Stanford, CA
34. " Laminar Flow Elements: Installation and Operation Manual", Meriam Process Technologies
35. Burns, G. W., Scroger, M. G., Strouse, G. F., Croarkin, M. C., Guthrie, W. F., 1993,
36. "Temperature-Electromotive Force Reference Functions and Tables for the Letter-Designated Thermocouple Types Based on the ITS-90," Natl. Inst. Stand. Technol., Monograph 175
37. Dwyer Instruments, Inc., Bulletins D-57 and D-3, http://dwyer-inst.com
38. Validyne Engineering Corp., http://validyne.com
39. Goldstein, R.J. , 1974. "Film Cooling", Advanced Heat Transfer